Influence of Sulfur on Liquid Fuel Reforming

by

Joseph M. Mayne

A dissertation submitted in partial fulfillment
of the requirements for the degree of
Doctor of Philosophy
(Chemical Engineering)
in The University of Michigan
2010

Doctoral Committee:

Professor Johannes W. Schwank, Chair
Professor Philip E. Savage
Professor Margaret S. Wooldridge
Associate Professor Suljo Linic
Adjunct Professor Galen B. Fisher

For Baby Joey

ACKNOWLEDGEMENTS

This dissertation presents the fruits of the amazing collaborative relationships that have defined my graduate studies at Michigan. I have been especially fortunate to enjoy the benefit of guidance from three individuals that have defined for me the meaning of the word mentor. Chief among these is my advisor, Johannes Schwank, who tempered my most cynical tendencies and offered the encouraging words which helped foster my growing confidence. Benjamin Gould provided the most assistance in developing my first experimental catalysis skills. I thank him for his patience and council through some of the most challenging times of my graduate career. I must also thank Andrew Tadd who proved a seemingly endless source of new ideas, helpful encouragement, and thought provoking discussion. His guidance was most essential into developing the researcher that I am today.

I thank my thesis committee of Galen Fisher, Suljo Linic, Philip Savage, and Margaret Wooldridge for their generous contributions of time and support. I must acknowledge the great amount that I have learned from Professors Linic and Savage as a student in their courses. Professor Linic's unique perspective prompted me to approach thinking of my research in a completely new manner, while Professor Savage's tutelage helped spur continued vigilance in developing reaction engineering and error analysis skills. I especially acknowledge the contributions of Galen Fisher and his extensive experience and astounding approachability. His helpful discussions and pointed questions were integral to the work described in these pages.

Much of the work of my dissertation derives either directly or indirectly from

collaboration with fellow students. Kevin Dahlberg performed many of the X-Ray Diffraction measurements and Transmission Electron Microscopy which will be discussed and was an invaluable editor when preparing manuscripts. He is a hard worker with innovative ideas, and it has been one of the greatest pleasures of my graduate career to pay-forward the mentorship so graciously imparted upon me. In addition to performing the IR measurements discussed in Chapter IV, Thomas Westrich and I were able to form a great working relationship owing to our complimentary skill sets. For example, he was particularly helpful when I needed to develop new control software for my flow reactor system. His engineering skills are unmatched by any student I have worked with. I also acknowledge the work of Jonathon Butler who worked for a time as an undergraduate researcher in our group. He helped perform some of the initial experiments which would eventually culminate with the work described in Chapter V.

I would also like to acknowledge the tireless efforts of the Chemical Engineering department staff. Susan Hamlin, Claire O'Connor, Shelley Fellers, and Mike Africa were especially helpful to me personally. Harold Eberhart, a master glassblower, prepared several pieces of glassware for me, including my reactor tubes. Additionally, his open door and tool collection were a graduate student's dream. Dr. Kai Sun and Dr. Haiping Sun, of the Electron Microbeam Analysis Laboratory (EMAL), are acknowledged for all of their help and training on EMAL equipment.

Financial support for this work was provided by the U.S. Army Tank-Automotive Research, Development and Engineering Center under Cooperative Agreement Number W56HZV-05-2-0001, and by the U.S. Department of Energy under Contract Number DE-FC26-06NT42813. Their support is gratefully acknowledged.

I would also like to thank those in my personal life who inspired my success or simply made my life more enjoyable with their friendship. It would be difficult to name all of those people who have made my life at Michigan the most enjoyable

time of my life despite all of the stresses that graduate school offers. However, I will acknowledge the close friendships I have developed with Meghan Cuddihy, Thomas Westrich, Neil Schweitzer, Amanda Hickman, James and Amy Bucher, Bean Getsoian, Elizabeth Ranney, David and Nikki Ingram, Daniel and Michelle Lilly, Philip Christopher, Peter Burgardt, Michael Senra, Adam Holewinski, Michael Hoepfner, Elizabeth Stewart, Allison Bourke, Sean Langlier, Ashish Agarwal, Christine Andres, Daniel and Erin McNerny, Jason Huang, Kevin and Georgina Critchley, Siris Laursen, Ramsey Zeitoon, and Stephanie Teich-McGoldrick. I thank them all for their various positive contributions to my life.

The bulk of the credit for my personal success is thanks to my parents, Lorraine and Douglas Mayne. My mom is the hardest working person I know and I am inspired by her success and I am constantly striving to live up to her strong ideals and values. My dad fostered what would become my passion for science and helped me hone math and computer skills from an early age. I also thank my sister, Jessica Mayne, who initiated my interest in both Chemical Engineering and the University of Michigan.

Above all I must acknowledge my wife, Megan. She has been patient and supportive throughout my graduate career. She has challenged me to grow as an individual and that has benefited my work tremendously.

TABLE OF CONTENTS

LIST OF FIGURES

Figure

LIST OF TABLES

Table

LIST OF ABBREVIATIONS

ATR Autothermal Reforming

APU Auxilliary Power Unit

CZO $Ce_{0.75}Zr_{0.25}O_2$

DI deionized

d_p particle diameter

DRIFTS Diffuse Reflectance Infrared Fourier Transformed Spectroscopy

EDS energy-dispersive X-ray spectroscopy

GC Gas Chromatograph

GHSV gas hourly space velocity

H_2O/C steam to atomic carbon ratio

HDS hydrodesulfurization

NO_x oxides of nitrogen

O/C atomic oxygen to atomic carbon ratio

POX Partial Oxidation

PFD process flow diagram

PFPD Pulsed Flame Photometric Detector

S_A active surface area

SCR Selective Catalytic Reduction

SEM Scanning Electron Microscopy

SOFC Solid Oxide Fuel Cell

SR Steam Reforming

STEM Scanning Transmission Electron Microscopy

TCD thermal conductivity detector

TGA Thermogravimetric Analysis

TEM Transmission Electron Micrsocopy

TPO Temperature Programmed Oxidation

TPR Temperature Programmed Reduction

VSC Volatile Sulfur Compound

XPS X-Ray Photoelectron Spectroscopy

XRD X-Ray Diffraction

$\mathbf{Y}_{SG}$ synthesis gas yield

ABSTRACT

Influence of Sulfur on Liquid Fuel Reforming

by

Joseph M. Mayne

Chair: Johannes W. Schwank

The production of H_2 and CO (synthesis gas) by reforming petroleum distillates, such as commercial gasoline, is a growing technology with widespread potential impact on America's energy efficiency. This dissertation describes the application of Ni-based catalysts to the Autothermal Reforming (ATR) of isooctane, a surrogate for gasoline. In this system, isooctane, air and water react to form an equilibrium-limited effluent, comprised chiefly of synthesis gas. Unfortunately, the widespread adoption of Ni-catalyzed ATR is limited by the tendency of the catalysts to lose activity when exposed to even low concentrations of sulfur.

Experiments explored the effects of thiophene on isooctane reforming over Ni under varying reaction stoichiometries. As expected, the presence of thiophene led to lower production of synthesis gas for all conditions. One finding of this work was that the steam reforming performance of the catalyst was more adversely affected by the presence of sulfur than was partial oxidation activity. However, stable performance of the catalyst for at least 48 hours-on-stream was achieved at inlet conditions which favored high production of hydrogen (H_2 molar fractions greater than 30%). Interestingly, these conditions also corresponded to those when thiophene was largely or

completely converted to H_2S.

In an effort to examine the role of under-coordinated sites, an innovative approach was used to investigate the influence of Ni particle size during isooctane ATR. Under sulfur free conditions, catalysts comprised of roughly 5 nm Ni particles produced 32% less synthesis gas than catalysts with a mean Ni diameter of 50 nm. Although the bigger particles were more affected by sulfur exposure, they still had a 25% higher yield of synthesis gas than the smallest particles when thiophene was present.

Finally, several bimetallic catalysts were designed and tested for their durability under high exposure of thiophene. Increased stability appeared possible by alloying Ni with either platinum or tungsten.

This study has revealed new understanding about the performance of this reaction as determined by reaction conditions, sulfur content, Ni particle size, and bimetallic metal formulations. This new wisdom provides the foundation for the production sulfur-tolerant ATR reactors by employing inexpensive Ni-based catalysts.

CHAPTER I

Introduction to Reforming Catalysis

1.1 From Fossil Fuels to Hydrogen Gas

Fossil fuels such as natural gas and petroleum distillates (gasoline, diesel, jet fuel) are ubiquitous energy sources of the current economy. Together, they comprise about 61% of the United States energy consumption (*DOE*, 2005b). Their widespread implementation is due to their highly matured distribution infrastructures and relatively high energy density on a per volume basis. However, the continued reliance on these energy sources as the backbone of future economic growth is increasingly haunted by the twin specters of dwindling supply and their potential for environmental harm.

The ability of the American economy to continue to hinge upon petroleum has particularly come under increasing economic and geopolitical uncertainty. Domestic oil production peaked in 1970, causing the ever-increasing demand to be progressively more committed to imported sources, as shown in Figure 1.1 (*DOE*, 2005a).

Additionally, the heavy dependence on combustion of carbon based fuels has a myriad of environmental consequences. The products of hydrocarbon combustion, CO_2 and H_2O, are greenhouse gases and the steadily increased atmospheric concentration of CO_2 has been linked to increased average global temperatures and widespread climate change (*Hansen et al.*, 1981). Furthermore, combustion byproducts such as unconverted hydrocarbons and oxides of nitrogen (NO_x) are responsible for the

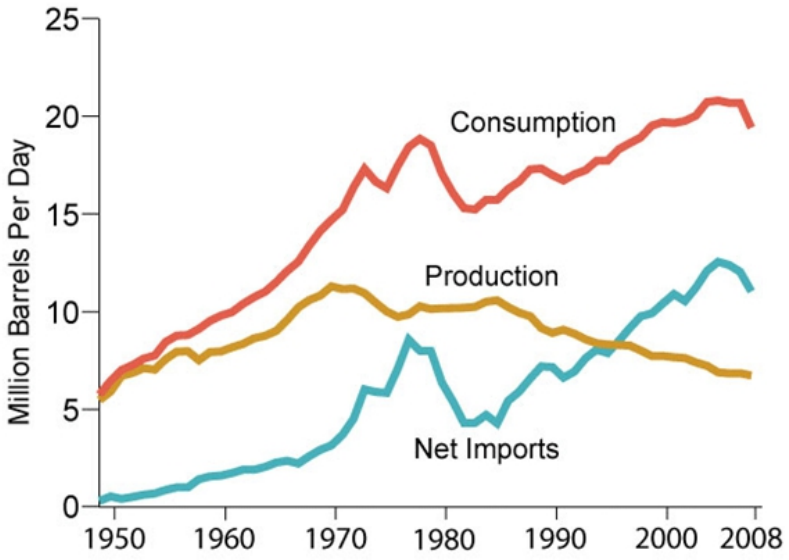

Figure 1.1: United States consumption, production, and total imports of petroleum. Reproduced from *DOE* (2005a).

formation of ground-level ozone leading to smog and respiratory illness (*Bell et al.*, 2004).

Both environmental and economic concerns caused by the continued use of natural gas and petroleum would obviously be remedied by a new technology which radically altered the way energy is produced and utilized. However, despite recent improvements to several technologies (such as nuclear fission and solar voltaic cells), there is still no clear winner in the race to replace fossil fuel combustion as the primary route of energy production.

One recently touted replacement for fossil fuels has been the proposed use of hydrogen gas as the energy carrier of choice. The electrochemical oxidation of hydrogen in a fuel cell is an attractive reaction due to its benign nature from an environmental perspective and its potential for high exergy (useful work potential) efficiency from a thermodynamic perspective (*Haynes*, 2001). The proposed model based upon this chemistry has become known colloquially as the Hydrogen Economy.

However, the practical implementation of a Hydrogen Economy is problematic for

several reasons. First, although hydrogen is the most universally abundant element, it is not naturally available in molecular form. For this reason hydrogen should not be thought of as an energy source, but rather as an energy carrier. Therefore, hydrogen gas must be generated from a primary energy source.

The second drawback to a Hydrogen Economy is that hydrogen gas has a very low density. The implication of this is that once produced, hydrogen must be immediately converted in a fuel cell or stored. Liquefaction and chemical fixation of hydrogen both represent plausible storage strategies, each with their respective costs on system efficiency. These challenges taken together with the current lack of supporting infrastructure represent formidable challenges to the widespread adoption of a Hydrogen Economy.

Although the realization of a purely hydrogen based energy industry is anything but inevitable, there are niche roles that hydrogen may readily fill in the current energy economy. Ironically, the production of hydrogen from fossil fuels represents a promising route for early adoption of hydrogen-based technologies. While these systems would not completely assuage the concerns of either dwindling fossil fuel supply or adverse environmental impact, the efficiency gains over combustion based systems would offer marked improvements on these fronts in certain scenarios. Additionally, on-demand production of hydrogen from the energy-dense fossil fuels of an existing distribution infrastructure does not contend with the drawbacks of a full-scale Hydrogen Economy.

The chemistry used to convert fossil fuels (other than coal) to H_2 rich streams is termed either reforming or fuel processing. Ideally, reforming reactions convert the carbon in fuel to CO, resulting in a reformate stream highly reductive in nature. High temperature Solid Oxide Fuel Cells (SOFCs) are able to electrochemically oxidize the reformate mixture, producing CO_2 and H_2O as byproducts. This combination of hydrogen production from reforming chemistry and fuel cell power generation may be

used to produce electricity for a range of applications from stationary power generation to motive and non-motive transportation demands (*Krumpelt et al.*, 2002).

On-board a transportation or military vehicle reforming technology has several applications. Specifically, there is a significant amount of interest in both private and public spheres to produce Auxilliary Power Units (APUs). These devices would satisfy non-propulsion electrical demands (up to around 10 kW) which are of particular importance to the long-haul trucking industry and the military sector (*Brodrick et al.*, 2002; *Lamp et al.*, 2003; *Jain et al.*, 2006; *Patil et al.*, 2004). In the transportation sector, it has been estimated that approximately 2.5 billion gallons of fuel are burned annually during idling scenarios (*Gaines et al.*, 2006). Under these conditions, the efficiency of internal combustion engines is as low as 3% (*Brodrick et al.*, 2002). Various technoeconomical studies have demonstrated that long-haul truckers who instituted a fuel-cell based APU would enjoy a payback period of around 2 years and a modest 15% market penetration of APUs would decrease the NO_x emitted from the nation's fleet of idling engines by 40% (*Lutsey et al.*, 2007; *Jain et al.*, 2006).

There is also potential for reformate gas to participate in several emission reduction technologies (*Schwank and Tadd*, 2010). Among these potential uses are the cold-start ignition of an internal combustion engine and several post-combustion pollution control technologies, such as the Selective Catalytic Reduction (SCR) of NO_x. An overview of some additional applications of reforming chemistry are shown in Figure 1.2. It is clear from this brief outline that the potential for reforming chemistry is fairly extensive.

1.2 Confronting the Challenges of Liquid Fuel Reforming

Motivated by the breadth of potential applications, various researchers have made significant progress in recent years towards the development of fuel reformers. There are three catalytic routes for the production of synthesis gas (H_2 and CO) from liquid

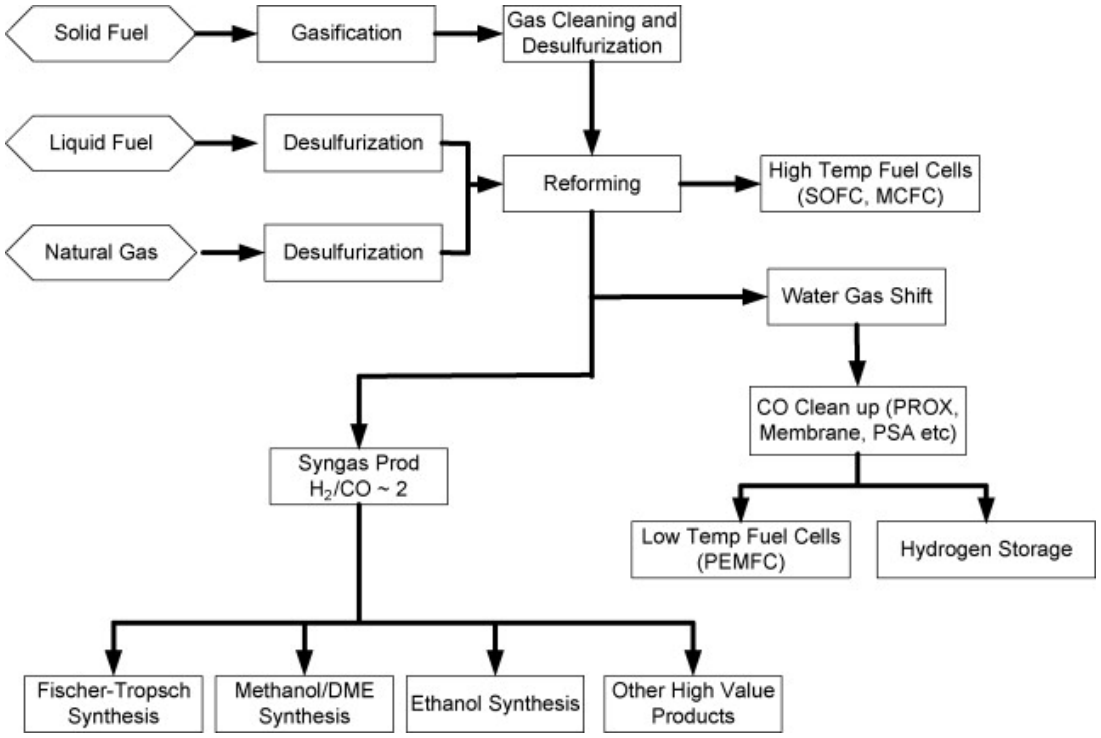

Figure 1.2: Fuel processing of gas, liquid, and solid hydrocarbon fossil fuels to produce H_2 rich product gas, and the potential applications of this technology. Figure from *Holladay et al.* (2009).

hydrocarbon fuels. These are Steam Reforming (SR), Partial Oxidation (POX), and Autothermal Reforming (ATR). Generalized chemical formulas which describe these respective reactions are shown for a generic hydrocarbon, C_xH_y, in Reactions 1.1, 1.2, and 1.3.

$$C_xH_y + xH_2O \rightarrow \left(\frac{y}{2} + x\right) H_2 + xCO \tag{1.1}$$

$$C_xH_y + \frac{x}{2}O_2 \rightarrow \frac{y}{2}H_2 + xCO \tag{1.2}$$

$$C_xH_y + (x - 2z)\, H_2O + zO_2 \rightarrow \left(\frac{y}{2} + x - 2z\right) H_2 + xCO \tag{1.3}$$

SR is the most industrially mature of these technologies, as it is the current commercial production route for hydrogen from natural gas. The reaction is carried out in excess of steam and at elevated temperatures because the reaction is highly endothermic. Due to the excessive heat demands of the reaction, heat is usually supplied by a simultaneous combustion of a portion of the fuel. In practice, reaction rates are limited by the heat transfer from burners to the reformer units. Thus, while SR has the highest stoichiometrically predicted production of H_2 of the three routes, the actual efficiency is limited by the need to burn some fuel to produce heat.

On the other end of the enthalpic spectrum is POX, where the fuel is reacted with a sub-stoichiometric feed of air, leading to the incomplete combustion products of H_2 and CO. In this exothermic reaction the rates are much quicker than SR, and are generally limited by mass transfer effects, meaning that the chemistry occurs only as quickly as reactants can be supplied to the reaction site. The prolonged activity of these sites is especially limited in the case of POX due to competing reactions which foul the sites with carbon deposits. Also, the absence of water in the feed results in a lower stoichiometrically expected hydrogen production.

Seen as a compromise between the other two options, ATR offers less severe con-

ditions compared with POX but still capitalizes on partial oxidation mechanisms to provide heat to the system. Under finely tuned conditions, the reaction may even be operated thermoneutrally, such that the energy supplied by exothermic pathways is balanced by the endothermic demands ($\Delta H_{Rxn} \approx 0$). The inclusion of water in the feed has two benefits compared to POX. First, water has been shown to decrease the deposition of carbon on catalysts; and second, the presence of water increases the stoichiometric limit on H_2 production.

Developing an exact mechanistic picture for all three fuel reforming reactions has been the subject of significant progress in the catalysis community. Due to the similarities of the different systems, it is best to envision the SR reaction as an integral piece of the POX system, which is in turn very similar mechanistically to ATR.

Extensive work has been performed to describe methane SR, due to the industrial significance of this process. *Rostrup-Nielsen* (1984) presented an in-depth review of the pertinent literature. In short this reaction involves the catalytic dehydrogenation of methane, forming surface carbon atoms which react with surface hydroxyl (OH) species to produce H_2 and CO. Based upon this mechanism, the structure of the support plays an important role. Specifically, it is important that the catalyst is able to somehow escape the pit-fall of carbon deactivation. Additionally, the high activation barrier for C-H bond cleavage makes it difficult to achieve high methane conversion. Considering the SR of heavier hydrocarbons, there is an increased importance of α-scission of C-C bonds. In all cases, it has been shown that carbon deposition can be limited by maintaining a high steam to atomic carbon ratio (H_2O/C).

Spatially resolved techniques have been employed by several researchers to describe the internal chemistry of a POX reactor (*Horn et al.*, 2006, 2007; *Fisher*, 2009). These techniques demonstrate that oxygen is quickly consumed near the front edge of the catalyst, producing mainly combustion products (CO_2 and H_2O). These intermediate products are then utilized in the remainder of the catalyst bed to pro-

duce the desired reforming products, presumably through the endothermic steam and dry reforming mechanisms (1.1, 1.4). The final product distribution is then controlled by approach to thermodynamic equilibrium (which may be described by such reactions as the Water Gas Shift Reaction, 1.5). Non-catalytic gas-phase reactions are also important when considering the POX of heavier hydrocarbons (*Panuccio et al.*, 2006). Thermal cracking of these compounds before they reach the catalyst leads to the intermediate formation of light olefins and paraffins.

$$C_xH_y + xCO_2 \rightarrow \frac{y}{2}H_2 + 2xCO \tag{1.4}$$

$$CO + H_2O \rightleftharpoons CO_2 + H_2 \tag{1.5}$$

In summary, this mechanistic picture depicts three distinct regions: upstream homogeneous cracking, catalytic oxidation zone and catalytic reforming zone. This chemical description has been applied also to explain the ATR of heavy hydrocarbons (*Qi et al.*, 2005; *Yoon et al.*, 2008; *Gould et al.*, 2007).

As fuel processing is a catalytic process, it is necessary to introduce the concept of a catalyst. It is simplest to envision heterogeneous reforming catalysts as providing the surface sites which act as the meeting point for reactants of the elementary chemical reactions which combine to describe the total chemistry of the reactor. Therefore, the performance of a catalyst is maximized when the material exhibits the largest number of active and physically accessible sites. This motivates the use of supported catalysts, where the active material (generally a metal) is dispersed over a porous material with a complex micro-structure. Many such catalysts have been developed and tested in reforming catalysis.

The activity of reforming chemistry has been demonstrated on supported transition metal surfaces, including Pt, Rh, Pd, Ru and Ni (*Krumpelt et al.*, 2002; *Schwank*

and Tadd, 2010). The development of non-noble metal based catalysts is highly desirable to increase the economic viability of fuel reforming technology. Specifically, considerable progress has been made recently in developing Ni catalysts supported by a mixed oxide of Ce and Zr (*Tadd et al.*, 2005; *Gould et al.*, 2007; *Chen et al.*, 2007; *Dantas et al.*, 2010; *Escritori et al.*, 2009; *Kambolis et al.*, 2010; *Kumar et al.*, 2007; *Montoya et al.*, 2000; *Youn et al.*, 2008). This support is advantageous for several reasons, not the least of which is that itself is active to many of the reactions of interest in a liquid fuel processor.

However, it is clear that there are several challenges which limit the widespread adoption of liquid fuel reforming. These mainly deal with the ability to maintain the activity of catalyst sites under reforming conditions. There are three main processes in a reformer which tend to decrease catalyst performance. They are catalyst particle growth, known as sintering; carbon deposition; and sulfur poisoning (*Sehested*, 2006).

Sintering can affect both the support and active metal in catalysis. Elevated temperature can cause a degradation of support microstructure, rendering some of the active sites physically inaccessible. Additionally, the conditions of a reforming environment are well suited for the agglomeration of metal particles. When particles coalesce, they do so because there is a thermodynamic driving force to minimize their surface area. Unfortunately, less metallic surface area results in fewer active sites to accommodate the elementary steps of the chemistry.

Carbon deposition occurs when carbon on the catalyst surface binds together forming various types of carbon based structures. These structures can block accessibility to active sites, increase pressure drop across the catalyst, and degrade the mechanical integrity of the supporting structure. Due to the problematic nature of carbon formation on Ni catalyzed reforming, there is a wealth of literature available which seeks to describe and prevent the phenomenon (*Rostrup-Nielsen*, 1984; *Schwank and Tadd*, 2010).

However, perhaps the biggest impediment to fuel reformer technology, even noble metal based approaches, is their susceptibility to active site poisoning by sulfur containing compounds. These molecules are found at various levels in liquid fuel feed-streams. The concentration and identity of these sulfur compounds depend on the type of liquid fuel which is to be processed. They exist in these fuels because they are present in the crude oil from which these fuels are derived (and also present as fuel-additives in the case of jet fuels).

The average sulfur content in crude oil has increased over the years. It has recently been reported at about 1.4 wt% (*DOE*, 2007). Sulfur is removed during the refinery process according to appropriate specifications in order to decrease the amount of sulfur oxides emitted to the atmosphere during combustion of the fuels. Various specifications for transportation fuels are given in Table 1.1. These specifications provide a rough estimate for the expected sulfur concentration in the prospective reforming feed streams.

Crude Oil	1.4 wt%
Diesel Fuel (Dibenzothiophenes)	
Low Sulfur Diesel	500 ppmw
Ultra Low Sulfur Diesel	15 ppmw
Euro IV Standard	50 ppmw
Jet Fuel (Benzothiophenes)	
JP-7	1000 ppmw
JP-8	3000 ppmw
Commercial Gasoline (Thiophenes)	
Annual Average Cap	30 ppmw
Per Gallon Cap	80 ppmw

Table 1.1: Specified concentrations of atomic sulfur in various petroleum distillates and products. Data compiled from *DOE* (2007); *EPA* (2007); *Chevron* (2006); *NPRA* (2010).

It is possible to significantly decrease the concentration of sulfur to below 0.2 ppmw S upstream of the reforming catalyst (*Hernandez-Maldonado and Yang*, 2004). This is achieved by the selective adsorption of thiophenic compounds to a sorbent

material via π-complexation. However, in some applications the implementation of upstream sorbent beds, which require either regeneration or periodic replacement represents a layer of unacceptable system complexity. Therefore, the ultimate goal of reforming technology is to develop more sulfur-tolerant catalysts.

Substantial progress has been made to describe the interaction between Ni-based SR catalysts and sulfur compounds such as H_2S. It is generally accepted that there are two possible means by which sulfur can diminish the activity of the Ni catalyst (*Sehested*, 2006; *Rostrup-Nielsen*, 1968; *Rakass et al.*, 2006; *Ashrafi et al.*, 2008). The first method is important especially at high sulfur concentrations and is described as a direct chemisorption and dissociation of H_2S (Reaction 1.6), which blocks the adsorption of other compounds to the Ni surface.

$$Ni + H_2S \rightarrow NiS + H_2 \tag{1.6}$$

The second interaction occurs when adsorbed sulfur causes a restructuring of the catalyst, either in terms of physical rearrangement of sites or by altering the chemical nature of the sites. The consequence of this restructuring is that the adsorption characteristics of reactant molecules are negatively impacted. This type of interaction can impede the activity of Ni at even low coverages of sulfur on the catalyst surface. The equilibrium coverage of sulfur under various reaction conditions has been described by *Alstrup et al.* (1981); *Rostrup-Nielsen* (1968). Based upon these studies it can be expected that even at elevated reaction temperatures such as 800°C a minimal concentration of only 5 ppmv S can negatively impact the activity of a Ni reforming catalyst.

It is possible to regenerate Ni catalysts which have been deactivated by minimal sulfur exposure. Controlled exposure to either H_2 or O_2 has been shown to decrease

the presence of sulfur on Ni catalyst surfaces (*Rostrup-Nielsen*, 2002; *Rostrup-Nielsen*, 1984; *Rostrup-Nielsen*, 1968, 1971; *Alstrup et al.*, 1981; *Hepola and Simell*, 1997). Yet, these approaches may themselves lead to a drop in catalyst activity due to sintering.

Unfortunately, there is not a well developed molecular-level understanding of the poisoning behavior of sulfur under ATR conditions. The complex chemical nature of this reaction is epitomized by thermal and redox gradients through the reactor. The influence of sulfur containing compounds on these disparate reactive environments is not well understood. However, research has been undertaken by various groups to describe the effect of model sulfur compounds or actual commercial fuels on overall reformer performance.

While it is difficult to draw specific fundamental insights from the breadth of literature that exists regarding systems of disparate active site formulation, there are some general thematic consistencies and approaches which are important to note. For example, one consistent approach is the use of bimetallic and doped materials. For example, *Strohm et al.* (2006) found that the coupling of Ni with Rh led to increased stability compared to Rh alone due to the preferential adsorption of sulfur to the Ni sites. Other approaches have seen the pairings of Ni-Co, Ni-Pt, Pt-Pd, Ni-Re, Ni-Mo, Ni-Sr as well as the pairing of support materials and the addition of zeolites (*Murata et al.*, 2007; *Wang et al.*, 2004a; *Choudhary et al.*, 2007). These studies offer promise that a solution may be reached using creative catalyst formulation techniques.

This dissertation explores some of the gaps which exist in understanding the complex ATR system. While prior researchers have generally sought to merely compare the performance of new catalyst materials when they are exposed to sulfur-containing hydrocarbon feeds, the work discussed in this thesis takes a markedly unique approach. The adjustable parameters of ATR operation and catalyst formulation were used as experimental tools to ask probing questions of the internal chemistry. Application of the new knowledge which resulted from these efforts offers the greatest

hope of the eventual development of more sulfur-tolerant reformers.

Chapter II introduces the reader to the tools used to answer these fundamental questions. The synthesis process for the supported nickel catalysts is described, while outlining the key properties of the material. Then, the construction and design of an ATR reactor is detailed. This reactor was unique in that it allowed for reliable and reproducible identification and quantification of dilute sulfur containing compounds. Finally, some preliminary studies are discussed which motivate the use of surrogate fuels in future experiments and provide a context for interpreting the results of those experiments.

The major experimental questions are explored comprehensively in Chapters III and IV. The first of these questions was how different reforming environments influence the sulfur poisoning phenomenon. The parameter space of an ATR reactor made it straight-forward to formulate an experimental plan which tested a Ni catalyst under conditions of elevated reliance on the chemical pathways for steam reforming, or alternatively those for partial oxidation. These experiments coupled with the analytical approach described in Chapter II were rewarded with very interesting insights. For example, it was discovered that the steam reforming activity of Ni is more vulnerable to the negative effects of sulfur exposure than the partial oxidation activity of the catalyst. However, sulfur tolerance could be achieved by manipulating the balance between the atomic feeds of hydrogen, oxygen and carbon, such that the elevated production of molecular H_2 was thermodynamically favored.

These results motivated further research to understand if certain types of catalytic sites were more prone to deactivation than others. This question prompted the design of the unique experiment which is described in Chapter IV. In this experiment, a series of Ni catalysts were synthesized such that they accentuated different types of Ni sites. This was achieved by intentionally aging catalysts in a controlled manner. Testing these catalysts demonstrated that designing catalysts which had an increased

ratio of sites which are known to have excellent steam reforming activity did not translate to catalysts of higher activity in an ATR reactor. This highlights how the complex ATR environment is difficult to describe by way of comparison to systems, such as a SR reactor, which are similar in terms of their chemistry.

These new insights were then applied to the study which is outlined in Chapter V. In that experiment bimetallic catalysts were synthesized and tested for ATR activity under sulfur exposure. The knowledge developed in the prior chapters is applied to help understand, for example, why Au-Ni catalysts are ineffective under sulfur exposure despite their desirable performance in terms of diminished carbon deposition. This study identified two catalysts which would prove exceptional targets of further inquiry. These two catalysts (Pt modified 10 wt% Ni/CZO and W modified 5 wt% Ni/CZO) showed higher initial activity and prolonged durability compared to unmodified monometallic Ni catalysts when exposed to a heavy dose of sulfur.

This dissertation provides new insight into ATR chemistry, especially in terms of the role that sulfur plays in deactivating Ni-based catalysts. The pointed experimental questions asked and the methodical approach taken to answer those questions yielded new potential strategies for developing ATR reactors which are more tolerant to the presence of sulfur.

CHAPTER II

Experimental Approach to Understanding Reforming Chemistry

This dissertation explores the catalytic production of synthesis gas (H_2 and CO) from hydrocarbon fuel. Of specific interest is the effect that sulfur-containing compounds have upon the activity of Ni-based catalysts. Major questions that will be explored involve understanding how the chemistry of reforming reactions (ATR, SR, and POX) are affected by the presence of sulfur and if certain catalytic properties play a role in determining susceptibility or tolerance to sulfur. A consistent experimental approach was employed to provide answers to many of these questions. This approach involved the synthesis of Ni-based catalysts supported upon a Zirconium modified Ceria support. These catalysts were then tested for their activity towards the reforming of model compounds (such as isooctane and thiophene) in a fixed-bed reactor which was designed to provide vital information on the chemical environment of the reformer. Additionally, various characterization techniques were also employed to probe crucial catalyst characteristics. Those techniques will be introduced and discussed as they are employed in the subsequent chapters. This chapter explains the details of the reactor design and discusses the general experimental approach

employed in this thesis.

2.1 Introduction to Catalyst Properties and Synthesis

The catalytic material used in this dissertation consisted of an active metal phase which was supported over a ceramic support. Supported catalysts are useful because the complex microstructure of the support provides a large amount of surface area on which the metal may be dispersed. A high dispersion of the metal ensures that a large number of surface sites are available to participate in the chemistry of interest.

The motivations for selecting Ni as the active phase were discussed in Chapter I. However, the selection of a proper support material is also important. *Wang and Gorte* (2001) has reported that when Ni is supported by an inert material, such as silica, the reforming activity is heavily deactivated by the deposition of carbon on the catalyst. Several different catalyst supports have been identified and studied for the reforming of hydrocarbons, including the α- and γ- phases of Al_2O_3, doped aluminas, and various modifications of ceria (*Schwank and Tadd*, 2010; *Laosiripojana and Assabumrungrat*, 2005).

Ceria (CeO_2) is of particular interest in reforming catalysis because of the mobile oxygen and oxygen vacancies present in the fluorite lattice of the material. This oxygen storage capacity, or ability to take-in or give-up oxide ions, is thought to facilitate the oxidation of carbon deposits leading to more stable reformer performance (*Wang et al.*, 2004b; *Pengpanich et al.*, 2002; *Zhu and Flytzani-Stephanopoulos*, 2001; *Montoya et al.*, 2000; *Pengpanich et al.*, 2004). Furthermore, it has been demonstrated that the inclusion of zirconium in the material improves the oxygen storage capacity, redox properties, thermal stability, and catalytic activity of the support (*Laosiripojana and Assabumrungrat*, 2005). *Balducci et al.* (1998) used computational methods to demonstrate that the this improvement is brought about by the decrease in the reduction energy of the $Ce^{4+/3+}$ couple and the segregation of atomic oxygen vacancies

at the energetically favored [110] and [111] crystal facets.

Further studies have demonstrated that the support and active material can work together in the reactor in a complicated manner. For example, *Pacheco et al.* (2003) has proposed a mechanism for the reforming of heavy hydrocarbons which is facilitated by the adsorption and dissociation of water on the support material. It also appears that support properties can affect the chemistry of the active metal. *Xu and Wang* (2005) demonstrated that the mixed oxide support was responsible for a lower reduction temperature of Ni and increases rates of methane POX over the catalyst.

The catalysts used in the studies described in this dissertation were all prepared in a similar manner. The modified ceria support was prepared first and then the active metal was added, or impregnated into the support pore structure. The empirical formula used for the support was $Ce_{0.75}Zr_{0.25}O_2$, which will be referred to in this thesis as CZO. CZO was prepared by coprecipitation of Ce and Zr from salts dissolved in deionized (DI) H_2O. For this reaction, 4M NH_4OH was used as the precipitating agent. It was added drop-wise to the solution to ensure a homogenous solution pH.

The resulting suspension of cerium-zirconium hydroxide was then continuously stirred for at least 20 hours. During this time, the mixture changed at first from a slight brown-gray color to dark purple, before reaching the final dark yellow color which indicated complete conversion to an oxide form. The support was then recovered from the solution via vacuum-filtration and dried at 100°C for at least 12 hours. The dried catalyst was then fired in a furnace to stabilize the pore-structure.

Addition of the active metal was achieved by a method known as incipient wetness impregnation. In this method, a solution containing the metal precursor is added such that it fills the pores of the support without any excess fluid. Following impregnation, the catalyst is then calcined a second time to decompose the nitrate ions from the metal precursor solution. At that point the catalyst is in a stable oxide form. Before reaction or characterization, the catalyst is heated under hydrogen flow in order to

reduce the Ni metal.

Based upon this synthesis method, there are several variables which can affect various properties of the catalyst. The metal loading of the catalyst is generally described in terms of the mass percentage of Ni, with values ranging between 0.1 and 10% considered in this dissertation. The gas environment and temperature at which the catalyst is exposed during each of the various steps in the synthesis protocol can also influence the catalyst properties.

2.2 Description of Flow Reactor Design

When testing the synthesized catalysts for their activity to the autothermal reforming reaction there are additional experimental parameters which will be used in this dissertation to define the inlet conditions. ATR is the reaction of a hydrocarbon based fuel with water and air to produce a hydrogen rich product stream. The stoichiometry of the reaction is defined by the ratio of those reactants. The H_2O/C and atomic oxygen to atomic carbon ratio (O/C) are used to describe that stoichiometry. An O/C below two is required to avoid complete oxidation of the fuel, while the H_2O/C is maximized in order to minimize carbon deposition. However, in many of the mobile applications of reforming technology, the H_2O/C ratio is practically limited by the availability of water. Additionally, the space velocity describes the relationship between the inlet gas flow-rate and amount of catalyst being tested.

Reactor experiments were carried out in a system designed and built specifically for the work described in this dissertation. The process flow diagram (PFD) for the reactor setup is shown in Figure 2.1. A bifurcated feed system allowed for two modes of operation. In the Startup/Shutdown Mode the catalyst was exposed to either reductant or inert flow, while the reactant stream was initiated on a separate line which was discarded to a waste container. In the Reaction Mode, the reactant stream was switched from the discard line to the reactor, while the alternate feed-line

was shut-off. This approach allowed for an instantaneous initiation of the reaction by exposing the catalyst to a complete flow mixture of the reactants. Additionally, this allowed for the immediate quenching of the catalyst bed in inert flow following reaction.

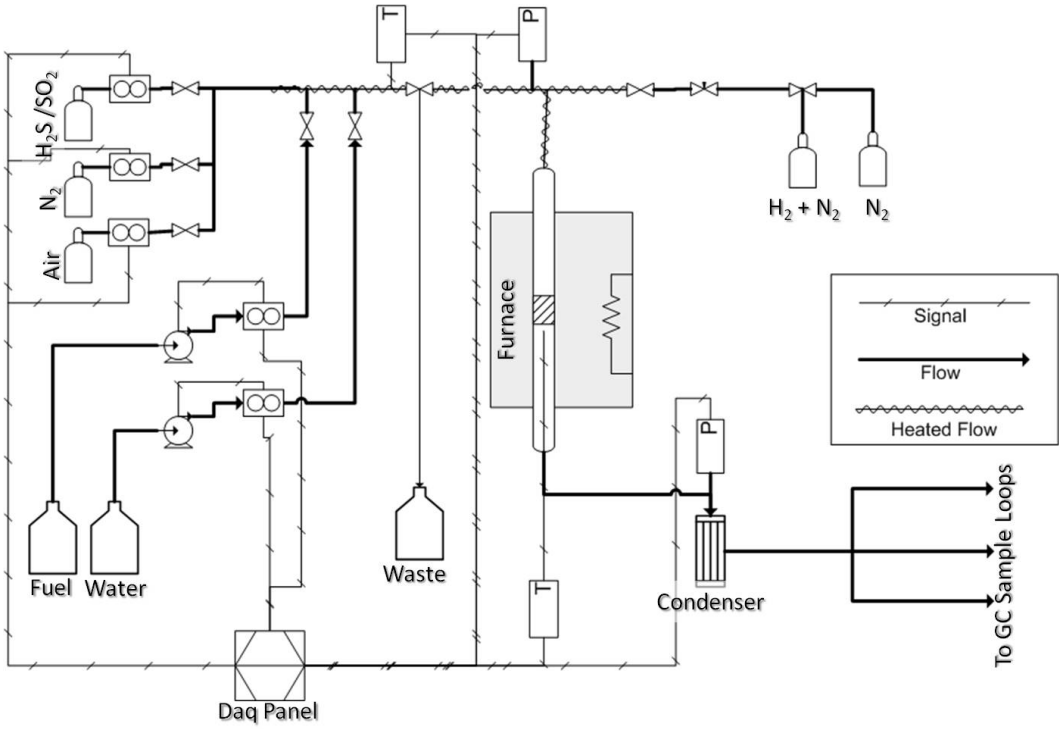

Figure 2.1: Process Flow Diagram for ATR reactor system.

Gas feed was supplied to the reactant streams from compressed cylinders (Matheson TriGas, Cryogenic) that were controlled by MKS Mass-Flo Series mass flow controllers. Liquid feed was achieved by a combination of Bronkorst L13-AAD-11-K-30S Digital Liquid Flow Meters which sent an analog control signal to Instech P625 peristaltic pumps. The alternate feed-line flowrate was manually controlled with a needle valve and Omega Rotameter.

The 1/4" and 1/8" o.d. stainless-steel feed lines used in for the reactor as well as all of the fittings were treated with the Restek Sulfinert coating. This coating provided the material with an inert silane-based surface which was not reactive with VSCs (*Smith*, 2006; *Barone*, 2003; *Smith*, 2006). Use of Sulfinert treated reactor

lines ensured that adsorptive losses of sulfur compounds in the reactant feed did not occur. This made it possible to feed an accurate and reproducible amount of sulfur at concentrations at the ppmv level.

The reactant lines were heated with Omega FGH Series Heating Tapes. The temperature of the feed lines was monitored with a thermocouple. All of the thermocouples used in the reactor were Omega K-type grounded probes with a 1/16" stainless-steel sheath. It was important to control the temperature of the reactant stream. A feed temperature of 180°C ensured complete evaporation of the water, without reaching a temperature sufficient to react any of the hydrocarbon fuel. Snubbed stainless-steel pressure transducers, obtained from Omega, were used to monitor the pressure upstream and downstream of the catalyst.

In all of the reaction conditions studied in this study, a reactor inlet temperature of 500°C was used. This temperature was sufficient to provide heat to start the reaction, in other words light-off the catalyst. This heat was provided by a Barnstead Thermolyne Furnace.

The reactor consisted of a 1/2" o.d. inert quartz tube. An image of the catalyst bed following light-off is seen in Figure 2.2 (left) next to a cross-sectional view of the reactor geometry (right). This figure illustrates both the design of the reactor as well as the radiative energy emitted from the front-face of the catalyst during an ATR reaction. In the design of the reactor, the catalyst bed was supported by plug of chromatography-grade quartz wool, which was in turn supported by three indentations made in the side wall of the quartz reactor tube. The quartz wool and the Teflon ferrule connecting the quartz reactor tube to the stainless-steel reactor lines were held in place by friction, which limited the pressure that could be sustained in the reactor. Prolonged pressure above 20 psig would lead to a failure of the seal at the Teflon ferrule or blow-through of the catalyst.

Along the center-line of the quartz reactor tube was a close-ended 1/8" o.d. quartz

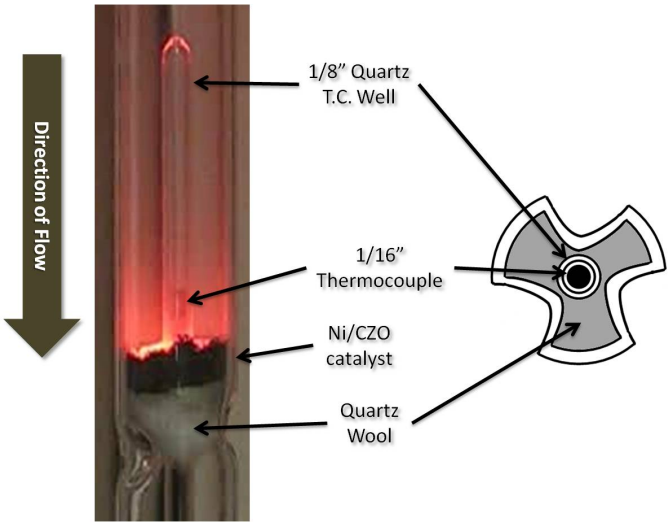

Figure 2.2: In-Situ Configuration of ATR reactor.

tube which was used as a thermocouple well. Inside the well was placed a 1/16" thermocouple which could be repositioned along the central axis of the reactor. This allowed measurement of in-situ temperature profiles which resulted in profound insight into the internal chemistry of the reformer.

The pressure transducers, thermocouples, and flow controllers were all interfaced in various ways with a National Instruments USB-6229 M Series DAQ board. A virtual instrument was developed in Lab View to monitor the reactor. The graphical user interface of this virtual instrument is displayed in Figure 2.3. This program provided set-points to the various control devices, monitored process variables, and provided PID control of two reactant line heating tapes.

2.3 Description of Analytical Setup

The reactor effluent from the system was fed into a single-stage condenser which was kept at 0°C. The condenser was necessary in order to prevent excessive water from flooding the analytical columns. The gas phase from the condenser was analyzed in a modified Varian CP-3800 Gas Chromatograph (GC). A simplified PFD of the system is displayed in Figure 2.4. The GC analyzed hydrocarbons from ethylene to

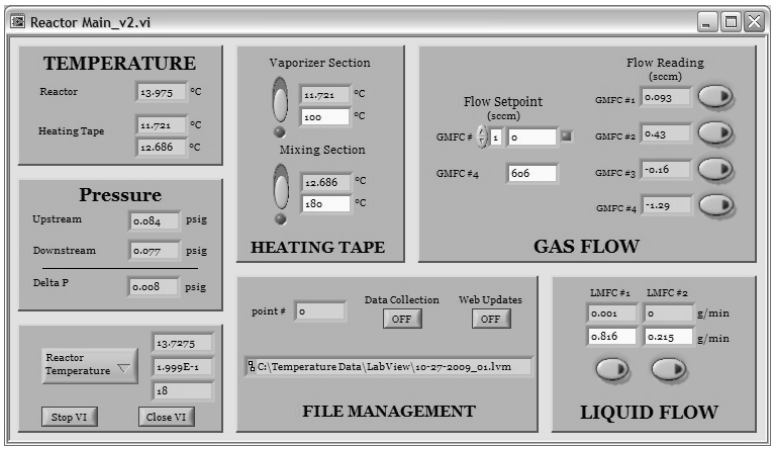

Figure 2.3: Interface of Reactor Control Virtual Instrument.

butylene, separated on a Alltech Carbosphere 1000 packed column, using a thermal conductivity detector (TCD). Lighter gases from hydrogen to methane were also analyzed on a TCD, and were separated on a HaySep DIP packed column. Sulfur compounds were separated on a Restek XLSulfur packed column and were analyzed in a Pulsed Flame Photometric Detector (PFPD). Three 10-port injection valves filled sample loops which were injected onto the three columns using Argon gas as the mobile phase/carrier gas. The volume of the sulfur analyte was 5 mL, while the other two sample loops were 0.1 mL. The larger volume of gas fed to the PFPD increased the sensitivity of the system.

The area of each eluted peak from the TCDs corresponded to the concentration of the given species, while the areas of each peak in the PFPD chromatogram were proportional to the number of moles of that sulfur-containing compound squared. Calibration curves (see Appendix A) were used to calculate the concentration of each species. A MATLAB interface was created (see Figure 2.5) to monitor the yield of various species and temperature and pressure data passed from the LabView virtual instrument.

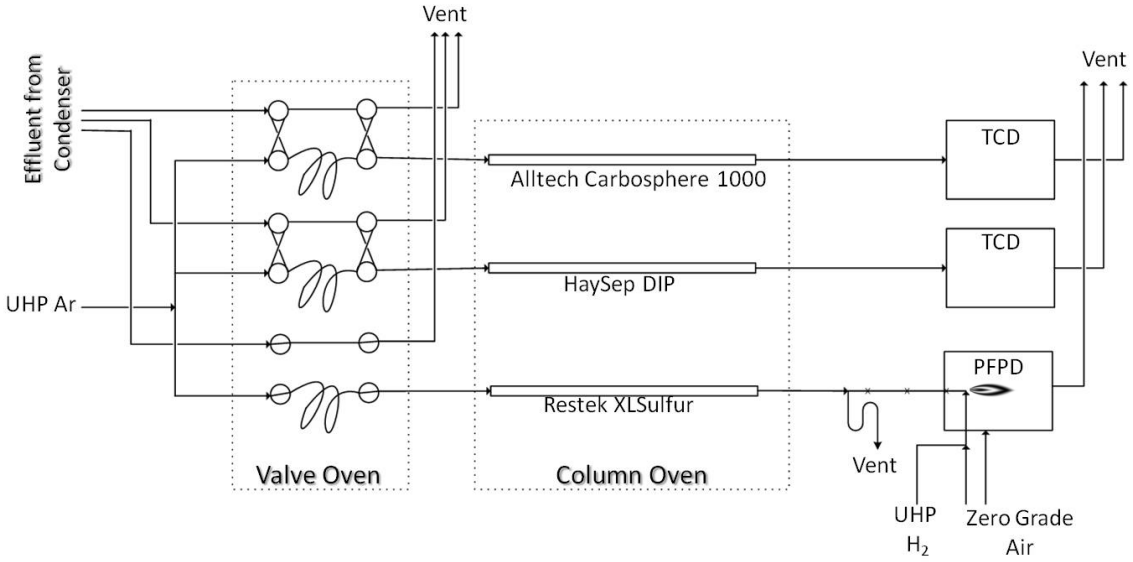

Figure 2.4: PFD of GC sample injection system.

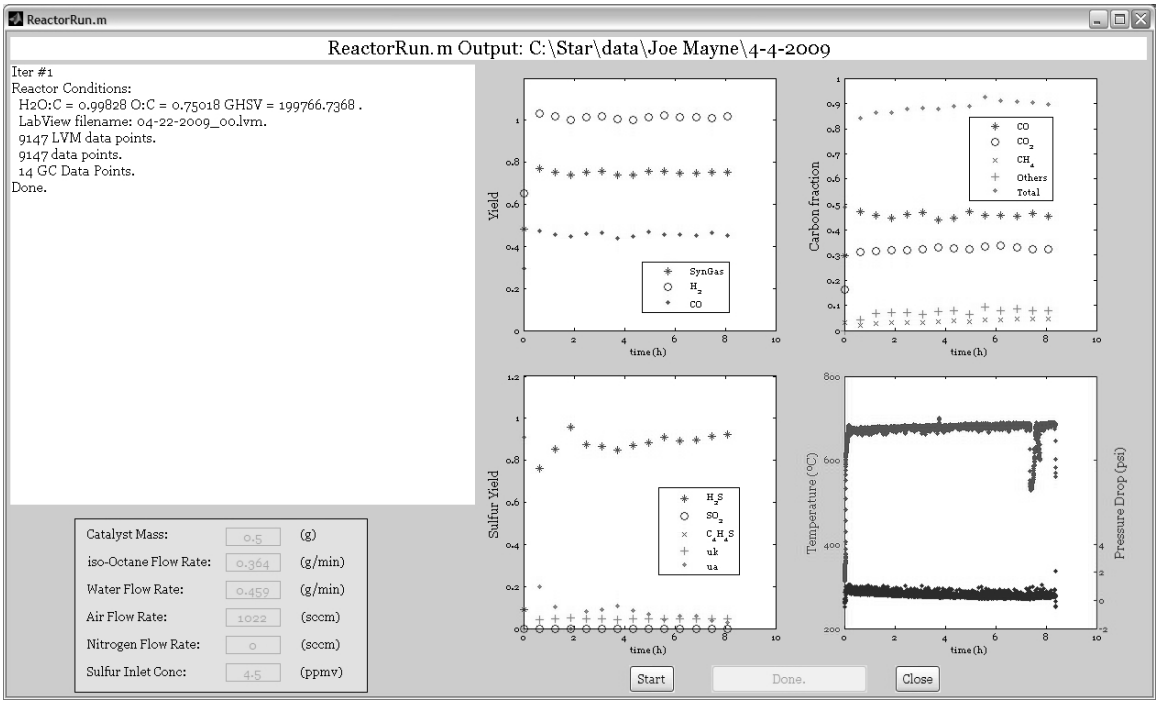

Figure 2.5: Graphical User Interface of Reactor Monitor Program.

2.4 Reforming of Gasoline and Surrogate Fuels

The reactor, as described above, was designed for the reforming of model compounds such as isooctane contaminated with thiophene. These mixtures were studied as a surrogate for the more complex fuel, commercial gasoline. The exact chemical composition of gasoline can vary considerably depending upon the source of the original petroleum and the refinery processing of the fuel. Composition data of the major species found in a sample of commercial gasoline are displayed in Table 2.1 (*Burri et al.*, 2004). That composition data is representative of a typical gasoline mixture, as it consists largely of C_5-C_8 paraffin and C_7-C_9 aromatic hydrocarbons, with additional contributions from napthalenes and olefin species. The sulfur compounds in gasoline are typically sulfides and thiophenes with a roughly equivalent carbon number distribution compared to non-sulfur-containing hydrocarbons (*Yin and Xia*, 2004).

C-number	Naphthenes	Paraffins	Cyclic Olefins	i,n-Olefins	Aromatics
4		0.73		0.15	
5	0.47	16.06	0.24	1.77	
6	2.68	10.76	0.69	3.54	0.88
7	1.07	6.22	0.52	1.63	15.33
8	0.57	2.23	0.14	2.37	16.24
9	0.11	0.37		0.29	8.98
10			0.07		0.84
Total wt%	4.90	36.37	1.66	9.75	42.27
Total vol%	4.76	42.03	1.57	10.56	36.21

Table 2.1: Chemical composition of an Example Sample of Commercial Gasoline. Reproduced from *Burri et al.* (2004)

This section compares the reforming behavior of gasoline obtained from a commercial filling station to a surrogate mixture of isooctane and thiophene. The reactor design was not ideal for the reforming of gasoline. The high volatility of gasoline was problematic for the liquid delivery system. A pressurized fuel delivery system would be more ideal for gasoline, but is not necessary for isooctane. Furthermore, as

the actual composition of the fuel was unknown, all of the yield calculations required an assumed empirical formula for gasoline ($C_{7.14}H_{14.28}$). The complex composition of gasoline leads to a reformate mixture with several unidentified hydrocarbon species.

Despite these drawbacks, ATR of the gasoline was maintained for over 40 hours over a 5 wt% Ni/CZO catalyst. The approximate feed conditions for this experiment were a H_2O/C ratio of 1, an O/C of 0.75, and a GHSV of 200,000 hr^{-1}. The yields of synthesis gas, Y_{SG}, and H_2S are displayed in Figure 2.6a. There was a slight decline observed in both yields as a function of time-on-stream. The carbon yields of CO, CO_2, CH_4, and the combined yields of ethylene, ethane, propylene, propane, and isobutylene are presented in Figure 2.6b at three different times. There were several additional peaks that were unidentified in the collected chromatograms. These peaks likely represent the remaining portion of the carbon balance.

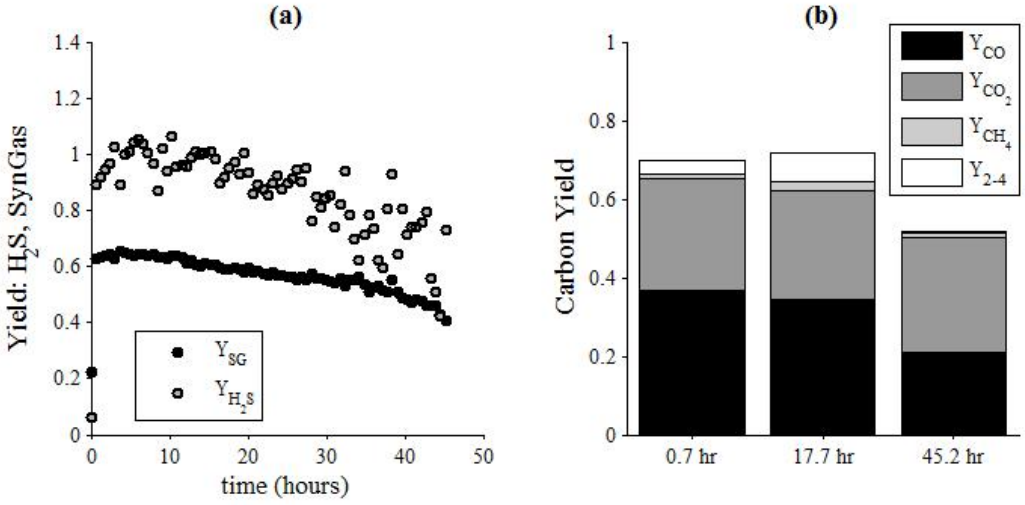

Figure 2.6: ATR of commercial gasoline over 5% Ni/CZO catalyst. The yields of synthesis gas and H_2S are depicted in (a) while the carbon fractions at three different times are shown in (b). (Approximate Reaction Conditions: $H_2O/C = 1$, $O/C = 0.75$, GHSV = 200,000 hr^{-1}, $S_{in} \approx 5$ ppmv.)

The results for the ATR of commercial gasoline are compared to the ATR of a corresponding surrogate mixture of isooctane and thiophene. The results from the surrogate fuel ATR experiment are shown in Figure 2.7. When comparing the two

experiments it is clear that there are benefits and shortcomings to considering surrogates in place of actual gasoline. The initial yields of synthesis gas and carbon species are very similar in the two experiments suggesting that performing the experiment with a surrogate mixture does a good job at describing the chemistry of the system. Also, in both cases it is evident that the sulfur contained in the fuel is initially converted entirely to H_2S.

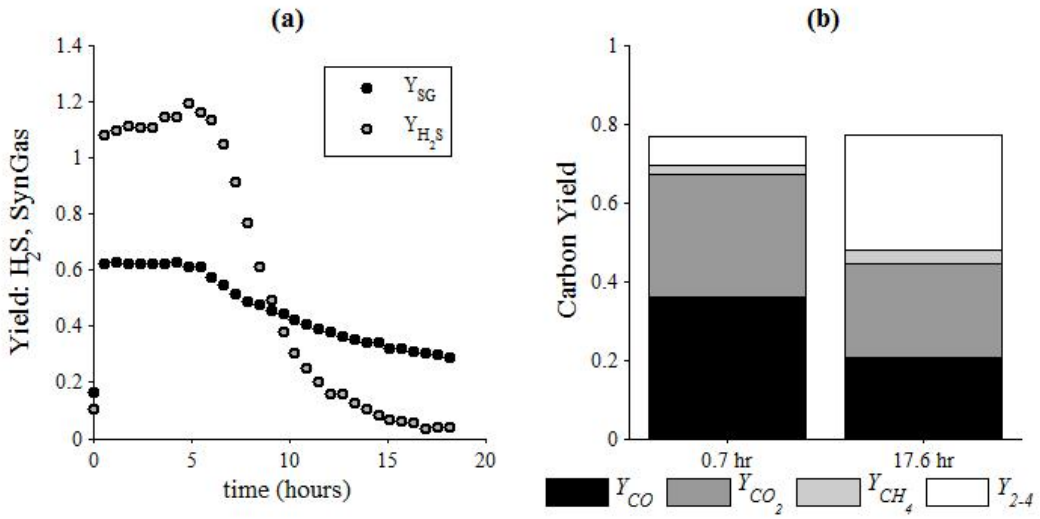

Figure 2.7: ATR of isooctane doped with thiophene (gasoline surrogate) over 5% Ni/CZO catalyst. The yields of synthesis gas and H_2S are depicted in (a) while the carbon fractions at three different times are shown in (b). (Reaction Conditions: $H_2O/C = 1$, $O/C = 0.75$, GHSV = 200,000 hr^{-1}, $S_{in} \approx 5$ ppmv.)

While the rate of deactivation is significantly higher for the surrogate mixture, there are clear advantages to studying the reforming of the simplified fuel. Considering fewer compounds simplifies the analysis of the reformate product. Perhaps most useful is that fundamental understanding of the chemistry is possible, as will become evident in the subsequent chapters, as separating the role of sulfur is made possible from not including thiophene in the surrogate mixture.

By comparing different surrogates for sulfur it was determined what influence the identity of the sulfur molecule has. This is what was done to produce the data in

Figure 2.8. As with the previous experiment, these runs were operated at a H_2O/C of 1, an O/C of 0.75, and a GHSV of 200,000 hr^{-1}. This time, the sulfur-free activity of isooctane was compared to experiments where a sulfur additive was introduced into the system 120 minutes into the experiment. The sulfur contaminant was either thiophene, H_2S, or SO_2, such that the inlet gas-phase sulfur concentration was approximately 6 ppmv. Each experiment was performed in triplicate in order to estimate the experimental error.

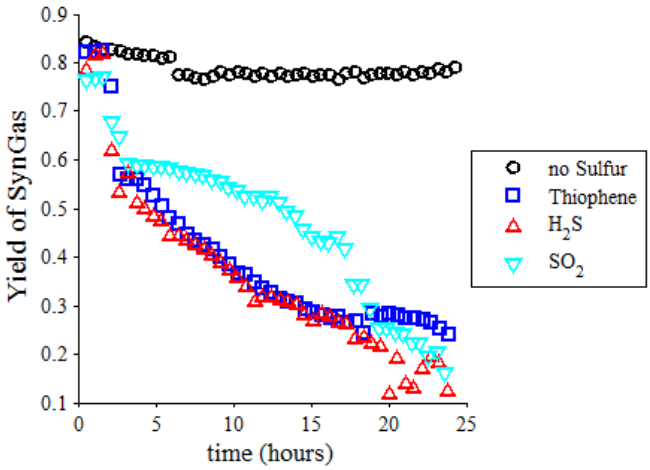

Figure 2.8: ATR of isooctane considering various sulfur poisons. (Reaction Conditions: $H_2O/C = 1$, $O/C = 0.75$, GHSV = 200,000 hr^{-1}, $S_{in} = 6$ ppmv.))

As soon as any sulfur was added to the system there was an immediate drop in activity. There did not appear to be a significant difference in the performance if sulfur was added as thiophene or H_2S for at least the first 20 hours on stream. In both cases, the activity continued to decline linearly with time-on-stream at these inlet conditions. However, when the sulfur was added as SO_2, the behavior was slightly altered. After the initial drop in activity, the subsequent decline was not as significant as it was during H_2S and thiophene exposures. This benefit was lost however above around 20 hours, at which point there was no significant difference between the sulfur types. Based upon the strength of interaction between the different types of sulfur

and a nickel surface, it could be expected that SO_2 would not interact as strongly with the support, and these results seem to corroborate that interpretation at the outset of sulfur exposure.

2.5 Non-Catalytic and Support Reforming Activity

When describing the activity of a particular catalyst formulation or a certain inlet condition, it is important to first establish the baseline of minimum performance and also the highest achievable production of the desired products. The upper boundaries on performance are defined by stoichiometric and thermodynamic limitations. These will be explored more fully in Chapter III for several different reforming conditions.

When considering the minimum baseline of catalyst activity, it is necessary to understand that a significant portion of the reactants fed to the reactor would be converted even in the absence of Ni in the catalyst formulation. In order to demonstrate and quantify this phenomenon, the production rates of various species were measured for a blank quartz reactor tube at two furnace temperatures. Additionally, the activity of the CZO support, without Ni present, was determined. For both of these experiments the inlet H_2O/C and O/C ratios were 1 and 0.75, respectively. In order to contextualize the results of the subsequent chapters, these experiments were operated such that they corresponded to a GHSV of 200,000 hr^{-1} if a 10 wt% Ni/CZO catalyst were being studied. Accordingly, the inlet molar flowrates were 3.19 mmole/min of isooctane, 25.5 mmole/min of water, and 45.2 mmole/min of air. The isooctane fuel was contaminated with thiophene such that the feed flowrate of thiophene was 9.6e-5 mmole/min.

The results for the blank tube experiments are shown in Table 2.2. These results demonstrate that when exposed to temperatures typical for catalyst beds in an ATR reactor, a significant portion of the isooctane fuel is already thermally decomposed and even homogenously oxidized before it reaches the catalyst bed. The PFPD

was able to detect a small amount of H_2S suggesting a very minimal conversion of thiophene in the homogeneous zone as well.

	675°C	775°C
H_2	0.26 mmole/min	1.49 mmole/min
CO	0.91	5.16
CO_2	0	0.27
CH_4	0.64	2.77
C_2H_4	0.1	0.83
C_2H_6	0.04	0.15
C_3H_6	0.47	1.03
C_3H_8	0.03	0.13
C_4H_8	0.87	0.80
H_2S	3.5e-8	7.25e-8
$X_{iC_8H_{18}}$	0.27	0.66
$X_{C_4H_4S}$	3.73e-4	7.72e-4

Table 2.2: Blank tube activity at isooctane ATR feed conditions (T = 675°C and 775°C). Molar flowrates of major species are listed along with the conversions of isooctane and thiophene at the two inlet Temperatures. (Reaction Conditions Corresponding to: $H_2O/C = 1$, $O/C = 0.75$, GHSV = 200,000 hr^{-1})

The activity of the CZO support is shown in Figure 2.9. The combined yield of CO and H_2 is plotted in Figure 2.9a. According to this trend, there is a significant initial production of synthesis gas which linearly decreases with time on stream. It is not apparent why the activity decreased with time. The yields for the carbon species produced are shown in Figure 2.9b for two points in the experiment (0.5 hours and 8 hours). These data demonstrate that near complete conversion of isooctane is achieved initially, but the conversion decreased with time-on-stream. It is important to note that all of the products found during the ATR of isooctane over a 10 wt% Ni/CZO catalyst are also present when considering reforming over CZO itself.

Examining the sulfur products present in the effluent (Figure 2.9c), it is apparent that CZO does not effectively convert thiophene to H_2S. The lagging breakthrough of thiophene suggests that a significant amount of thiophene is being adsorbed on the CZO. This suggests that the support may play a role in the interaction of thiophene

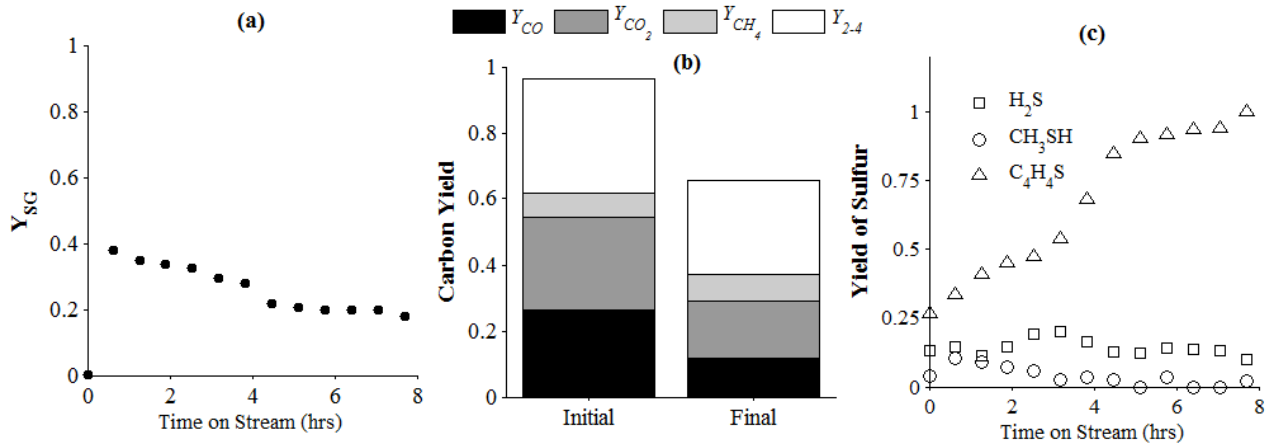

Figure 2.9: ATR of thiophene doped isooctane over CZO support: the yields of synthesis gas (a), carbon-containing species (b), and sulfur-containing species (c) are displayed. (Reaction Conditions: $H_2O/C = 1$, $O/C = 0.75$, GHSV = 200,000 hr^{-1})

with a Ni/CZO catalyst as well.

While the results delineated in Table 2.2 and Figure 2.9 provide a base-line for evaluating the reforming activity of a Ni/CZO catalyst, the infinite residence-time or equilibrium predicted gas-phase composition is the practical limitation on what may actually be achieved in a reformer. To illustrate this, refer to Figure 2.10. This figure depicts the dry, nitrogen-free mole fraction as a function of the Extent of Reaction, ξ, from blank tube activity at 675°C. Therefore, the composition of the homogeneous reaction products is shown at the left-hand side of the plot and the right-hand side of the plot shows the composition at 675°C once the Gibbs free energy of the system has been minimized. The composition at each value of ξ is derived based upon the formal definition of Extent of Reaction, given in Equation 2.1.

$$\xi = \frac{(N - N_{blank})}{(N_{equil} - N_{blank})} \tag{2.1}$$

In this expression, N refers to the number of moles of a given species at a specific value of ξ, and the subscripts $_{equil}$ and $_{blank}$ refer to respective molar values at equilibrium and as obtained from the blank tube experiment.

Based upon this analysis, it is clear that the role of the catalyst is to produce the vast majority of the hydrogen, the desired product of the chemistry, and react away all of the homogeneous cracking products. Due to the derivatives of the curves in Figure 2.10, it is apparent that small deviations away from thermodynamic equilibrium would result in a most significant measuable differences in the concentrations of H_2 and hydrocarbon intermediates, such as propylene and isobutylene.

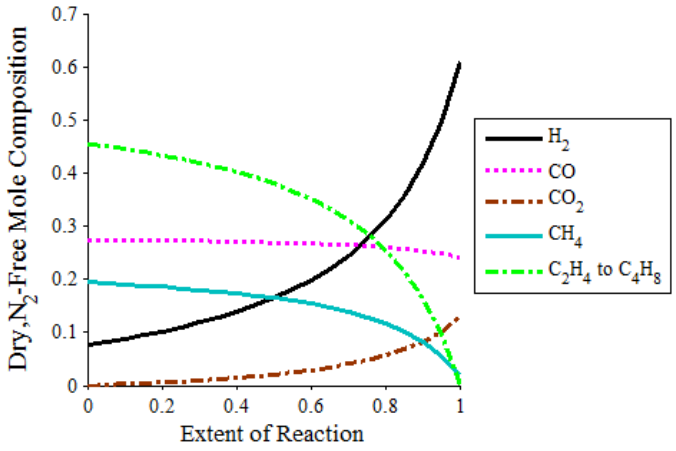

Figure 2.10: Approach to equilibrium (right-hand side) from the blank tube activity (left-hand side). (Reaction Conditions correspond to: $H_2O/C = 1$, $O/C = 0.75$)

CHAPTER III

Influence of Thiophene on the Isooctane Reforming Activity of Ni Based Catalysts[1]

Catalytic reforming of liquid hydrocarbon fuels is challenging due to potential deactivation due to carbon deposition and sulfur poisoning. To gain a better understanding of the effect of sulfur on the deactivation of $Ni/Ce_{0.75}Zr_{0.25}O_2$ catalysts, isooctane conversion to syngas was studied in presence of small amounts of thiophene under various O/C and H_2O/C ratios representing steam reforming, partial oxidation, and autothermal reforming conditions. It was found that depending on the reaction conditions, thiophene underwent different degrees of desulfurization, leading to the formation of H_2S. Under reaction conditions leading to nearly complete conversion of thiophene to H_2S, the nickel catalyst lost only a small amount of its initial activity, but then maintained stable performance over longer times on stream. In contrast, reaction conditions allowing thiophene to emerge unconverted from the reactor led to severe and continued deactivation of the catalysts. Furthermore, co-feeding thiophene with isooctane caused significant increases in the temperature profile of the reactor and an increased amount of olefins were seen as products of the reaction, in-

[1]This chapter appeared in The Journal of Catalysis, volume 271, page 140.

dicating that sulfur deactivated primarily endothermic steam reforming reactions, while having less impact on exothermic partial oxidation reactions. Controlling the reaction conditions in such a way as to generate sufficient hydrogen concentrations in the catalyst bed for effectively desulfurizing thiophene to H_2S appears to be the key to maintaining stable catalytic activities in the presence of sulfur compounds.

3.1 Introduction

The processing of liquid fuels, such as gasoline, into hydrogen-rich gas streams would prove attractive to such varied applications as auxiliary power units, cold-start engine ignition and potential emission control strategies. Possible catalytic reforming approaches include SR (3.1), POX (3.2), and ATR (3.3). SR is the common large-scale production route for synthesis gas from methane, and produces the most hydrogen of the three reforming options by reacting hydrocarbon fuels with an excess of steam. POX employs a sub-stoichiometric co-feed of oxygen and results in a lower yield of hydrogen than SR. The ATR reaction offers a compromise between the prohibitive heat transfer demands of steam reforming and the excessive carbon deactivation of partial oxidation, with the added benefit of a tunable process heat duty (*Krumpelt et al.*, 2002).

$$C_xH_y + xH_2O \rightarrow \left(\frac{y}{2} + x\right) H_2 + xCO \tag{3.1}$$

$$C_xH_y + \frac{x}{2}O_2 \rightarrow \frac{y}{2}H_2 + xCO \tag{3.2}$$

$$C_xH_y + (x - 2z)\, H_2O + zO_2 \rightarrow \left(\frac{y}{2} + x - 2z\right) H_2 + xCO \tag{3.3}$$

Autothermal reforming of various hydrocarbons has previously been investigated on both noble and non-noble metal-based catalysts (*Navarro et al.*, 2006; *Pino et al.*,

2006; *Koga et al.*, 2006; *Barison et al.*, 2007; *Nilsson et al.*, 2007; *Flytzani-Stephanop. and Voecks*, 1983; *Nagaoka et al.*, 2004). While noble metal catalysts generally offer higher activity and lower carbon formation than non-noble metals, their implementation may be cost-prohibitive. The use of nickel in reforming catalysis is attractive from an economic perspective, but Ni catalysts have several significant drawbacks that limit their performance (*Sehested*, 2006), including carbon deposition, loss of active sites due to nickel particle growth, or sintering, and sulfur poisoning. Carbon deposition on Ni-based catalysts can be inhibited by supporting the metal over a zirconia-modified ceria support, whose redox behavior helps decrease the amount of carbon formed during reforming reactions (*Laosiripojana and Assabumrungrat*, 2005; *Shekhawat et al.*, 2006; *Chen et al.*, 2007).

Perhaps the most intractable impediment to catalytic fuel reforming is the challenge posed by sulfur poisoning. Mercaptans, thiophenes, benzothiophenes, and dibenzothiophenes are found as contaminants or additives at various concentrations in the major hydrocarbon-based feeds to proposed fuel reforming systems. The interaction of these species with the catalyst can lead to active-site poisoning. Such behavior has been shown to be long-range in character; consequently even low levels of sulfur exposure (less than 1 ppmv) can cause significant changes in catalyst activity and selectivity (*Rodriguez et al.*, 1999). The development of more sulfur-tolerant reformers hinges on the ability to understand the interaction of these sulfur contaminants on a complex chemical system.

The goal of the research discussed in this Chapter was to develop a better understanding of the effect of sulfur on Ni-based ATR catalysts. The effectiveness of Ni supported on $Ce_{0.75}Zr_{0.25}O_2$ (CZO) for the ATR of 2,2,4-trimethylpentane (isooctane) and n-dodecane under sulfur-free conditions has been reported previously (*Tadd et al.*, 2005; *Gould et al.*, 2007). In the current study, the influence of thiophene on the reforming of isooctane is investigated under a range of ATR conditions, and under pure

POX and SR conditions. Substantial progress was made towards the understanding of sulfur deactivation in catalytic fuel reformers through novel analytical and experimental strategies. Reaction conditions were chosen which bounded typical reforming experiments, and considered stoichiometric and thermodynamic limitations. The in situ temperature profiles of the reformer, the identification and quantification of sulfur-containing products, and the effects of thiophene exposure upon measureable changes in catalyst morphology provided a more thorough description of reforming behavior.

3.2 Experimental

3.2.1 Catalyst Preparation

For the purposes of this study a single batch of 10 wt% Ni supported on CZO was prepared. This loading level is higher than has been previously recommended for optimal carbon deposition behavior (*Gould et al.*, 2007), but was selected for this study because the larger Ni crystals that result are easily characterized with X-Ray Diffraction (XRD) and Scanning Electron Microscopy (SEM). The support was prepared by the co-precipitation of Ce and Zr from $Ce(NO_3)_3{\cdot}6H_2O$ and $ZrOCl_2{\cdot}8H_2O$ in DI water, using a 4 M solution of NH_4OH as a precipitating agent. The precipitate was filtered and washed with DI water and then calcined in air at a temperature of 900°C for two hours. The support material was impregnated with an aqueous solution of $Ni(NO_3)_2{\cdot}6H_2O$ via incipient wetness. The catalyst precursor was then calcined at 900°C for two hours. The calcination temperature was chosen such that it exceeded maximum catalyst bed temperatures during reforming experiments, and was intended to thermally stabilize the material. The Ni/CZO catalyst was size-fractioned, and particles between 250 and 420 microns were retained for study. Particles of this size were found to give the most favorable flow behavior during reforming experiments,

preventing catalyst-bypass and excessive pressure drop.

3.2.2 Reforming Experiments

3.2.2.1 Experimental Design

The prepared catalyst was tested for activity to reforming of isooctane, a surrogate for gasoline, under sulfur-free conditions and with thiophene present. Table 3.1 shows the experimental reforming conditions considered. In each experiment, 500 mg of catalyst was loaded into the reactor, and a total gas hourly space velocity (GHSV) of 200,000 hr^{-1} was used for the reactant stream. The conditions for the Base Case were chosen to represent harsh yet manageable ATR conditions, in terms of carbon deposition and sintering, and such that the produced reformate stream was very near thermodynamic equilibrium under sulfur-free operation. The influence of sulfur tolerance under increasingly POX-dominated conditions was studied by considering an elevated O/C and pure POX conditions. Likewise, the role of sulfur in an increasingly SR-dominated environment was studied by an elevated H_2O/C and pure SR conditions. For consistency, an inlet temperature of 500°C was employed for each of the compositions. Additionally, the SR experiments were also tested at the more industrially relevant temperature of 750°C.

Assuming that nitrogen is non-reactive under reforming conditions, carbon, oxygen and hydrogen are the reactive elements in a reformer system (neglecting the relatively low concentration of sulfur and the catalyst material). The balance of these three elements in the design of a reforming system allows for the tuning of carbon deposition behavior, heat duty, product composition, and safe operation. Figures 3.1a and 3.1b show ternary diagrams for these three elements. Each point on the ternary plot may be taken to represent the elemental balance for a given set of inlet conditions. Tie-lines on the diagram represent the steam reforming of isooctane (i), the gasification of elemental carbon (ii), the partial oxidation of isooctane (iii), and the

Scenario	H_2O/C ratio	O/C ratio	$F_{iC_8H_{18}}$ (mmole/min)	F_{H_2O} (mmole/min)	F_{O_2} (mmole/min)	F_{N_2} (mmole/min)	S_0 (ppmv)
Base Case	1	0.75	3.19	25.5	9.56	35.64	4.500
Elevated O	1	1	2.64	21.2	10.58	39.42	3.736
Pure POX	0	0.75	4.85	-	14.55	54.24	6.855
Elevated Steam	3	0.75	1.82	45.2	5.47	20.37	2.667
Pure SR	3	0	1.82	45.2	-	25.84	2.667

Table 3.1: Reforming scenarios considered. The atomic sulfur concentration refers to the inlet concentration into the reactor.

desired products of reforming, H_2 and CO (synthesis gas, iv). The bold portion of the partial oxidation line represents the flammability region of isooctane in air at atmospheric pressure.

Open marks in Figure 3.1a represent experimental conditions used in previous studies of the effects of sulfur contamination on hydrocarbon reforming (*Shekhawat et al.*, 2006; *Qi et al.*, 2007; *Goud et al.*, 2007; *Dinka and Mukasyan*, 2007; *Cheekatamarla and Lane*, 2006; *Cheekatamarla and Thomson*, 2006; *Cheekatamarla and Lane*, 2005; *Murata et al.*, 2007; *Wang et al.*, 2004a; *Strohm et al.*, 2006; *Lakhapatri and Abraham*, 2009). These studies showed strikingly similar inlet C-H-O compositions employed across a broad range of hydrocarbon fuels (C_7H_{14} to $C_{14}H_{30}$) which can be attributed to a common desire amongst researchers for low carbon deposition rates, conventionally achieved through high H_2O/C ratios. Only one of the studies chose a feed composition which lay directly on the synthesis gas tie-line (*Cheekatamarla and Thomson*, 2006), the idealized goal of reforming. However, that inlet condition was particularly harsh in terms of carbon deposition. The researchers achieved a product stream of almost pure synthesis gas but also reported excessive carbon deposition and sulfur poisoning of their Mo_2C catalyst.

The conditions chosen in this study are depicted in Figure 3.1b (closed symbols). The Base Case scenario lies on the edge of the typical operating region for reforming systems, where higher carbon deposition rates are expected. The Elevated H_2O and the Elevated O cases lie on the low and high carbon edges, respectively, of the region with the highest density of ATR experiments. The Pure POX case lies above the higher flammability limit of isooctane in air and is well within the region where higher carbon deposition rates are expected. The Pure SR case falls on the low H_2O/C side of the region of typical SR experiments.

The ternary diagram was used together with equilibrium calculations to predict the chemical makeup of the product gas. The equilibrium predicted gas compositions

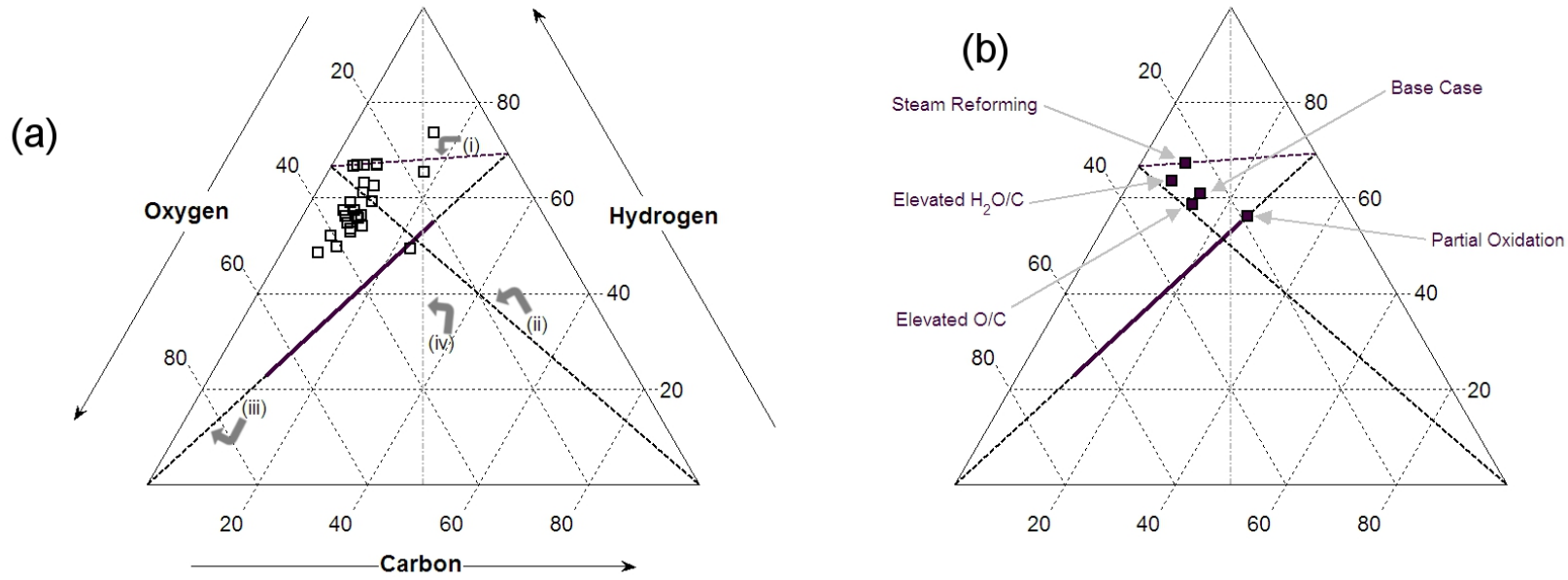

Figure 3.1: C-H-O ternary diagrams based on total feed composition. 3.1(a) shows feed mixtures explored used during the investigation of sulfur effects on the reforming of various hydrocarbon feeds (*Shekhawat et al.*, 2006; *Qi et al.*, 2007; *Goud et al.*, 2007; *Dinka and Mukasyan*, 2007; *Cheekatamarla and Lane*, 2006; *Cheekatamarla and Thomson*, 2006; *Cheekatamarla and Lane*, 2005; *Murata et al.*, 2007; *Wang et al.*, 2004a; *Strohm et al.*, 2006; *Lakhapatri and Abraham*, 2009). 3.1(b) shows the feed mixtures chosen for this study. In both Figures: the line labeled (i) represents the combinations of C_8H_{18} and H_2O (pure SR); likewise, (ii) represents elemental carbon and H_2O; (iii) represents C_8H_{18} and O_2 (pure POX), with the bold portion signifying the flammability region; and (iv) represents synthesis gas compositions.

were determined for each of the inlet scenarios using the Gibbs free energy minimization method in ASPEN Plus. For these calculations the reactor was assumed to be adiabatic, with initial temperatures the same as employed in the experiments (500°C or 750°C). The product concentrations of key components for each scenario are listed in Table 3.2. Based on these calculations, the equilibrium concentration of H_2 in the product stream should follow the trend: Base Case > Elevated H_2O > Elevated O > Pure SR (750°C) > Pure POX > Pure SR (500°C).

Scenario	T(°C)	H_2(%)	CO(%)	CO_2(%)	CH_4(%)	C_2H_4 to C_4H_8 (%)
Base Case	711.39	35.98	15.09	6.71	0.46	0.00
Elevated O	1003.69	27.43	15.03	4.95	0.00	0.00
Pure POX	1108.26	22.00	24.51	0.00	6.59	0.78
Elevated Steam	679.95	30.69	5.30	9.92	0.08	0.00
Pure SR (500°C)	407.74	12.18	0.18	6.74	10.58	0.00
Pure SR (750°C)	496.54	23.26	1.20	8.49	6.68	0.00

Table 3.2: Predicted exit temperatures and equilibrium gas compositions of key products for the scenarios tested, assuming adiabatic minimization of Gibbs free energy.

Experimentally, each scenario was tested in duplicate under sulfur-free conditions. To determine the influence of thiophene at each set of conditions, each scenario was also tested in duplicate using isooctane containing thiophene. The concentration of thiophene in the isooctane stream for these experiments was 77.19 ppmw, or equivalently 29.42 ppmw atomic sulfur. This concentration was selected on the basis of the 2000 Tier 2 Vehicle & Gasoline Sulfur Program Final Rule, which set the EPA guidelines for sulfur content in gasoline. This regulation specifies that the annual average sulfur content of gasoline was not to exceed 30 ppmw for any gasoline producer by the year 2004 (*EPA*, 2000). The resulting inlet volumetric concentration of atomic sulfur fed into the reformer at each inlet condition is given in the final column of Table 3.1. The thiophene concentration in the fuel was verified by means of a Varian PFPD installed on a Varian CP-3800 GC.

3.2.2.2 Flow Reactor Description

For each of the reactor experiments the catalyst was loaded into a 1/2 inch outer-diameter quartz reactor tube where it was supported by coarse-fibered quartz wool. The reactor assembly included a thermocouple shielded within a thermowell, a close-ended 1/8 inch quartz tube. Temperature profiles during the flow experiments were measured by repositioning the thermocouple within the thermowell. The reactor system was loaded into a vertical Thermolyne furnace, and was operated in a down-flow configuration. Omega pressure transducers monitored the pressure upstream and downstream of the catalyst bed. The flow system consisted of MKS Flow Controllers for gas delivery and Bronkhorst Liquid Flow Controllers, which controlled Instech peristaltic pumps, for the delivery of liquids. 2,2,4-Trimethylpentane and thiophene were obtained from Sigma Aldrich (>99% purity). DI water was used as the steam source. The feed lines were heated to a temperature of 180°C using Omega heating tape in order to vaporize the liquid feed.

The effluent from the reactor was passed through a single-stage condenser to trap excess water and prevent flooding of the GC columns. The gas phase from the condenser was analyzed using a Varian CP-3800 GC. The lighter components, H_2, O_2, N_2, CO, CH_4, and CO_2, were separated on a Haysep DIP packed column and quantified using a TCD. Heavier hydrocarbons, such as ethylene, ethane, propylene, propane, and isobutylene, were separated on an Alltech Carbosphere 1000 packed column and were also quantified using a TCD. Volatile Sulfur Compounds (VSCs), such as H_2S, methanethiol and SO_2, were separated on a Restek XLSulfur packed column and analyzed with a PFPD, whose operation was specifically optimized for atomic sulfur sensitivity and selectivity. The analytical setup also allowed for the detection of isooctane and thiophene in the condenser. However quantification of these condensable species was indirect because the gas-phase composition of these two chemicals was dependent upon their respective vapor-pressures at the condenser

operating temperature. For each experiment, the presence or absence of condensable products was noted and the concentration of thiophene was normalized to its steady-state value, providing an estimation of the transient concentration of thiophene.

Stainless-steel lines and related fittings for the entire system were treated with Restek/Silcotek Sulfinert coating, which provided an inert silane surface to the flow path (*Smith*, 2006; *Barone*, 2003; *Smith*, 2006). This limited adsorptive losses of VSCs, which was a significant strength of this study (*Gramshaw and Hussain*, 1978; *Wardencki*, 1998).

3.2.2.3 Reactor Startup and Shutdown

Prior to reaction the Ni/CZO catalyst was reduced under a flow of 5% H_2 in N_2 at 600°C. For the ATR and POX experiments the catalyst was then cooled under N_2 to an initial reactor temperature of 300°C. A dual-feed setup allowed the reactant flow to equilibrate before the reaction was initiated. The time at which the flow over the catalyst was switched from N_2 to the reactant stream was taken as the initial time of the experiment. Catalytic light-off occurred immediately upon exposure to the reactant feed in all ATR and pure POX cases and was indicated by a sharp rise in catalyst temperature of at least 100°C and a slight increase in reactor pressure drop. The furnace temperature was increased at 10°C/min to achieve a final reactor feed temperature of 500°C. It has been reported previously that by starting the experiment at a lower initial temperature then ramping to the final feed temperature limits undesirable transient temperature spikes (*Gould et al.*, 2007). Air in the ATR and POX experiments was substituted with pure N_2 in the SR experiments, in order to maintain the same space velocity for all experiments. The SR experiments were carried out at a constant furnace feed temperature of either 500°C or 750°C.

The activity and selectivity of the catalyst under each condition was monitored for 500 minutes. Temperature profiles of the catalyst bed were measured at steady-

state conditions. Following the experiment, the catalyst bed was cooled under N_2 flow to help preserve the chemical state of the catalyst. Prior to any post-reaction characterization the entire sample was finely ground to thoroughly mix the sample, and thereby minimize sampling error due to inhomogeneity.

3.2.2.4 Analysis of Reforming Behavior

The GC quantification provided the dry mole fractions of non-condensable species at a time interval of approximately 35 minutes. The molar flowrates, F_X, of each component were calculated using N_2 as an internal standard. These flow-rates were used to calculate the yields for key components (expressions 3.4-3.12). The carbon balance was calculated by summing the yields of carbon-containing products. Under conditions with 100% isooctane conversion the carbon balance closed to within 5%.

$$Y_{H_2} = \frac{F_{H_2,out}}{9 * F_{C_8H_{18},in}} \tag{3.4}$$

$$Y_{CO} = \frac{F_{CO,out}}{8 * F_{C_8H_{18},in}} \tag{3.5}$$

$$Y_{SG} = \frac{(F_{H_2} + F_{CO})_{,out}}{17 * F_{C_8H_{18},in}} \tag{3.6}$$

$$Y_{CO_2} = \frac{F_{CO_2,out}}{8 * F_{C_8H_{18},in}} \tag{3.7}$$

$$Y_{CH_4} = \frac{F_{CH_4,out}}{8 * F_{C_8H_{18},in}} \tag{3.8}$$

$$Y_{2-4} = \frac{(2 * F_{C_2H_4} + 2 * F_{C_2H_6} + 3 * F_{C_3H_6} + 3 * F_{C_3H_8} + 4 * F_{C_4H_8})_{,out}}{8 * F_{C_8H_{18},in}} \tag{3.9}$$

$$Y_{H_2S} = \frac{F_{H_2S,out}}{F_{C_4H_4S,in}} \tag{3.10}$$

$$Y_{C_4H_4S} = 1 - X_{C_4H_4S} \approx \frac{F_{C_4H_4S,out}}{max\,(F_{C_4H_4S,out})} \tag{3.11}$$

$$Y_{CH_3S} = \frac{F_{CH_3S,out}}{F_{C_4H_4S,in}} \tag{3.12}$$

The synthesis gas yield (Y_{SG}) is considered for the purposes of this study to be the

most useful single-parameter measure of reforming activity and selectivity. Table 3.3 shows the Y_{SG} calculated based upon the idealized reaction stoichiometry and the calculated adiabatic equilibrium results. The idealized reaction stoichiometry, as defined in Reaction 3.3 is considered the best possible outcome since the only products considered are H_2 and CO under ATR and SR conditions. These stoichiometrically limited product compositions can also be found using a simple construction using a C-H-O ternary plot, as shown in Figure 3.2. A line is drawn between the reactor composition and the point representing pure water. This line intersects the line representing pure synthesis gas at the stoichiometrically constrained H_2/CO ratio. The stoichiometric limitations of POX are complicated by the sub-stoichiometric oxygen feed requirement for safe operation. The additional carbon in the POX feed was assigned here to ethylene. For all scenarios, equilibrium calculations provide more conservative constraints to Y_{SG} as they consider both the energetic state of the inlet conditions and the presence of undesired products at their thermodynamically favored concentration. In general, the equilibrium calculated Y_{SG} maxima are lower than stoichiometric limited Y_{SG} values due to the presence of compounds such as CO_2 and CH_4 at equilibrium.

3.2.3 Catalyst Characterization

Physical surface area measurement of the prepared catalyst was performed using the single-point BET N_2 physisorption technique on a Quantachrome ChemBET instrument. The metallic surface area and dispersion were determined using H_2 chemisorption on a Micromeritics ASAP 2020 instrument, with the procedure given previously (*Gould et al.*, 2007).

Gravimetric analyses of Temperature Programmed Oxidation (TPO) profiles were performed on a TA TGA Q500 instrument. Samples were heated from 100 to 900°C at 10°C/min under a flow of 60 mL/min air and 40 mL/min nitrogen to identify

Scenario	Idealized Reaction Stoichiometry	Y_{SG} from stoichiometry	Y_{SG} from equilibrium
Base Case	$C_8H_{18} + 2H_2O + 3O_2 \overset{6H_2O}{\rightarrow} 11H_2 + 8CO$	1.12	1.08
Elevated O	$C_8H_{18} + 4O_2 \overset{8H_2O}{\rightarrow} 9H_2 + 8CO$	1.00	1.00
Pure POX	$C_8H_{18} + 3O_2 \rightarrow 7H_2 + 6CO + C_2H_4$	0.76	0.67
Elevated Steam	$C_8H_{18} + 2H_2O + 3O_2 \overset{22H_2O}{\rightarrow} 11H_2 + 8CO$	1.12	1.11
Pure SR	$C_8H_{18} + 8H_2O \overset{16H_2O}{\rightarrow} 17H_2 + 8CO$	1.47	0.33 (500°C) 0.70 (750°C)

Table 3.3: Idealized stoichiometry for each of the scenarios tested and the maximum theoretical synthesis gas yield obtainable based upon stoichiometric and adiabatic equilibrium calculations.

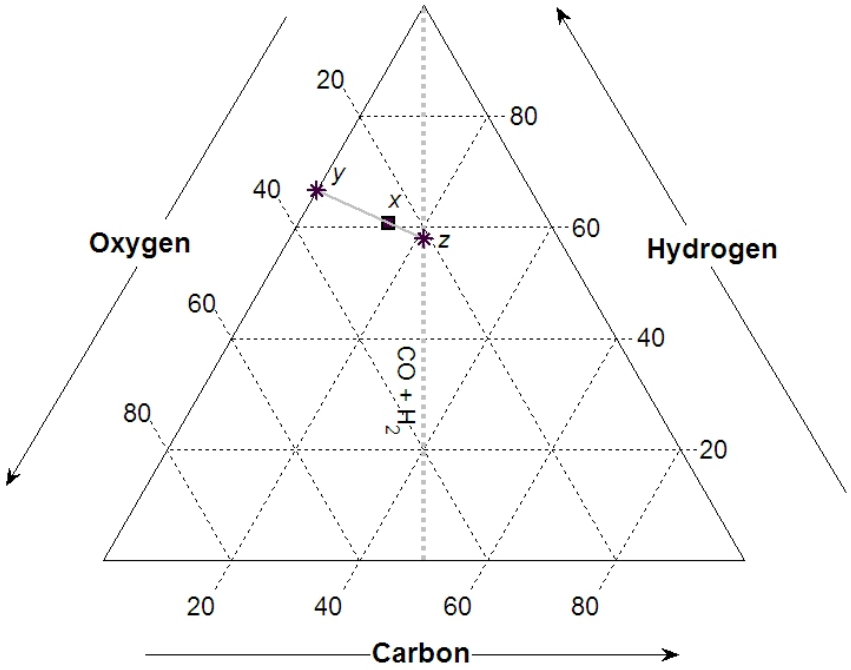

Figure 3.2: A C-H-O ternary diagram that shows an example of how to construct a line used to determine the stoichiometric constraint as defined by Reaction 3.3. The line is constructed by connecting the point of pure water (point y) with the Base Case inlet conditions (point x) and extending the line to intersect with the Syngas line. This intersection (point z) represents the ratio H_2/CO for the maximum obtainable Y_{SG}.

and quantify carbon deposited on catalysts during reaction. During this procedure, the oxidation of carbon deposits occurred along with the oxidation of metallic nickel sites. The TPO derivative peaks were isolated using a deconvolution method. Mass loss peaks occurring between temperatures of 500 and 700°C were attributed to carbon burn-off. Numerical integration of these peaks provided the mass of the carbon deposited during the reaction.

Powder XRD was performed on fresh and spent catalysts to identify solid phases present in the sample. The analysis was performed using a Rigaku 12-kW high-intensity rotary anode generator with a Cu K_α source. K_β radiation was filtered with a graphite-diffracted beam monochromator. XRD patterns were analyzed using Jade 9.0 software.

SEM provided visual confirmation of carbon morphologies and the presence of larger Ni particles where applicable. A FEI Nova Nanolab instrument was used to produce micrographs and determine elemental identification and composition calculation using energy-dispersive X-ray spectroscopy (EDS).

3.3 Results

3.3.1 Base Case

Figure 3.3 shows results for the ATR of isooctane over Ni/CZO with an inlet H_2O/C ratio of 1.0 and an O/C ratio of 0.75. Data is presented for representative sulfur-free and thiophene-exposed experiments. Experimetnal results were reproducible at all conditions, with variability in the Y_{SG} of within one to five percent. Figure 3.3a depicts the Y_{SG} during time-on-stream. The initial time on the x-axis is the point at which the catalyst was first exposed to the reactant stream. Figure 3.3b shows yields of carbon containing products (Y_{CO}, Y_{CO_2}, Y_{CH_4}, and $Y_{C_{2-4}}$) averaged over the final three data points of the experiment. The total carbon recovery is given

by the sum of these carbon yields. Carbon deposited on the catalyst itself represented a small fraction of the overall carbon and did not significantly influence the carbon balance. Figure 3.3c shows the temperature profiles through the reactor collected near the conclusion of each 500 minute experiment. The dashed lines show the relative locations of the front and bottom faces of the catalyst bed. Figure 3.3d shows the yields of the sulfur species H_2S, thiophene, and methylmercaptan throughout the duration of the experiment.

When sulfur was not present in the feed stream the activity of the catalyst was high and stable towards the production of synthesis gas. The carbon balance closed to within 5%, suggesting complete conversion of isooctane, almost entirely to CO and CO_2. The maximum bed temperature was 708°C with a bed exit temperature of 676°C. These reported temperatures are averaged between the repeated experiments. Variability in the bed temperature between repeated experiments was 1-5°C for most feed scenarios.

When thiophene was present as a contaminant both the isooctane conversion and the Y_{SG} were immediately lower than in the sulfur-free case. It is most notable that after the initial loss, the activity remained stable over the course of the experiment. In the presence of sulfur, the carbon balance was skewed noticeably away from CO, and more of the carbon exited the reactor as C_2-C_4 hydrocarbons, especially ethylene, propylene, and isobutylene. The temperature profile of the reactor showed a significantly higher catalyst bed temperature compared to the Base Case without sulfur. In this experiment the maximum bed temperature was 798°C and the temperature at the bottom-face of the catalyst bed was 778°C. Analysis of the sulfur products showed a breakthrough and complete recovery of sulfur within the first 100 minutes of the reaction. Thiophene was almost entirely converted to H_2S with a sulfur yield of less than 10% as methylmercaptan.

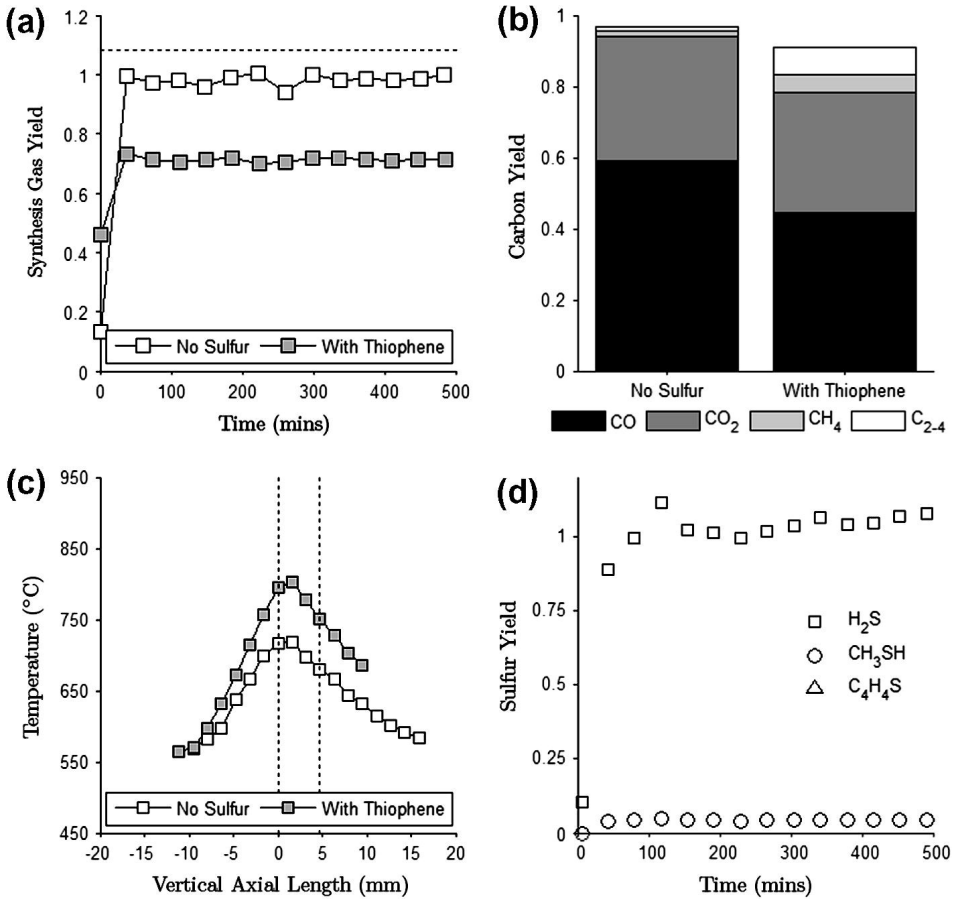

Figure 3.3: Results from the Base Case scenario. These panels show the effects of thiophene on Y_{SG} (a), the final yields of carbon species (b), and the steady-state axial reactor temperature profile (c). The dashed line in (a) shows the equilibrium predicted Y_{SG} (see Table 3.3). The dashed lines in panel (c) show the best approximation of the catalyst bed location, with negative axial length values denoting upstream temperatures and positive values for distance below the front face of the catalyst. Panel (d) shows the yield of major sulfur components in the product stream when thiophene is present in the Base Case. (Reactor conditions: $H_2O/C = 1$, $O/C = 0.75$, GHSV = 200 k h^{-1}, $T_{inlet} = 500°C$, $S_{in} = 0$ or 4.5 ppmv.)

3.3.2 Elevated O Scenario

The influence of thiophene on reforming behavior for feed conditions with an elevated oxygen concentration (O/C = 1, H_2O/C = 1) is shown in Figure 3.4. Without sulfur present the composition of carbon species was similar to the Base Case although there was a slightly lower Y_{SG} due to lower H_2 production. The temperature profile through the reactor showed significantly higher peak (822°C) and bed exit (807°C) temperatures.

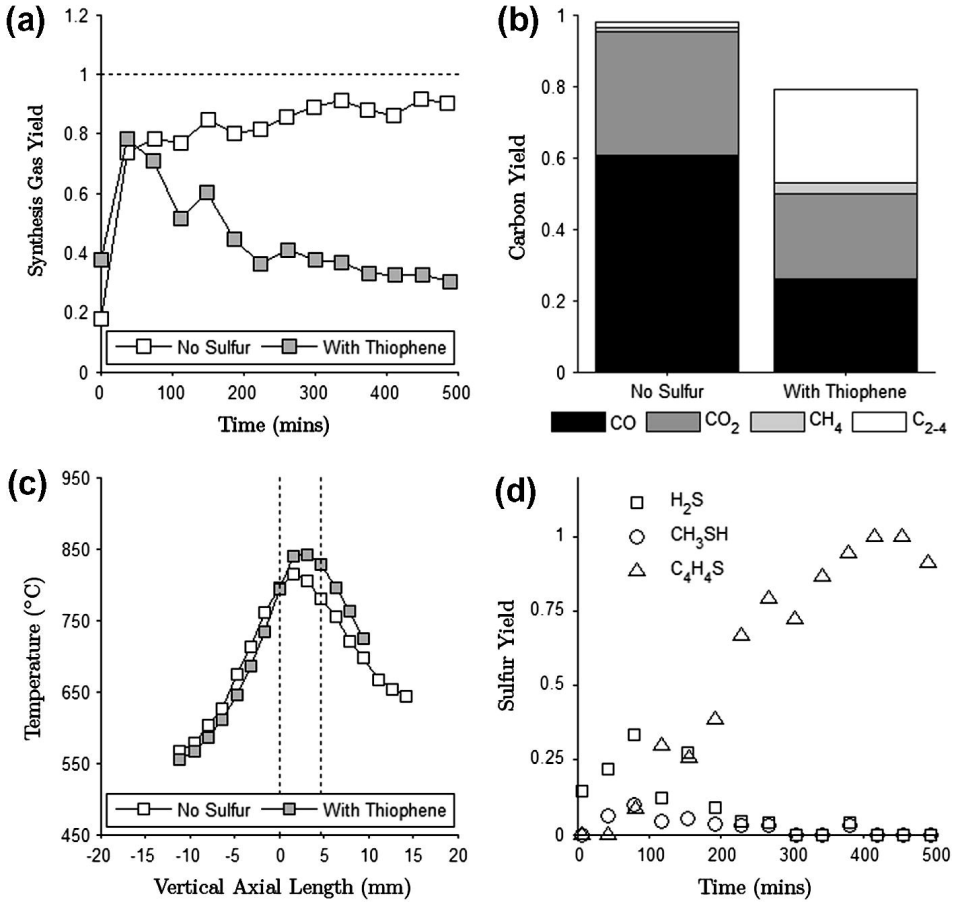

Figure 3.4: Results from the High O scenario. (a) Y_{SG} as a function of time-on-stream, (b) final yields of carbon species, (c) axial temperature profiles, and (d) yields of sulfur species. (Reactor conditions: H_2O/C = 1, O/C = 1, GHSV = 200 k h^{-1}, T_{inlet} = 500°C, S_{in} = 0 or 3.7 ppmv.)

The presence of thiophene had a significantly dissimilar effect upon reforming behavior in the Elevated O Case as compared to the Base Case. Initial selectivity

towards synthesis gas was similar to sulfur-free conditions, but decreased significantly over time in a trend suggesting continual deactivation. Carbon product yields in this case were almost evenly weighted between CO, CO_2, and the C_2-C_4 hydrocarbons, which were primarily olefins. The temperature profile shows that the reactor was again hotter in the presence of thiophene, although not as much as in the Base Case. The maximum bed temperature in this experiment was 842°C and the bed exit temperature was 829°C. As opposed to the Base Case, the thiophene was not completely converted to H_2S. An initial partial conversion to H_2S and methylmercaptan occurred, although eventually only thiophene was seen exiting the reactor.

3.3.3 Pure POX Scenario

Extending the influence of O concentration to pure POX conditions, with an O/C ratio of 0.75, results in the behavior shown in Figure 3.5. The activity was significantly lower than the Base Case or the Elevated O Case, even under sulfur-free conditions. However, the Y_{SG} was relatively stable over the course of this experiment, approximately 40%. The POX conditions resulted in a high CO/CO_2 ratio but a very significant level of olefins in the product stream. The sulfur-free maximum bed temperature was 790°C and the temperature at the bottom of the catalyst bed was 772°C.

With thiophene present in the isooctane feed, the consequences on Y_{SG} were similar to the Elevated O scenario, with an initial value similar to the sulfur-free experiment quickly showing a steady decline. Unlike the other feed conditions, there was no significant loss of isooctane conversion due to the presence of thiophene. However, a large portion of the carbon exited the reactor in the form of propylene and isobutylene. Reactor temperature measurements showed that the presence of thiophene coincided with a significant increase in reactor bed temperature with a peak temperature of 919°C and a temperature at the base of the catalyst bed of 901°C.

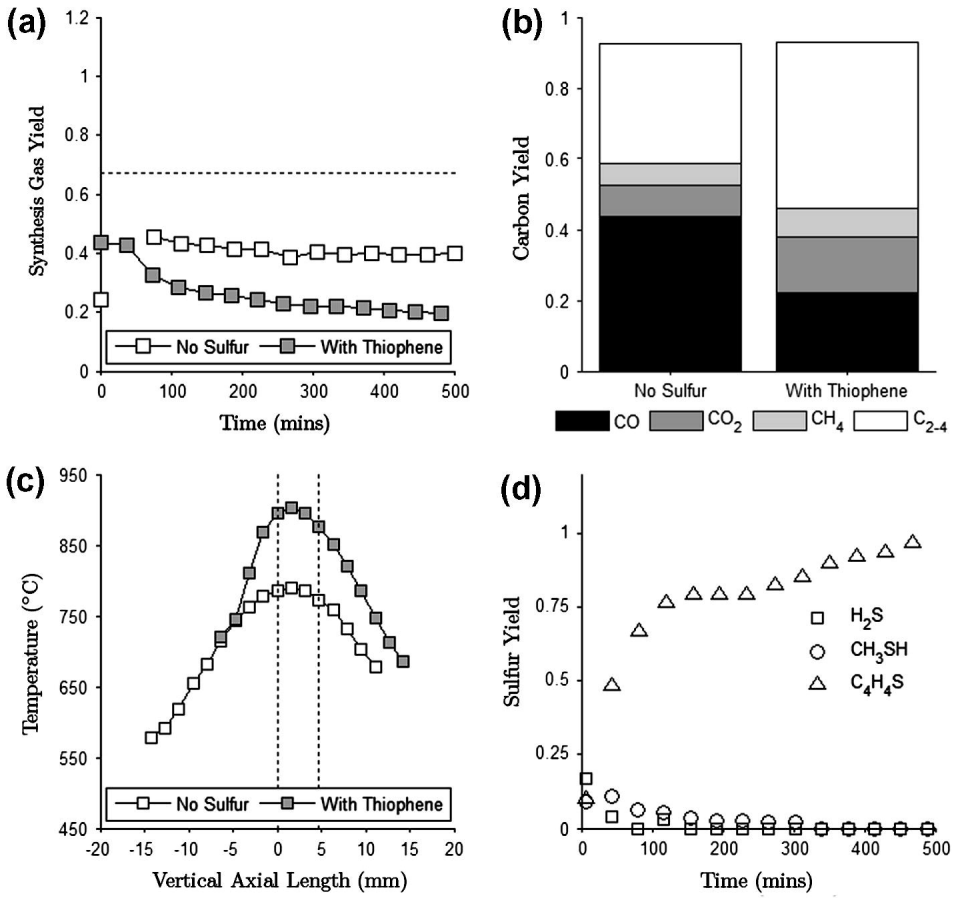

Figure 3.5: Results from the pure POX scenario. (a) Y_{SG} as a function of time-on-stream, (b) final yields of carbon species, (c) axial temperature profiles, and (d) yields of sulfur species. (Reactor conditions: $H_2O/C = 0$, $O/C = 0.75$, GHSV = 200 k h^{-1}, $T_{inlet} = 500°C$, $S_{in} = 0$ or 6.9 ppmv.)

Temperature measurements between the duplicated experiments showed significantly higher variability compared to other feed scenarios. The standard deviations of the experiments were 23°C and 36°C for the maximum bed and the bed-exit temperatures, respectively. Similar to the Elevated O scenario, thiophene was only initially converted to methylmercaptan and H_2S, and eventually unreacted thiophene was the only sulfur containing component in the product stream.

3.3.4 Elevated H_2O Scenario

Results of the Elevated H_2O feed concentration experiments (O/C =0.75, H_2O/C = 3) are shown in the panels of Figure 3.6, and most closely resemble the results of the Base Case. Under sulfur-free conditions the Y_{SG} was high and stable, about 90%. The carbon balance suggested only about a 90% conversion of isooctane. The reaction more strongly favored the production of CO_2 than the experiments with lower concentrations of H_2O. However, almost no methane was seen in the exit stream and C_2-C_4 hydrocarbons were not detected. The maximum temperature for this experiment was 685°C and the temperature at the lower face of the catalyst was 665°C.

With thiophene present the Y_{SG} under these conditions was diminished but stable, and a slightly higher selectivity to isobutylene and propylene occurred. The isooctane conversion was lower with sulfur present. As seen in prior scenarios, the temperature in the reactor was higher. The maximum temperature was 745°C and the bed-exit temperature was 734°C. Thiophene was completely converted to H_2S at steady-state.

3.3.5 Pure SR Scenario

Ni/CZO was not found to be significantly active under SR conditions (H_2O/C = 3) at the inlet temperature of 500°C (Figure 3.7). However, a small hydrogen yield was fairly stable over the course of the experiment, with less than 10% conversion

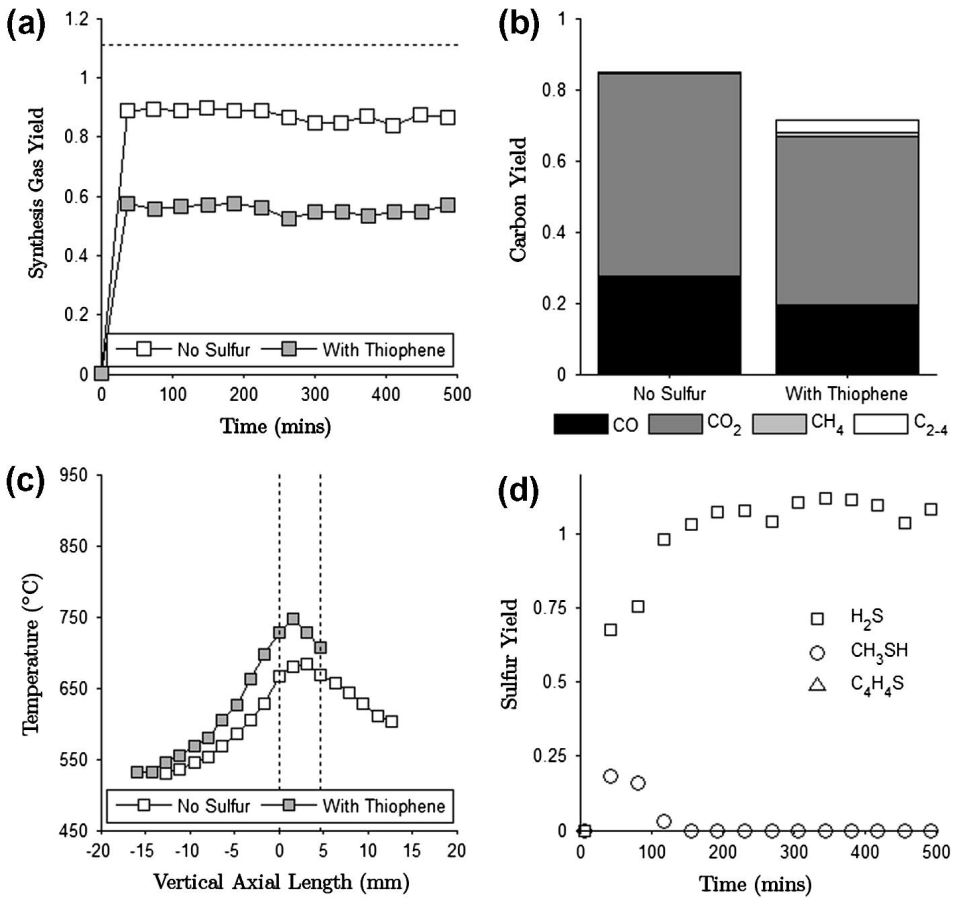

Figure 3.6: Results from the elevated H_2O scenario. (a) YSG as a function of time-on-stream, (b) final yields of carbon species, (c) axial temperature profiles, and (d) yields of sulfur species. (Reactor conditions: $H_2O/C = 3$, $O/C = 0.75$, GHSV = 200 k h^{-1}, $T_{inlet} = 500°C$, $S_{in} = 0$ or 2.7 ppmv.)

of isooctane to CO_2. However, when thiophene was added to the fuel, the minimal reforming activity vanished within the first 30 minutes of the experiment and thiophene emerged as the only sulfur product from the reactor. The sulfur-free SR activity was significantly higher for an inlet temperature of 750°C. But again, the presence of thiophene led to a complete loss of activity in the first 30 to 90 minutes of the experiment.

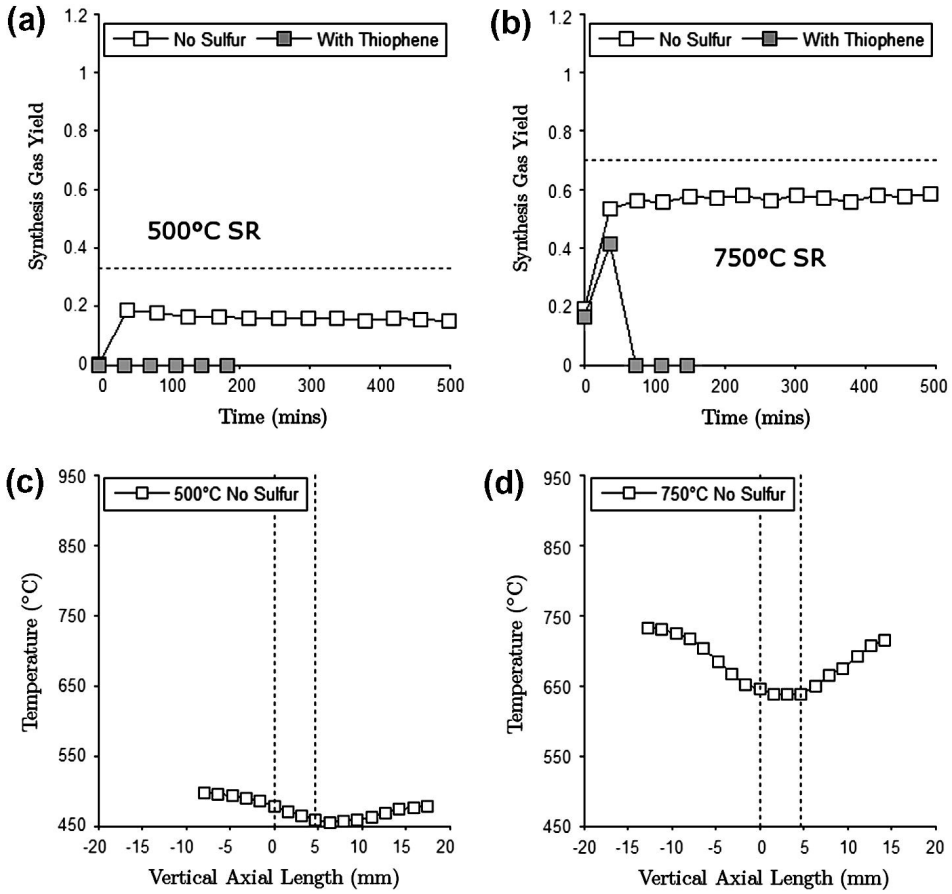

Figure 3.7: Results from the pure SR scenarios. (a) Effect of thiophene on Y_{SG} under SR at an inlet temperature of 500°C, (b) effect of thiophene on SR activity with an inlet temperature of 750°C, and (c and d) steady-state axial temperature profiles for SR at 500°C and 750°C, respectively. (Reactor conditions: $H_2O/C = 3$, $O/C = 0$, GHSV = 200 k h^{-1}, T_{inlet} = 500°C or 750°C, S_in = 0 or 2.7 ppmv.)

3.3.6 Carbon Deposition during Reforming

Average carbon deposition rates for the reforming experiments are shown in Table 3.4. TPO analysis showed that carbon deposition rates for all Elevated O and Elevated H_2O experiments, and the 500°C SR with thiophene experiment were below the detectable limits. Two broad mass gain peaks are due to the oxidation of metallic nickel and have peak temperatures of 400°C and 550°C. The mass loss peaks, attributed to carbon oxidation, occur over a range of temperatures between 500 and 700°C. The lowest quantifiable carbon deposition rate is approximately 0.3 mg C/(g catalyst∗hr) as small mass loss peaks cannot be distinguished from the mass gain peaks associated with Ni oxidation.

Scenario	No Sulfur	With Thiophene
Base Case	7.59 ± 7.38	0.82 ± 0.53
Elevated O	≤ 0.3	≤ 0.3
Pure POX	81.16	102.18 ± 54.35
Elevated Steam	≤ 0.3	≤ 0.3
Pure SR (500°C)	5.33 ± 3.31	≤ 0.3
Pure SR (750°C)	59.85	61.05

Table 3.4: Carbon deposition rates as determined by TPO, mg C/(g catalyst∗hr).

The carbon deposition rate data show that there was significantly more carbon deposited during the POX experiments than the ATR or SR experiments. Conclusions regarding the effect of thiophene upon carbon deposition were difficult to deduce based on the data of Table 3.4. The presence of thiophene under Base Case and 500°C SR conditions coincided with lower carbon present on post-reaction samples than after sulfur-free experiments. Conversely, carbon deposition was more pronounced under thiophene exposure during POX experiments and the 750°C SR conditions. However, these differences are all within the experimental error of the analysis and are not significant trends. Overall, the carbon deposition rates for all but the most extreme POX conditions were relatively low.

The morphologies of the carbon deposits were analyzed using SEM, and Figure 3.8

shows representative images. Figure 8a shows the structure of the reduced catalyst prior to reaction. All samples exposed to ATR conditions, regardless of exposure to thiophene, had structures like those seen in Figure 3.8b, which shows a micrograph of the post-reaction sample from the Base Case scenario with thiophene. Large particles of Ni with diameters between 50-500 nm were visible in all post-reaction samples, except those of SR experiments. Carbon deposits generally take the form of coating or encapsulating deposits or filament-like structures (*Chen et al.*, 2007). There were no carbon filaments visible in any ATR post-reaction samples, suggesting the formation of only coating-types of carbon.

Carbon filaments of various diameters were seen in POX post-reaction samples and SR samples not exposed to thiophene. Figure 3.8c shows the catalyst after reaction under POX conditions without sulfur. This image shows a region of high carbon filament concentration with diameters ranging between 40 and 150 nm. Ni particles as large as 500 nm are visible as well as regions of almost pure CZO. Figure 3.8d shows the effect of thiophene on carbon morphologies formed under POX conditions. The top portion shows a large carbon filament (∼350 nm), representative of the majority of carbon structures found throughout the sample. The bottom portion shows a particle of pure carbon presumably formed through the coalescence of large carbon filaments.

3.3.7 Surface Area Measurements

The physical surface area of the CZO support alone was 18.71 m^2/g and the surface area of the Ni/CZO catalyst was 13.94 m^2/g, as determined by single-point BET N_2 physisorption. H_2 chemisorption on reduced Ni/CZO was performed to determine the availability of active metal sites. The metal dispersion of the fresh catalyst was 1.69% and the active metal surface area was 1.12 m^2/g catalyst. Figure 3.9 shows chemisorption results from post-reaction analyses. In all experiments a sig-

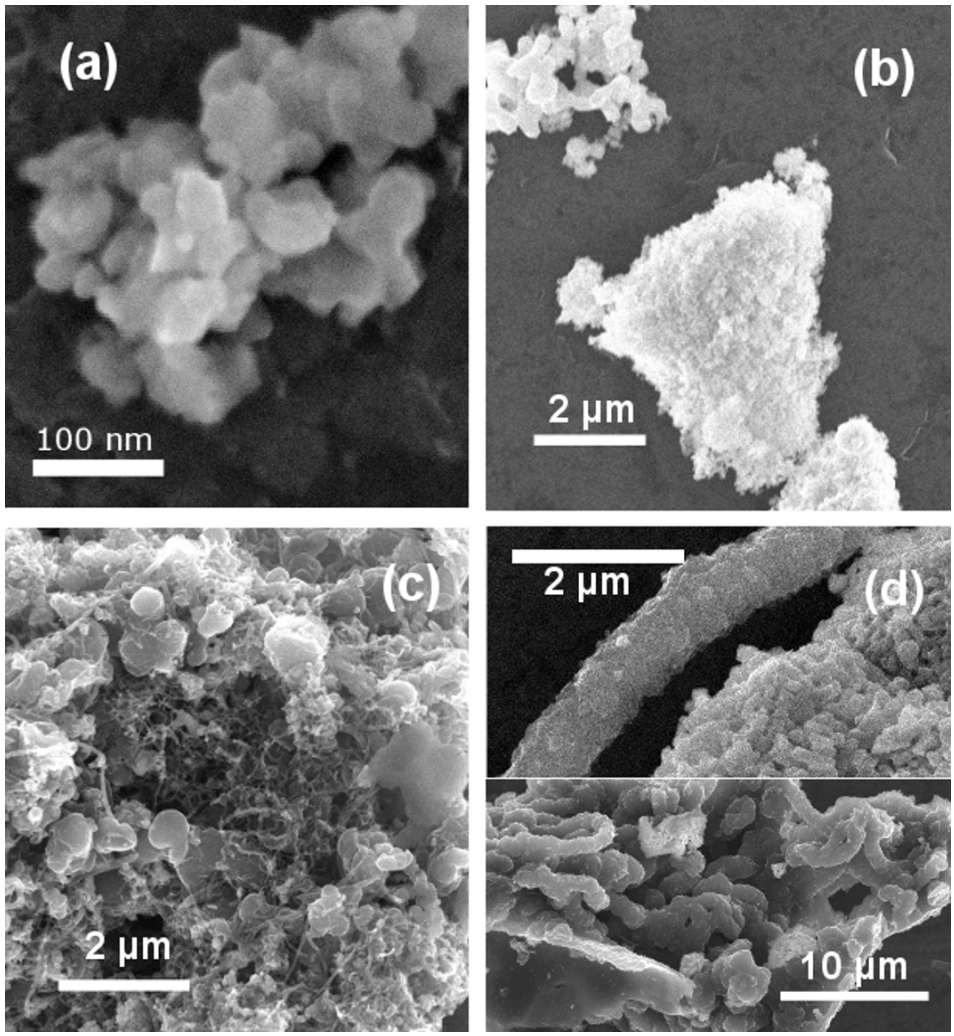

Figure 3.8: (a) SEM image of a fresh, reduced 10 wt.% Ni/CZO catalyst. (b) SEM image of a post-reaction catalyst following Base Case conditions with thiophene. (c) Carbon filament domains for a catalyst after POX without sulfur. (d) Carbon morphologies of POX sample exposed to thiophene.

nificant fraction of hydrogen uptake capacity was lost. The decrease in hydrogen chemisorption uptake was even more pronounced in cases with thiophene exposure. For example, at the Base Case conditions, the presence of thiophene resulted in 37% less hydrogen uptake. The most pronounced effect of thiophene was under POX conditions, where the hydrogen uptake was 81% lower when thiophene was present compared to sulfur-free POX runs. In the SR case, where the sulfur-free activity was low and the activity under thiophene exposure was undetectable, there was a 40% decrease in hydrogen uptake after reaction without sulfur and an 87% decrease after thiophene contaminated conditions.

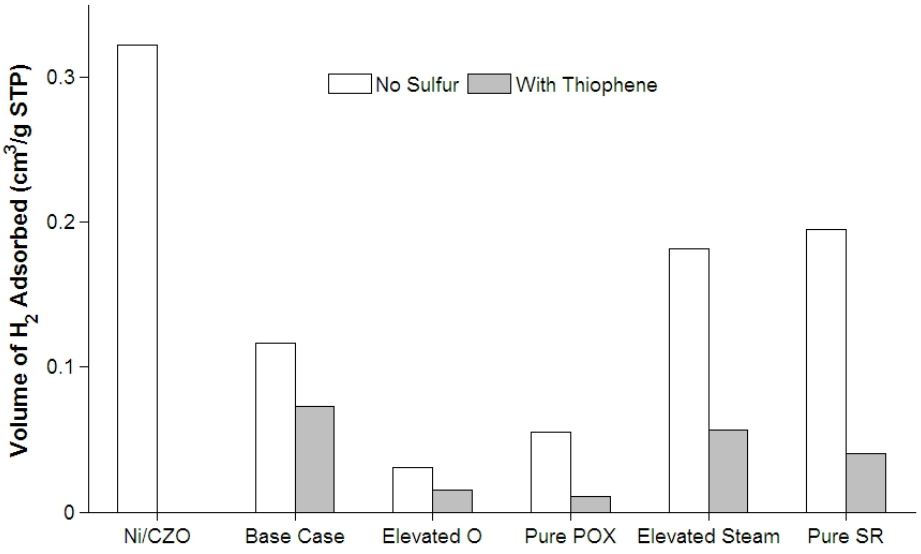

Figure 3.9: H_2 uptake of catalyst prior to reaction and after reaction at each condition.

3.3.8 XRD Measurements

Selected results from the powder XRD analysis are shown in Figure 3.10. The XRD pattern for fresh reduced Ni/CZO is shown at the bottom of both the left and right columns. The catalyst showed reflections for both CeO_2 and metallic Ni. The CeO_2 reflections were shifted slightly to higher 2θ values than reported in literature,

consistent with inclusion of Zr in the Ce lattice (*Kummerle and Heger*, 1999). Furthermore, in several of the samples there is a pronounced shoulder visible at the CeO_2 reflection in the region of 2θ = 26-32°. Recent work has shown that these discrepancies between CeO_2 and CZO reflections are due to separate phases of higher relative Ce and Zr concentrations (*Montini et al.*, 2009). The XRD patterns for post-reaction samples are also shown in Figure 3.10, with (right) and without (left) thiophene. In all cases the nickel reflections were stronger following reaction compared to the fresh sample. These reflections were weaker for thiophene-exposed samples than they were for sulfur-free samples. The high carbon deposition rates of the POX experiments coincided with the presence of graphitic reflections in post-reaction samples. NiO reflections were only visible for the post-ATR Elevated H_2O samples.

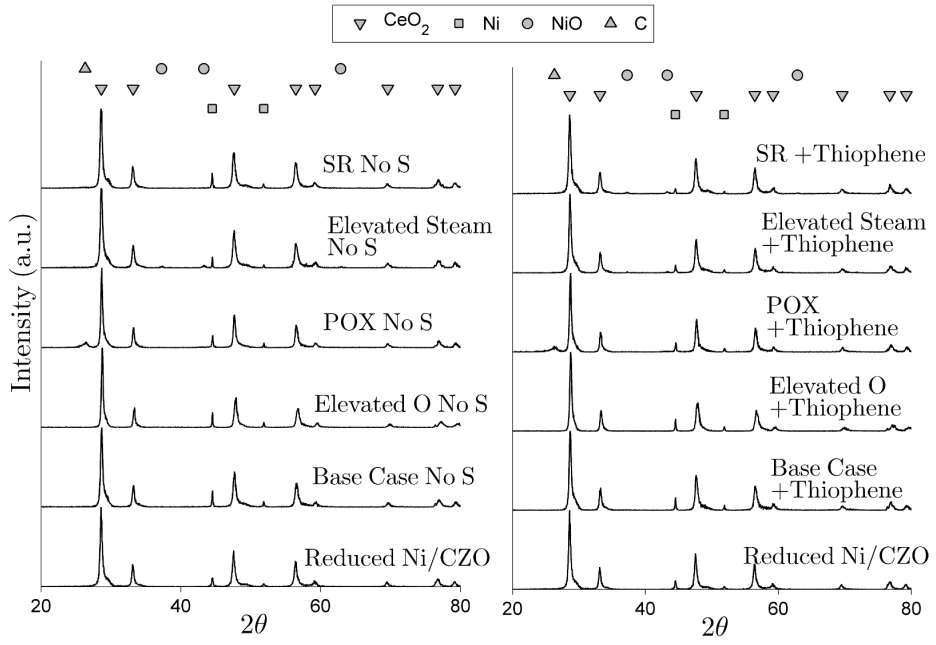

Figure 3.10: X-ray diffraction patterns of CZO support, reduced Ni/CZO catalyst and representative post-reaction samples. Reference reflections are shown above the figure (*Kummerle and Heger*, 1999; *Chen et al.*, 1990; *Rooksby*, 1943)

3.4 Discussion

The influence of sulfur on Ni-based catalysts has attracted interest due to the implications to the industrial steam reforming and hydrodesulfurization processes (*Rodriguez et al.*, 1999; *Rodriguez*, 2006). Studies on model systems have shown that the adsorption of sulfur on various crystallographic planes of Ni at high coverages provides the thermodynamic driving force for surface restructuring, leading to profound changes in activity and selectivity (*Owens et al.*, 1994; *Somorjai*, 1994). Charge transfer from metal d-orbitals to sulfur-localized orbitals during the formation of surface-bound sulfides leads to a decrease in the chemisorption activity of the metal (*Rodriguez et al.*, 1999). The extent of this interaction is dependent upon several factors including sulfur concentration, exposure time, and various catalyst properties.

However, a lack of a thorough description of the role of sulfur in an ATR reactor is primarily a consequence of the complex nature of this system. Visualize an autothermal reformer as consisting of three distinct regions with significantly different reactive environments. In the first region, radiative heat transfer from the catalyst provides the thermal energy for homogeneous decomposition and oxidative cracking of hydrocarbons, producing CO and lighter hydrocarbons. Molecular oxygen is then rapidly depleted in a shallow front-section of the catalyst bed through fast and exothermic catalytic partial oxidation and total oxidation reactions. The majority of the catalyst bed is dominated by slower reactions such as the highly endothermic reforming of light hydrocarbons and the establishment of thermodynamic equilibrium, presumably through a water-gas shift mechanism. This depiction has been developed explicitly for POX systems using spatially resolved techniques (*Horn et al.*, 2006) and has been implicitly extended to describe ATR systems (*Qi et al.*, 2005; *Laosiripojana and Assabumrungrat*, 2005; *Yoon et al.*, 2008; *Horn et al.*, 2007).

The experiments in this study have been performed in order to describe the behav-

ior of thiophene under various reforming conditions. Under all reaction conditions, the presence of thiophene resulted in an elevated reactor temperature and diminished selectivity towards synthesis gas production. Furthermore, more of the carbon exited the reactor in the form of hydrocarbons, especially propylene and isobutylene. These olefins are mostly formed through a homogeneous thermal cracking mechanism, and are consumed by catalytic steam reforming. Their increased concentration under thiophene exposure may therefore be attributed to diminished steam reforming activity. This diminished activity towards an endothermic mechanism is consistent with the elevated catalyst bed temperature.

In order to gain further insight into the reforming behavior, equilibrium calculations were performed using ASPEN. The equilibrium composition was calculated by minimizing the Gibbs free energy at the measured temperature and pressure at the end of the catalyst bed (unlike the preliminary results given in Table 3.2 that assumed adiabatic behavior). Thermodynamic calculations offer a convenient way to contextualize the results of reforming experiments. Table 3.5 shows how the measured outlet compositions of each experiment compared to equilibrium at the exit temperature and pressure. Thermodynamic equilibrium is effectively the reactor-exit composition at the infinite residence time and thus deviations from equilibrium compositions give a clue to the relative contributions of various reaction mechanisms, particularly which reactions were incomplete. For example, the positive deviation of CO_2 concentration for all experiments suggests that reactions leading to CO_2 formation, such as catalytic total oxidation, were quicker than reactions resulting in CO_2 depletion, such as reverse water-gas shift and dry reforming.

Under sulfur-free conditions, the data in Table 3.5 demonstrates that product compositions are very near thermodynamic equilibrium for all feed conditions except for SR, where low methane production resulted in a significant positive H_2 deviation. In all scenarios the presence of thiophene led to more positive, or less negative,

Scenario	H_2(%)	CO(%)	CO_2(%)	CH_4(%)	C_2H_4 to C_4H_8 (%)
Base Case	60.5%	24.1	14.4	0.97	0.02
no sulfur	(60.9%)	(23.9)	(13.1)	(2.03)	(9.94E-6)
Base Case	56.5	23.0	17.4	2.09	0.93
with thiophene	(61.9)	(28.0)	(9.9)	(0.14)	(2.81E-7)
Elevated O	55.7	27.7	15.1	0.88	0.66
no sulfur	(59.2)	(27.4)	(13.4)	(0.03)	(2.58E-8)
Elevated O	39.3	27.4	24.4	3.40	5.46
with thiophene	(59.0)	(27.9)	(13.0)	(0.02)	(1.5E-8)
Pure POX	38.4	40.8	7.55	5.90	7.40
no sulfur	(38.3)	(46.1)	(0.09)	(15.6)	(0.007)
Pure POX	17.7	30.2	14.4	14.0	22.8
with thiophene	(38.7)	(46.1)	(0.002)	(15.1)	(0.14)
Elevated H_2O	64.2	11.8	23.6	0.39	below detection
no sulfur	(66.8)	(11.1)	(21.9)	(0.26)	(1.44E-7)
Elevated H_2O	59.6	11.2	28.3	0.59	0.34
with thiophene	(66.4)	(13.1)	(20.5)	(0.05)	(1.33E-8)
Pure SR (500°C)	75.6	1.21	23.1	0.03	0.03
no sulfur	(54.8)	(2.14)	(22.0)	(21.1)	(0.008)
Pure SR (500°C)	N/A	N/A	N/A	N/A	N/A
with thiophene					
Pure SR (750°C)	70.6	8.28	15.3	2.63	3.16
no sulfur	(71.4)	(11.5)	(15.4)	(1.61)	(3.28E-8)
Pure SR (750°C)	N/A	N/A	N/A	N/A	N/A
with thiophene					

Table 3.5: Measured average product mole composition (no N_2, iC_8H_{18} or H_2O) compared to equilibrium predicted molar composition. Equilibrium values (given in parentheses) were calculated at the measured temperature of the bottom face of the catalyst.

equilibrium deviations for CO_2, CH_4, and C_2-C_4 hydrocarbons and more negative deviations for H_2 and CO. This suggests that the mechanisms for steam and CO_2 reforming are most adversely affected by the presence of thiophene, especially under conditions of high oxygen feed.

Stoichiometric considerations also aid in understanding the role of separate reaction mechanisms. Figure 3.1b shows the position of the reaction conditions on a ternary diagram. Considering the atomic balance of H, O, and C in the reactor provides a way to manage certain key system processes. For example, as demonstrated in this study, the Elevated H_2O and Elevated O feed scenarios both showed minimal carbon deposition and also produced less-negative deviations of CO from equilibrium in the presence of thiophene. These effects may be due to a greater availability of atomic oxygen, either from higher H_2O or O_2 feed. More molecular oxygen in the feed leads to a greater importance of oxidative cracking, a production route for CO. Similarly, the higher availability of atomic oxygen leads to an increased ability to remove carbon away from the catalyst surface.

An important distinction of this study lies in endeavors to identify and quantify sulfur products leaving the reformer. A common assumption has been that thiophene and other VSCs are completely converted to H_2S immediately in the catalyst bed. It is true that under all reforming conditions there is a large thermodynamic driving force towards H_2S formation. However, this study has demonstrated for the first time that the hydrodesulfurization (HDS) performance of nickel is related to its reforming activity. HDS of thiophene is a two-step process in which thiophene is first adsorbed and hydrogenated on a nickel site leading to a nickel-sulfide bond, and then the blocked site is 'cleaned' by chemisorbed hydrogen leading to the formation of H_2S (*Norskov et al.*, 1992).

It has been proposed that the rate of HDS is proportional to the number of vacant Ni sites, which is in turn dependent on both the strength of the Ni-S bonds and the

composition of the vapor phase (*Norskov et al.*, 1992). The thiophene conversion should therefore be closely linked to the availability of hydrogen to both hydrogenate chemisorbed thiophene and to 'clean' sulfided nickel sites. As seen in the results of Table 3.2 there is a correlation between the equilibrium partial pressure of hydrogen and tolerance to thiophene during reforming over nickel. In particular the Base Case and Elevated H_2O experimental conditions showed both sustained activity under the presence of thiophene and the highest equilibrium H_2 partial pressures.

Based on these observations, it is proposed that when the HDS process proceeded normally only the most active steam reforming sites were blocked by sulfur, and sulfur coverage quickly reached equilibrium. Consequently, a diminished yet stable steam reforming activity persisted over time, which resulted in elevated catalyst bed temperatures and a lower synthesis gas production as compared to sulfur-free operation. Conversely, when this low sulfur-coverage equilibrium was not reached, perhaps due to a lower availability of surface-bound hydrogen, site-blocking sulfides accumulated on the less active nickel sites and thereby caused a continuous drop in activity over time.

The relationship between equilibrium hydrogen composition and sulfur tolerance was developed in this study for five specific inlet conditions. Figure 3.11 helps provide a predictor of performance over a broader range of reforming conditions. The results of adiabatic Gibbs free energy minimization calculations are shown for H_2O/C from 0 to 10 and O/C from 0 to 2. Figure 3.11a shows a contour plot of adiabatic reactor temperatures on a C-H-O ternary diagram and Figure 3.11b shows the H_2 equilibrium mole fraction. Figure 3.11a demonstrates that as the O/C ratio increases above one the equilibrium temperature begins to increase into an undesired region, first in terms of catalyst sintering and second in terms of safe operation. Figure 3.11b provides an implicit prediction of the tolerance of the reforming system to thiophene exposure. Based upon the results of this study, equilibrium hydrogen compositions above 28%

(the two lighter shaded regions in Figure 3.11b) are associated with both high HDS activity and stable performance under thiophene exposure. It would be advantageous to construct a similar map describing carbon deposition behavior to further define optimal reformer inlet conditions.

Thiophene exposure also has an impact on the structure of the catalyst. Particle agglomeration is unfavorable as this decreases the availability of active surface sites. While it would be reasonable to assume that the elevated bed temperature experienced under thiophene exposure would have increased the rate of particle growth, the results from this study do not show a conclusive relationship between thiophene exposure and rates of sintering. Both SEM and chemisorption results suggested an increase in particle size after sulfur exposure, however XRD results implied the opposite as the presence of thiophene led to a decrease in the intensity of Ni reflections. The reconciliation of these observations is not possible at present due to the limitations of the characterization techniques used. For example, the hydrogen uptake during the chemisorption analysis may be underestimated due to the presence of surface-bound sulfur atoms, or a complex interaction with the support material. Visual confirmation of particle size using SEM suffers from large sampling error leading to a bias towards larger particles. XRD results also provide an incomplete description of the bulk structure due to several sources of uncertainty, including inner-particle grain boundaries, amorphous Ni regions, and low concentration or small particles of bulk nickel sulfide.

The identification of sulfur species on the post-reaction catalyst samples was attempted, with mixed results. XRD analysis did not show any sulfide or sulfate phases in any of the thiophene-exposed samples. The Sulfur 2p, 2s, and LMM auger transition regions were all scanned by X-Ray Photoelectron Spectroscopy (XPS) for all samples to identify sulfur species on the surface of the catalyst. However, positive sulfur identification was not achieved, possibly due to the low response of these tran-

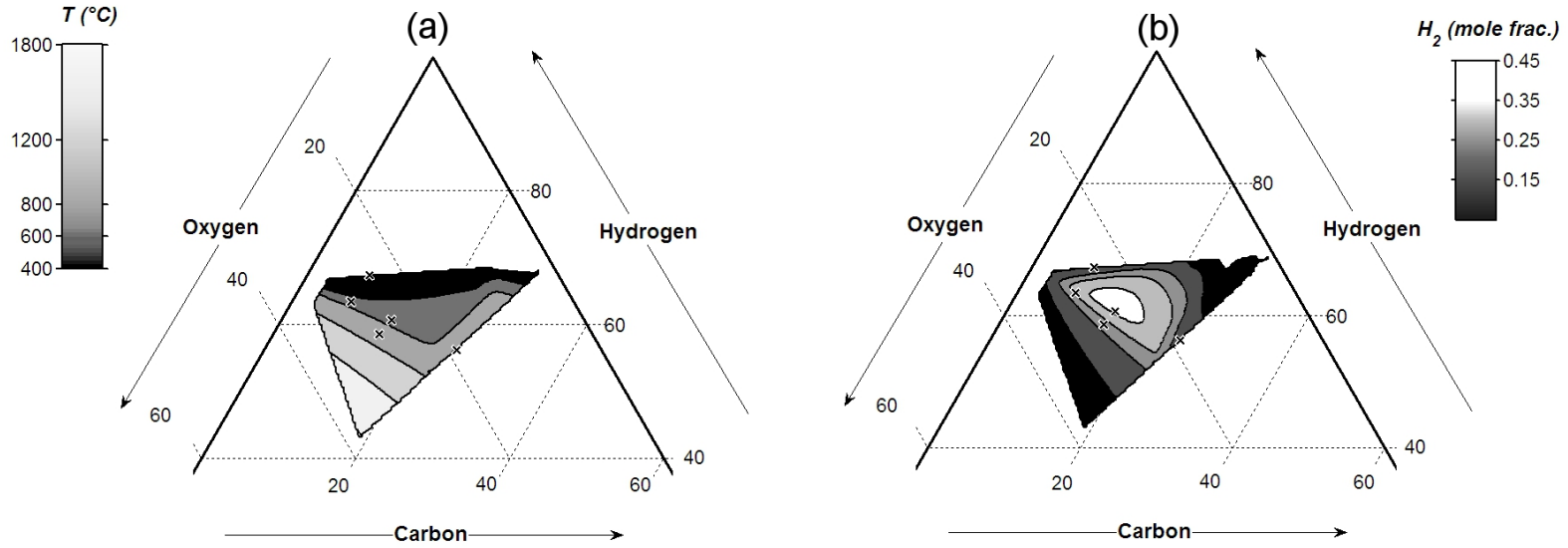

Figure 3.11: Contour plots of adiabatic exit temperature (a) and H_2 mole fraction (b) over the CHO space calculated by Gibbs free energy minimization of isooctane reforming. H_2O/C ratios ranged from 0 to 10 and O/C ratios ranged from 0 to 2. The equilibrium calculations were performed in ASPEN using isooctane, water and air as reactants with feed temperature of 500°C. In both diagrams, the × marks show the conditions considered in this study.

sitions. EDS measurements of SEM micrographs showed that sulfur was present on the Elevated Oxygen post-reaction sample. In this case, sulfur was only detected in regions of high Ni concentration, suggesting that sulfur was in close contact with nickel, supporting the theory that thiophene exposure at these conditions was responsible for loss of active nickel sites. The ability to identify and quantify sulfur from EDS measurements was inhibited by the presence of the overlapping zirconium peak.

An approximation can be made as to the sulfur content of post-reaction samples by analyzing the breakthrough curves of sulfur species through the reactor. Equation 3.13 gives the expression used to approximate the ratio of sulfur atoms to Ni atoms in the post-reaction sample. The results for each reforming scenario are given in Table 3.6. The values given in Table 3.6 likely suffer from a small systematic error due to unavoidable adsorptive losses of VSCs in the condenser. However, since this error is constant for all experiments, the trends shown in Table 3.6 are valid. As confirmed by SEM, the Elevated O scenario led to the most sulfur present on the catalyst. Such high adsorption levels of sulfur may have led to a loss in catalytic POX activity as well as SR activity, which may explain why the temperature rise due to the presence of thiophene was least severe under these conditions. The comparatively lower sulfur accumulation at pure POX conditions suggests that the excessive carbon deposition and sulfur blocking of steam reforming sites played a combined role in the poor selectivity towards synthesis gas production at these conditions.

Scenario	S/Ni ratio calculated from S breakthrough
Base Case with thiophene	0.01364
Elevated O with thiophene	0.04118
Pure POX with thiophene	0.02620
Elevated Steam with thiophene	0.01143
Pure SR with thiophene (500°C)	0.00489
Pure SR with thiophene (750°C)	N/A

Table 3.6: Atomic ratio of sulfur to nickel calculated from the breakthrough of sulfur-containing species from the reactor using Expression 3.13

$$S : Ni = \frac{F_{C_4H_4S,in} * MW_{Ni}}{cat.\ mass * cat.\ loading} \sum_t (1 - Y_{H_2S} - Y_{CH_3S} - Y_{C_4H_4S}) \cdot \Delta t \qquad (3.13)$$

Under the Base Case and Elevated H_2O ATR experiments, and the pure SR experiments, analysis of sulfur breakthrough showed less accumulation of sulfur compared to the Elevated O and pure POX feed conditions, despite their cooler bed temperatures. This observation is counterintuitive based on the inverse temperature dependence of the sticking coefficient. Low sulfur capacity under the two ATR conditions may be due to high HDS activity facilitated by high availability of H_2. The fact that the SR activity of the catalyst was completely diminished in the presence of thiophene suggests that the limited reforming activity under thiophene-free conditions was owed to the most highly active sites which were also the most susceptible to site blockage by adsorbed sulfur species.

3.5 Conclusions

In this study, the effects of thiophene on the isooctane reforming activity of $Ni/Ce_0.75Zr_0.25O_2$ catalysts were investigated under conditions representing five separate points on the C-H-O ternary diagram. These conditions ranged from pure steam reforming to pure POX, with the intermediary points representing typical autothermal reforming O/C and H_2O/C ratios.

It has been convincingly shown that adding even small amounts of thiophene to POX and ATR reformer feed streams can drastically alter the temperature profile in the reactor, leading to significant increases in catalyst bed temperatures. These temperature increases suggest that sulfur selectively blocks Ni sites responsible for endothermic steam reforming reactions, while having less effect on the sites responsible for exothermic partial or total oxidation reactions.

Remarkably, the reactivity of thiophene depends strongly on the reaction conditions. Depending upon the feed conditions, either the complete conversion of thiophene to H_2S or the breakthrough of unreacted thiophene was observed. The latter case coincided with a continuous decline in reforming activity over time-on-stream. In cases where conversion to H_2S occurred, an immediate but modest decrease in activity was observed, followed by stable reforming performance thereafter. Under pure steam reforming conditions at a 500°C feed temperature, thiophene exposure caused complete deactivation of the catalyst and thiophene emerged unconverted. This work has shown that certain reaction conditions can be selected that affect the availability of H_2 and thereby govern both the reforming activity and thiophene conversion to H_2S, thereby offering a promising strategy for maintaining stable reforming activity in the presence of sulfur compounds.

CHAPTER IV

Autothermal Reforming of Isooctane on Ni Catalysts: Particle Size and Sulfur Tolerance

This chapter describes the effect of Ni particle size on the autothermal reforming activity of sulfur-free and thiophene contaminated isooctane. Particle size was isolated as an experimental variable by preparing catalysts of variable Ni loading and equivalent pre-reaction active surface area. Without thiophene present, isooctane conversion and synthesis gas production increased as the Ni particle size increased. This suggests that small Ni particles either exhibited insufficient ensemble sizes or were handicapped by their higher propensity to form nickel oxides. However, smaller particles were less prone to deactivation during thiophene-exposed reforming. For Ni particles with mean diameters between 19 and 52 nm, as measured by Transmission Electron Micrsocopy (TEM), there was no significant difference in product yields or catalyst bed temperature under sulfur exposure. In fact, under these conditions the conversion of thiophene to H_2S was the only metric found to be correlated to particle size, thus suggesting different deactivation routes dependent upon particle size. These results demonstrate that smaller particles are less active to isooctane ATR but the elevated activity of larger particles is most vulnerable to sulfur poi-

soning. This would seem to controvert the null hypothesis that certain low coordinated sites would be most active to reforming chemistry and most prone to sulfur poisoning. In addition to the increased insight into the complex autothermal reforming chemistry, this work also provides the practical heuristic that maintaining catalytic activity under sulfur exposure will not be achieved by engineering materials with successively smaller particles.

4.1 Introduction

The influence of metal particle size on catalyst performance has been demonstrated for a broad range of systems. In most cases, the goal of catalyst synthesis is to formulate a material with a stable particle size distribution skewed towards smaller particles (*Somorjai*, 1994). Thereby, a maximum number of the metal atoms are available at the surface to facilitate the desired reactions. Additionally, it has been shown that the surface sites of smaller particles often behave different chemically than those of larger particles. This is because smaller particles will have an increased relative concentration of higher energy crystallographic planes. These surfaces feature a lower average coordination number and altered electronic structure (*Henry*, 2007; *van Hardeveld and Hartog*, 1969), causing them to bind adsorbing molecules more strongly.

The discussion of particle size is applied here to the field of hydrogen production from hydrocarbon fuels via the ATR reaction using Ni-based catalysts. Ideally, this system couples oxidation and steam reforming pathways to produce an equilibrium-limited mixture of H_2, CO, CO_2, and CH_4 (*Flytzani-Stephanop. and Voecks*, 1983; *Lutz et al.*, 2004; *Docter and Lamm*, 1999). This reformate has several applications, including power generation via solid oxide fuel cells and automotive emissions control (*Schwank and Tadd*, 2010; *Krumpelt et al.*, 2002). In practice, the long-term stability

and activity of noble and non-noble based catalysts are limited both by side reactions that produce problematic carbon deposits and also by poisoning of active sites by sulfur containing compounds often found within hydrocarbon fuels (*Shekhawat et al.*, 2006; *Rodriguez and Hrbek*, 1999; *Sehested*, 2006).

Investigations into particle size effects have been applied previously to certain aspects of this chemistry. For example, it is well demonstrated that steam reforming reactions preferentially occur at low coordinated kink and step sites and proceed at much slower rates on highly coordinated terrace sites (*Rostrup-Nielsen*, 1984; *Beebe et al.*, 1987; *Larsen and Chorkendorff*, 1999; *Abild-Pedersen et al.*, 2005; *Wei and Iglesia*, 2004; *Jones et al.*, 2008). In addition, there is evidence that carbon deposition rates are dependent on metallic particle size (*Bengaard et al.*, 2002; *Rostrup-Nielsen*, 1975; *Borowiecki*, 1982). However, it is often difficult to control particle size independently of other variables such as metal loading and total number of surface sites. For that reason, many previous studies have failed to separate or account for these confounding effects.

This study attempts to isolate the effect of particle size on the sulfur tolerance of a Ni-based catalyst during the autothermal reforming of isooctane. The weight loading of Ni in the catalyst was varied to control particle size. The novelty of this study is that the total number of active surface sites was removed as a variable in the discussion of particle size effects. This was done by selectively pre-treating catalysts to create a series of samples with different loadings and particle sizes but equivalent surface areas. This series of catalysts was then tested for ATR of sulfur-free and thiophene-doped isooctane. The goal of this study was both to further the understanding of particle size effects in a complex reaction environment and to guide the development of Ni catalysts more tolerant to sulfur exposure in such environments.

4.2 Experimental

4.2.1 Catalyst Preparation and Hydrothermal Treatment

The goal of the catalyst preparation phase of this study was to obtain catalysts which had the same measured surface area but different metal loadings. An increase in loading without a corresponding increase in the number of surface sites necessarily implies the presence of larger Ni particles, assuming that the particles are of roughly the same shape and interact similarly with the support.

The catalysts used for this study were Ni supported on zirconium-modified ceria. The support, $Ce_{0.75}Zr_{0.25}O_2$, was prepared by coprecipitation of the precursor salts $Ce(NO_3)_3{\cdot}6H_2O$ and $ZrOCl_2{\cdot}8H_2O$ using a 4M solution of NH_4OH. The precipitate was then recovered by filtration and dried at 100°C. The dried material was ground and sieved to yield material in the range of 250 and 420 microns. The support was then calcined in air at 900°C for 2 hours. Ni was impregnated onto the support using the incipient wetness technique with the metal precursor $Ni(NO_3)_2{\cdot}6H_2O$ dissolved in deionized water. The four different loadings of Ni that were prepared for this reactor study were 0.7 wt%, 3 wt%, 5 wt% and 10 wt%. Additional loadings were prepared and used to describe the effect of the sintering process described below. Following impregnation, each catalyst was calcined in air at 500°C for 30 minutes in order to decompose the nickel precursor.

Prior studies have shown that catalysts with increasing Ni particle size may be obtained by simply increasing the Ni loading (*Chen et al.*, 2007; *Gould et al.*, 2007, 2008), but this has the simultaneous effect of also increasing the active surface area (S_A). In order to compensate for this effect, increasingly severe hydrothermal treatments were performed to sinter the catalysts as Ni loading was increased, such that the final catalysts had an equal Ni S_A. The sintering behavior of Ni-based materials have been characterized previously by *Sehested* (2003, 2006); *Sehested et al.* (2004) under sim-

ulated steam reforming conditions. They reported simple power law rate expressions and Arrhenius-type temperature dependence, results that guided the hydrothermal treatment procedures in this study.

A 1/2" o.d. 316-SS vessel was used for the hydrothermal treatment. Prior to treatment the catalysts were reduced at 600°C for 30 minutes under flow of 5% H_2 in N_2. Following reduction the catalyst was heated or cooled to the desired treatment temperature in pure N_2. The catalyst was then exposed to flow consisting of a 10:1 ratio of steam to H_2 in N_2. A needle valve was used to set the pressure in the vessel to approximately 20 psig. Various aging times and temperatures were considered for the 3, 5 and 10% Ni loading catalysts in order to characterize the influence of aging conditions on the active surface area of the catalyst. In order to match the surface area of the 0.7% Ni catalyst, the 3% Ni sample was treated at 700°C for 4 hours, the 5% sample at 800°C for 5 hours, and the 10% sample at 830°C for 8 hours. The catalysts used for reactor studies are summarized in Table 4.1. The synthesis and subsequent aging procedures were repeated to create a second batch of identical catalysts to determine experimental variability.

4.2.2 Autothermal Reforming Behavior

The above described catalysts with approximately identical Ni surface areas and Ni different loadings were tested for their autothermal reforming activity with sulfur-free and thiophene-doped isooctane. Previously published results have shown that ATR operating conditions have a significant impact on the effects of thiophene (*Mayne et al.*, 2010). For example, at higher steam-to-carbon ratios, low carbon deposition and relatively high H_2 production lead to catalyst stability in the presence of thiophene. In order to neglect carbon deposition and focus solely on the relationship between Ni particle size and sulfur tolerance, this study used a steam-to-carbon ratio of three, an oxygen-to-carbon ratio of 0.75, and a gas-hourly-space-velocity of 200,000

Ni Loading (wt%)	Initial S_A (m^2/g)	Age Time (hours)	Age Temp. (°C)	Final S_A (m^2/g)	H_2 Chemi. d_p (nm)	XRD Ni [111] d_p (nm)	XRD Ni [200] d_p (nm)	STEM/EDS d_p (nm)
0.7	0.29	N/A	N/A	0.29	16.1	N/A	N/A	N/A
3	0.94	4	700	0.33	62.1	20.1	N/A	18.9
5	1.15	5	800	0.26	137.7	38.7	22.7	26.7
10	1.49	8	830	0.33	204.5	62.4	45.1	51.3

Table 4.1: Summary of the hydrothermal reduction treatment used to obtain the pre-reaction catalysts, the pretreatment H_2 Chemisorption S_A, the post-treatment S_A, and the particle size estimations from H_2 Chemisorption, XRD and STEM/EDS. All catalysts were calcined at 500°C in Air prior to any aging treatment.

hr^{-1}. In order to increase the observed effect of thiophene, a higher concentration was used compared to the previously reported study. A thiophene contamination of approximately 230 ppmw was used in the isooctane feed, which equates to 88 ppmw S in the isooctane or 7.9 ppmv S in the reactor feed stream.

Flow controllers (MKS, Bronkhorst) fed reactants into sulfur-resistant lines which were heated to 180°C to vaporize the feed. The reactor consisted of a 1/2" quartz tube inside a furnace (Thermolyne). A thermocouple within a closed-ended 1/8" quartz tube was used to measure in situ temperature profiles along the center-axis of the reactor tube. Online gas chromatography (Varian CP-3800 GC) was used to analyze the products of the reactor. A single-stage condenser was used to prevent water from flooding the GC columns. Two TCDs and a PFPD identify and quantify species within the product stream (H_2, N_2, CO, CO_2, CH_4, ethane, ethylene, propane, propylene, isobutylene, H_2S, CH_3S, and thiophene) separated on packed columns in the GC. This GC analysis provided compositional data at an interval of approximately 35 minutes.

Prior to reaction, 500 mg of catalyst were reduced in situ at 600°C for 30 min using a 5% H2 in N_2 feed. Previous studies have demonstrated that high-temperature light-off causes excessive sintering (*Gould et al.*, 2007). Therefore, a lower light-off temperature was used for these experiments. Following reduction, the catalysts were cooled in N_2 to 300°C. The reaction was started by switching the feed to the reactant flow (1.82 mmole/min iC_8H_{18} containing 230 ppmw thiophene, 45.2 mmole/min H_2O, and 25.8 mmole/min Air), and then ramping the furnace to the desired 'feed' temperature of 500°C. For each experiment the reaction was carried out for 400 minutes time-on-stream. A temperature profile of the catalyst bed was taken in the last 30 minutes of the reaction. Following the experiment, the catalysts were cooled under N_2-flow, and prior to any post-reaction analysis, the spent catalysts were finely-ground to reduce sampling errors.

The activity of the catalyst was described in terms of the yields of H_2, CO, and the combined performance metric, Y_{SG}, which are defined in Table 4.2. Additionally, the distribution of carbon between CO, CO_2, methane, and paraffins, olefins (C_2H_4-C_4H_8) and the distribution of sulfur (when thiophene was present) between H_2S, CH_3S and thiophene were determined. The yields of these various species are calculated by first calculating the flowrates of each species, F_x, in the product. This was achieved by treating N_2 as non-reactive species and as internal standard in the interpretation of the GC data. Since previous work has demonstrated a carbon balance closure within 5% (*Mayne et al.*, 2010), summing the yields of carbon-containing species provided a good estimate of isooctane conversion.

Performance Metric	Symbol	Formula
Synthesis Gas Yield	Y_{SG}	$\frac{\left(F_{H_2}+F_{CO}\right)_{,out}}{17*F_{C_8H_{18},in}}$
H_2 Yield	Y_{H_2}	$\frac{F_{H_2,out}}{9*F_{C_8H_{18},in}}$
CO Yield	Y_{CO}	$\frac{F_{CO,out}}{8*F_{C_8H_{18},in}}$
CO_2 Yield	Y_{CO_2}	$\frac{F_{CO_2,out}}{8*F_{C_8H_{18},in}}$
CH_4 Yield	Y_{CH_4}	$\frac{F_{CH_4,out}}{8*F_{C_8H_{18},in}}$
Yield of other hydrocarbons	Y_{2-4}	$\frac{\left(2*F_{C_2H_4}+2*F_{C_2H_6}+3*F_{C_3H_6}+3*F_{C_3H_8}+4*F_{C_4H_8}\right)_{,out}}{8*F_{C_8H_{18},in}}$
Conversion of isooctane	X	$Y_{CO}+Y_{CO_2}+Y_{CH_4}+Y_{2-4}$
H_2S Yield	Y_{H_2S}	$\frac{F_{H_2S,out}}{F_{C_4H_4S,in}}$
CH_3S Yield	Y_{CH_3S}	$\frac{F_{CH_3S,out}}{F_{C_4H_4S,in}}$
Thiophene Yield	$Y_{C_4H_4S}$	$1-X_{C_4H_4S}\approx\frac{F_{C_4H_4S,out}}{max\left(F_{C_4H_4S,out}\right)}$

Table 4.2: Metrics of isooctane ATR performance and their corresponding formulae.

4.2.3 Catalyst Characterization

Various techniques were employed to characterize fresh and spent catalysts in this study. H_2 chemisorption was used to verify equivalent active surface areas (S_A) for the pre-reaction catalysts. TEM and XRD provided direct measurement of particle sizes. Diffuse Reflectance Infrared Fourier Transformed Spectroscopy (DRIFTS) analysis of CO chemisorption experiments was performed in order to investigate the nature of the CO-Ni bonding for each of the catalysts. Temperature Programmed Reduction (TPR), H_2 Chemisorption, and XRD analyses of the post-reaction materials were performed to provide further insight into the Ni dispersion.

H_2 chemisorption experiments were performed using a Micromeritics ASAP 2020 instrument. Prior to analysis, the sample was first evacuated at 100°C, and then reduced under pure H_2 flow at 450°C for 2 hours. Next, the sample was evacuated for 2 hours at 450°C before being cooled to 35°C for analysis. The H_2 uptake was measured at pure H_2 doses ranging from 50 to 300 mmHg, at 50 mmHg intervals. The analysis was repeated in order to correct for physically adsorbed H_2 not stoichiometrically bound to the surface Ni atoms. Accordingly, the uptake reported in this study is the difference between the two measurements extrapolated to 0 mmHg. The H_2 uptake was used to calculate an apparent S_A by assuming a 1:2 H_2-to-Ni molecular ratio and a cross-sectional atomic surface area of 0.0649 nm^2 for Ni (*Micromeritics*, 2005). The S_A was used to approximate a surface-averaged particle diameter, d_p, assuming a spherical particle shape.

Scanning Transmission Electron Microscopy (STEM) coupled with EDS elemental mapping was used to measure the Ni particle size distribution in the catalyst materials and calculate a population-averaged d_p. Powder samples were prepared for analysis by dispersing approximately 10 mg of powder in 5 mL ethanol followed by ultrasonicating the solution for one hour to break up agglomerates. The particles were deposited on copper grid supported carbon films by submersion in the suspension.

A JOEL 2010F analytical electron microscope was used for STEM and EDS studies. The instrument uses a zirconated tungsten [100] thermal field tip filament and was operated at 200 kV under a pressure of 1.5e-7 Torr. A probe size of 0.5 nm was used for STEM. A Gatan retractable CCD camera was used to collect HAADF STEM images. Elemental maps for Ni, Ce, and Zr were obtained via an EDAX r-TEM detector with EDAX acquisition software. The effects of image drift were corrected using a drift correction mode. To measure metal particle sizes, the area of each clearly resolved particle in the Ni EDS Map was measured and converted to the diameter of a circle having the same area.

XRD provided a volume-averaged d_p measurement. Phase identification and crystallite size measurements for fresh catalyst samples via XRD were accomplished with a Rigaku Rotating Anode X-Ray Diffractometer. The instrument utilizes a Rigaku 12 kW rotary anode generator with a Cu K_α source. K_β x-ray wavelengths were filtered using a graphite diffracted beam monochromator.

Diffraction patterns were obtained over a 2θ range of 20-80°, at a scan speed of 2°/min and a 0.01°resolution. These patterns showed lines for both fluorite-structured CeO_2 and metallic Ni phases. A shift in CeO_2 lines to slightly higher 2θ values is consistent with the inclusion of some Zr in the fluorite lattice, however asymmetric features, such as tailing on the higher 2θ side of CeO_2 lines, suggests inhomogeneity in the Ce-Zr composition (*Montini et al.*, 2009; *Kummerle and Heger*, 1999). No Ni lines could be resolved for the 0.7 wt% loaded catalyst.

Ni particle sizes were calculated using the Scherrer Equation (4.1). The broadening, β, of each profile line of maximum intensity, I_p, was calculated according to an integral broadening expression (Equation 4.2).

$$d_p = \frac{2d_{hkl}tan\,(\theta)}{\beta} \tag{4.1}$$

$$\beta = \frac{1}{I_p}\int I\,(2\theta)\,d2\theta \tag{4.2}$$

For these calculations slower scans (0.1°/min) were obtained in the 2θ regions of Ni [111] (43-46°) and Ni [200] (50.4-53.4°) at a 0.2°resolution to obtain clean experimental profiles of these relatively weak lines. The contribution of broadening due to instrumental aberrations to the overall broadening of these lines was measured by repeating the procedure for a LaB_6 powder standard in the 2θ regions of [200] and [210] lines, corresponding to Ni [111] and [200] lines, respectively. All patterns were smoothed and stripped of their background using JADE software routines. Pure profile broadening values used in particle size calculations were obtained by decomposition of experimental profiles using the Fourier expansion procedure of *Rafaja* (2000).

Infrared signatures of characteristic surface-adsorbate geometries can provide a glimpse into the bonding character of heterogeneous catalysts. Toward this goal, CO was used as a probe adsorbate to gain insight into the surface structure of the prepared catalysts. DRIFTS experiments were conducted in a Bruker Optics Tensor 27 Infrared Spectrometer equipped with a Harrick Scientific Praying Mantis IR Accessory and High Temperature Reaction Vessel. Catalyst samples were diluted with potassium bromide (KBr, Spectrophotometric Grade, Sigma-Aldrich) to 35.0 wt%, finely ground, and loaded into the DRIFTS sample cell. The sample was oxidized in air at 600°C for 30 minutes to clean the sample of any carbonaceous species. Argon gas (UHP, 99.99% Ar) was used to purge the DRIFTS accessory of oxygen; the sample temperature was held at 600°C during the Argon purge. A mixture of 50% H_2 in Ar was used to reduce the sample for 60 minutes at 600°C. After reduction, UHP Argon was used to

purge the DRIFTS accessory and remove chemisorbed H_2 for a period of 60 minutes at 400°C. The sample was then cooled to 20°C under UHP Argon gas flow. Once the sample temperature reached 20°C, a background FTIR spectrum was collected; all FTIR measurements were acquired using 2048 scans at 2 cm^{-1} of resolution. Carbon monoxide (10% CO in Argon) was introduced to the DRIFTS accessory for 20 minutes and allowed to adsorb to the reduced Ni-metal. UHP Argon was used to flush the DRIFTS accessory of gas-phase and weakly-bound CO for 30 minutes, at which point the spectrum of interest was acquired.

TPR was used in this study to approximate the mass-averaged oxidation state of spent catalyst materials. TPO and TPR of fresh catalysts together provided a description of the ease to which metallic Ni may be oxidized or that NiO may be reduced. Both TPR and TPO analyses were performed using Thermogravimetric Analysis (TGA) using a TA TGA Q500 instrument. Samples were heated from 120 to 800°C under flow of 60 mL/min N_2 and 40 mL/min air for TPO and 90 mL/min N_2 and 10 mL/min H_2 for TPR.

In order to corroborate the oxidation state approximations obtained from TPR analysis, the spent catalysts were also characterized using XPS. The spent catalysts were finely ground and pressed into indium foil. The samples were then evacuated at less than 5e-7 torr for 8 hours prior to XPS analysis. Spectra were then collected at approximately 1e-9 torr background pressure. A Kratos Axis Ultra XPS was used with a monochromated Al X-Ray source. Ni 2p core scans were collected in the binding energy range between 880 and 846 eV with a 200 ms dwell time at each 0.1 eV interval. The detector was set to analyze electrons at a Pass Energy of 40 eV. Forty scans of the region were collected in order to decrease the signal-to-noise ratio. Binding energy calibration was achieved by setting the adventitious carbon 1s peak position to 284 eV. Data processing, including background removal and peak fitting, was performed using the CasaXPS software package.

4.3 Results and Discussion

Previously reported results have demonstrated that stable activity during the ATR of thiophene-containing isooctane can be achieved under operating conditions where thiophene was converted to H_2S, though the activity was lower compared to sulfur-free experiments (*Mayne et al.*, 2010). Experimental evidence suggested that steam reforming reaction pathways were most negatively impacted by the presence of thiophene, and it was theorized that the Ni sites most active to steam reforming were also most vulnerable to deactivation by thiophene or H_2S. This hypothesis suggests the possibility of achieving more sulfur-tolerant Ni catalysts by altering the balance between more highly active, but sulfur sensitive Ni sites, and less active, but more sulfur tolerant sites.

Investigations of model systems have demonstrated that key elementary steps of the steam reforming reaction and the poisoning of sites by sulfur are both structure-sensitive events; they proceed at dramatically different rates depending on the identity and chemical environment of the active site employed (*Ahmed et al.*, 1990). Based upon these findings, it should be expected that Ni dispersion and reforming activity should be closely linked. In general, higher dispersion will result in a higher fraction of exposed low-coordinated sites due to the balance between surface energy minimization and geometric limitations. Indeed, it has been demonstrated that the turn-over-frequency (chemical rate per active site) of methane steam reforming increases for higher dispersions for several transition metal catalysts, including Ni (*Jones et al.*, 2008).

Investigation of structure effects for catalytic ATR in the presence of sulfur is challenging due to the coinciding structure sensitivities of steam reforming and sulfur poisoning, and also due to thermal and chemical variability in the catalyst bed, characteristic of ATR. Stated simply, the goal of this research was to determine if low-coordinated active Ni sites more highly concentrated on small Ni particles were

most responsible for deactivation under thiophene exposure.

4.3.1 Catalyst Preparation and Hydrothermal Reduction Treatments

The most readily applied method for controlling particle size and therefore the proportion of different active sites (lower versus higher average coordination number) is altering the metal loading. The simultaneous effect on the total number of active sites is shown in Figure 4.1. For a series of Ni/CZO catalysts prepared with varied Ni loading, following a brief calcination at 500°C for 30 minutes, it was found that the active Ni S_A, as measured by H_2 chemisorption, increased linearly with the logarithm of the loading over the range of 0.5 to 10%. This linear trend holds with a correlation coefficient of 0.989, and solicits an underlying physical explanation which would predict such a simple relationship.

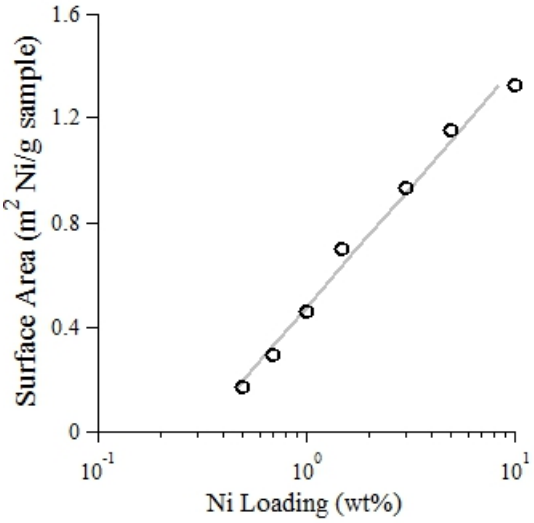

Figure 4.1: Active Ni surface area of prepared (non-aged) Ni/CZO catalysts measured by H_2 Chemisorption as a function of the nominal nickel loading (log scale). A linear trend line is displayed; this fits the data with a correlation coefficient of 0.989. Prepared Ni/CZO catalysts were calcined at 500°C for 30 minutes as part of the preparation procedure.

By way of example, a simple model might assume a fixed number of Ni nucleation sites on the blank support followed by cubo-octahedral growth of a fixed number

of Ni particles for increasing weight loadings. Such geometry has been described previously for fcc metals (*Agostini et al.*, 2009). This model expectedly predicts the decay in dispersion as Ni is added and an increasing number of atoms are present in the inner-core or bulk of the particles. However, this predicted rate of decrease in the dispersion is less than that which would describe the results shown in Figure 4.1. Assuming a fixed number of Ni particles, the Ni S_A would vary as a function of the Ni loading to the 2/3 power; which does not match the observations. The relationship shown in Figure 4.1 therefore requires a more complex model which would account for increased inaccessibility of Ni atoms due to both bulk particle growth and also another unknown process.

It is not known what contribution the CZO support has to the observed relationship between Ni loading and active surface area and no other supports were considered in this study. Also, no other adsorbate probes, such as atomic S or CO, were used to quantify S_A. Such investigations could possibly lead to the development of a more comprehensive description of metal particle growth. In this study it was sufficient to recognize and make use of the simple relationship shown in Figure 4.1.

As the goal of this work was to investigate only the effect of increasing Ni particle size, it was necessary to prepare a series of catalysts of different Ni loadings, resulting in different particle sizes, while attempting to correct for the corresponding increase in the total number of surface sites. This was achieved by selectively sintering catalysts to an increasing degree as the Ni loading was increased. As the catalyst is sintered the average particle size will increase and the S_A will decrease. This approach simultaneously accentuates the effect of interest, particle size, while correcting for S_A.

A point of clarity should be made at this point regarding this experimental approach. The process of sintering is an ongoing process at ATR conditions. There exists for each Ni loading a most thermodynamically stable structure of Ni (corre-

sponding to the value S_A^∞, described below). Over the course of the ATR experiments it is expected that the SA should decrease with time-on-stream, as it trends towards S_A^∞. Therefore, the goal of the catalyst preparation was to prepare catalysts with the same initial S_A, as a first-order attempt at correcting for the fact that increasing the Ni particle size by increasing the Ni loading also increases the number of Ni surface sites.

Sintering of Ni-based catalysts is a fairly well-explored issue as particle growth is a common problem affecting long-term catalytic performance. For example, *Sehested* (2003, 2006); *Sehested et al.* (2004) have made significant progress in describing the growth of Ni particles under simulated steam reforming environments. That work suggested a power-law expression for the decay of S_A with respect to time, as in Expression (4.3), and an Arrhenius-type dependence upon temperature, as given in Expression (4.4). In these expressions, k refers to the rate constant for the decay of S_A, n is an integer generally greater than 7, S_A^∞ is the infinite temperature S_A, and E_A is the activation barrier for the process.

$$-\frac{dS_A}{dt} = kS_A^n \tag{4.3}$$

$$S_A = S_A^\infty e^{E_A/RT} \tag{4.4}$$

Conditions similar to *Sehested* (2003, 2006); *Sehested et al.* (2004) were used in order to control the decrease in S_A, except that the pressures used here were less than 2 bar, as opposed to the 30 bar used by *Sehested* (2003, 2006); *Sehested et al.* (2004). Figure 4.2 shows the effect of the hydrothermal reduction process on the S_A of selected Ni/CZO catalysts. As expected, increased temperature and exposure time both decreased the Ni S_A. These results did not follow the Expressions (4.3) and (4.4), perhaps due to either an insufficient data set or the lower system pressure

used. However, the influences of treatment time and temperature were sufficiently predictable to develop a protocol for preparing catalysts with equal S_A.

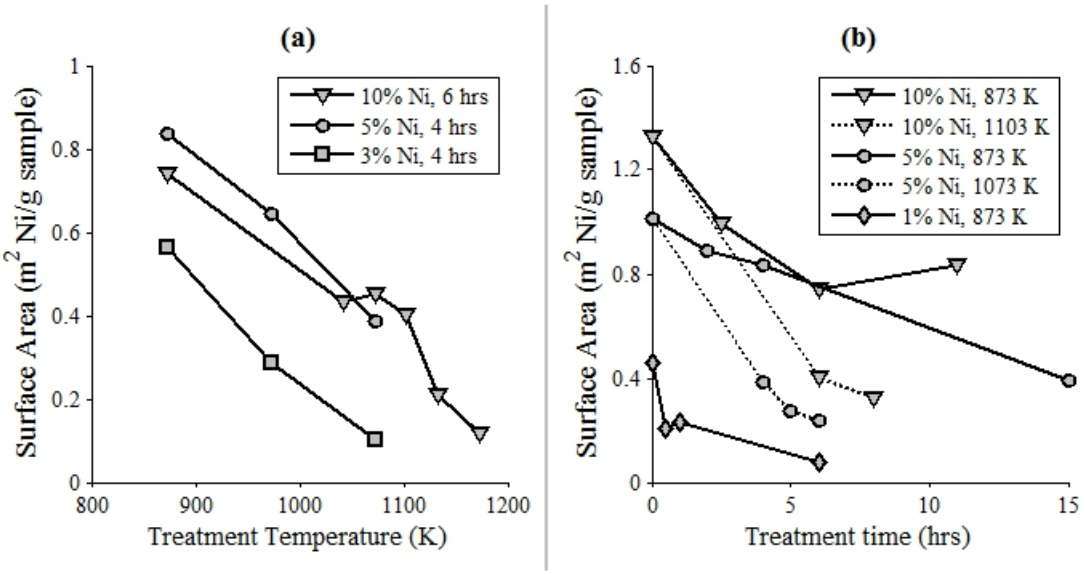

Figure 4.2: The effect of hydrothermal aging treatment temperature (a) and duration (b) on the measured S_A for various prepared Ni/CZO catalysts.

As shown in Table 4.1, the 3 wt%, 5 wt% and 10 wt% loaded samples were treated at the tabulated temperatures and durations in order to have Ni S_A similart to that of untreated 0.7 wt% Ni on CZO. This resulted in four different catalysts with 0.3 $\pm$0.03 m^2 Ni S_A per gram of catalyst prior to reaction. As these catalysts were loaded with different amounts of Ni, they were therefore expected to exhibit a range of particle sizes. Furthermore, if the range of particle sizes was sufficient, it would also be expected that the catalysts should display disparate chemical behaviors owing to a varied contribution of higher versus lower coordinated Ni surface sites. Additional characterization of the pre-reaction catalysts was performed in order to demonstrate that the four catalysts indeed presented an assortment of particle sizes and a measureable difference in surface chemical behavior.

4.3.2 Characterization of Pre-Reaction Catalysts

XRD and STEM were employed to independently verify that the catalysts prepared for this study exhibited significantly different particle sizes while yielding comparable active surface area measurements. Chemisorption provides an estimation of the surface-averaged mean particle diameter (d_p). However, the accuracy of this estimate is limited by Ni surfaces not accessible to probe adsorbate molecules likely due to physical interaction of the metal with the support. Therefore, it should be expected that chemisorption would over-estimate particle sizes by under-estimating active surface area.

XRD of the pre-reaction materials yielded a volume-averaged d_p. Table 4.1 shows the results of the application of the Scherrer Equation (4.1) to the Ni [111] and [200] reflections. Both Ni reflections for the 0.7% Ni/CZO sample and the [200] reflection for the 3% Ni/CZO sample could not be resolved sufficiently to calculate crystal sizes at those indices. Based upon the [111] reflection calculations, there is a clear trend in particle size across the pre-reaction catalysts such that 10% Ni/CZO > 5% Ni/CZO > 3% Ni/CZO. This trend follows the d_p trend approximated from H_2 Chemisorption, with XRD measurements consistently about 30% smaller than values approximated by chemisorption. If it is assumed that this trend holds for 0.7% Ni/CZO (Figure 4.3), an estimate of the Ni particle size for that sample would be 4.9 nm.

Based on the XRD results, the calculated d_p in the [200] direction is smaller than that calculated in the [111] direction, which is surprising given that the [111] plane has a lower surface energy (*Vitos et al.*, 1998). A simple Wulff type construction predicts a direct relationship between surface energy of a surface and the width of a particle in that direction (*Chorkendorff and Niemantsverdriet*, 2003). Possible causes for this discrepancy may be alternative surface energetics due to the chemical environment of the hydrothermal reduction process or a facet-specific interaction with the CZO support.

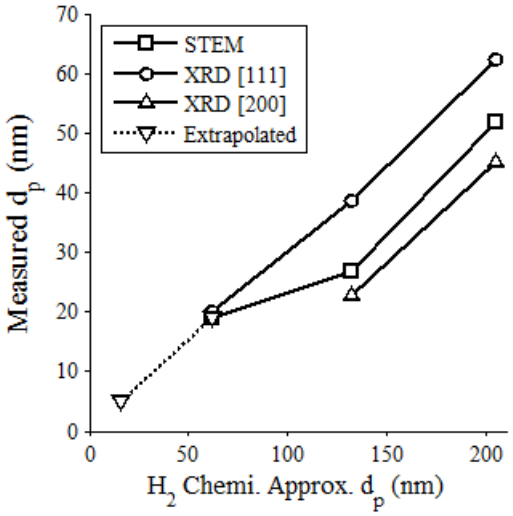

Figure 4.3: Ni particle size measurements obtained from STEM and XRD shown as a function of the H_2 chemisorption approximated particle size. The 0.7% Ni/CZO value is extrapolated based upon the linear relationship between the H_2 Chemisorption estimation and the XRD measured average particle size in the [111] lattice direction.

Ni mapping of STEM images performed with EDS measurements provides a method to both visualize the structure of Ni particles and to calculate a number-averaged d_p. Figure 4.4 shows representative STEM images for the pre-reaction catalysts. The Ni particles in the 0.7% sample were too small to be counted accurately for this analysis, but distinct Ni particles are visible among the CZO support material for the other samples. Particle size distributions are shown in Figure 4.5 fit to log-normal population distributions. This analysis confirmed the trend in particle size of the pre-reaction samples as measured using XRD and approximated from H_2 Chemisorption. The mean Ni particle diameter and the standard deviation of the mean particle diameter are both highest for the 10% Ni/CZO pre-reaction catalyst, followed by 5% Ni/CZO, and then 3% Ni/CZO. The d_p values calculated from the [111] and [200] reflections are within 1.1 standard deviations of the STEM measured particle sizes.

The combination of the S_A and d_p measurements confirm the production of a

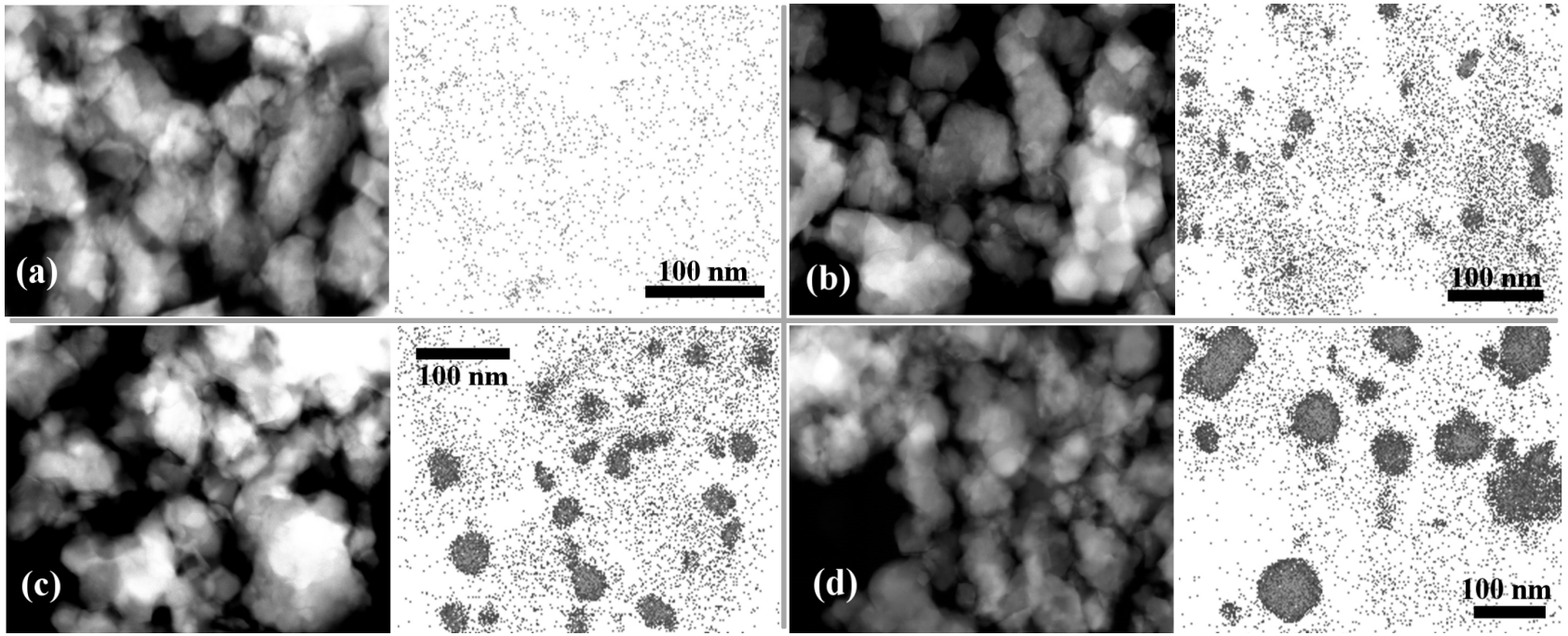

Figure 4.4: Representative STEM images (left) and corresponding EDS Ni maps (right) for the pre-reaction samples 0.7% Ni/CZO (a), 3% Ni/CZO (b), 5% Ni/CZO (c), and 10% Ni/CZO (d). Scale bars in all images correspond to 100 nm.

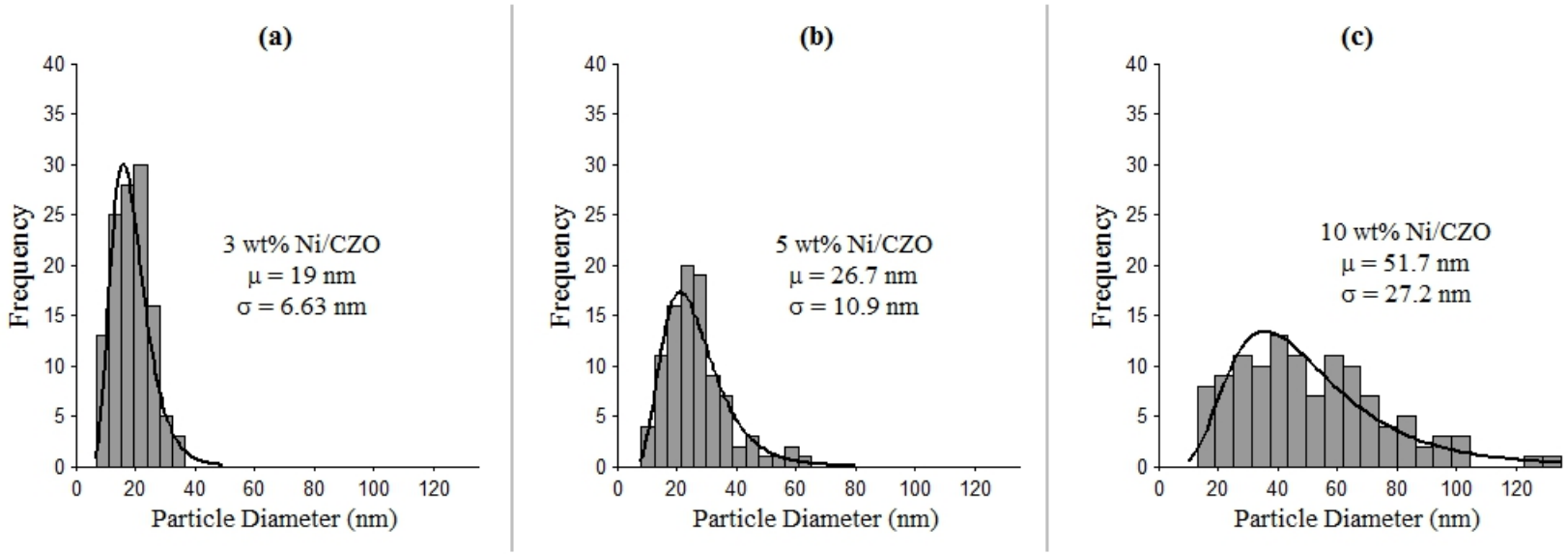

Figure 4.5: Particle Size Distributions obtained from STEM/EDS analysis for the pre-reaction catalysts: 3 wt% Ni/CZO (a), 5% Ni/CZO (b) and 10% Ni/CZO (c). Solid lines show the best-fit of log-normal distributions to each of the histogram data sets.

series of catalysts with equivalent pre-reaction surface areas and different particle sizes. In order to determine that the range in particle sizes were sufficient to affect a measurable change in reactivity, the pre-reaction catalysts were analyzed for their reducibility and oxidizability as well as the nature of their bonding with a chemisorbed probe molecule, CO.

Figure 4.6 shows the TPR features of the fully oxidized pre-reaction catalysts and the TPO features of the fully reduced pre-reaction catalysts. All four catalysts displayed two reduction features, a low-temperature feature between 270 and 290°C and a high-temperature feature between 630 and 640°C. The location and constant area of the high-temperature feature is consistent with the surface reduction of the CZO support (*Tadd*, 2006). The area of the low-temperature feature increases for higher Ni loadings and is assigned to reduction of NiO species. Results show that there is no significant difference between loadings in the reducibility of the pre-reaction materials once oxidized.

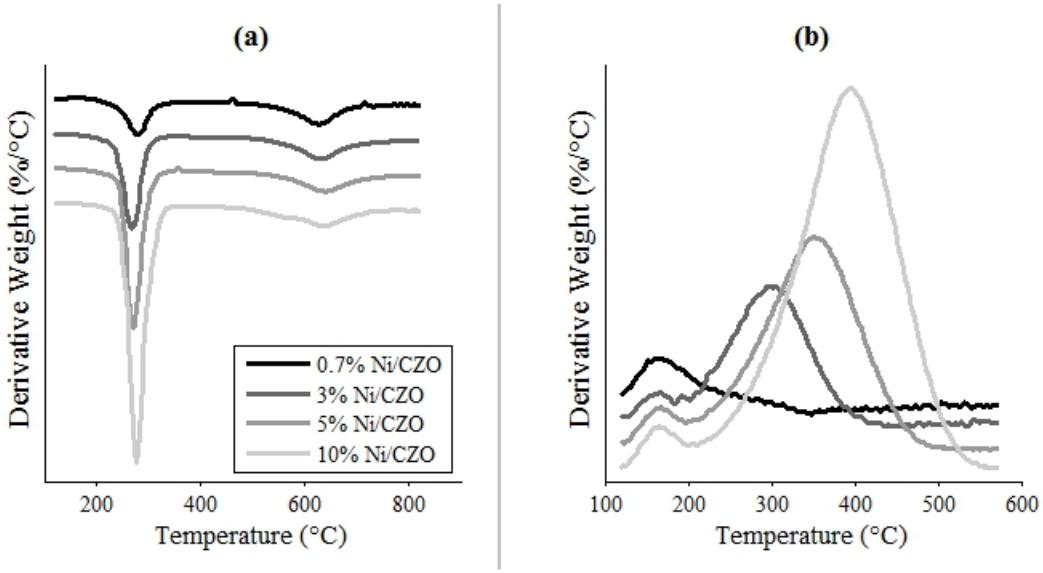

Figure 4.6: TPR (a) and TPO (b) dTGA curves of the pre-reaction catalysts.

However, the TPO curves shown in Figure 4.6b suggest a significant difference between loadings in the oxidation behavior of the reduced pre-reaction material. In

all samples there is a low temperature oxidation feature at 164°C. Additionally, there is a broader oxidation feature seen in the 3, 5, and 10% Ni/CZO samples, not seen in the 0.7% sample. This feature increases in temperature with loading, from 300°C for 3% Ni/CZO to 400°C for 10% Ni/CZO.

Due to a lack of work performed in the identification of TPO features, it is not clear from this data what specific oxidation process each feature represents. However, it is clear that 0.7% Ni/CZO is significantly easier to oxidize than the other catalysts exhibiting only the low-temperature feature. Additionally, the trend in the high-temperature feature suggests that 10% Ni/CZO is the least readily oxidized, followed by 5% Ni/CZO, and then 3% Ni/CZO.

Infrared probing of CO bound to pre-reaction catalysts provided a more direct view of the chemical nature of the Ni surface. These experiments also offered some evidence as to the relative contribution of higher index and more reactive versus low-index and less reactive Ni sites. The results, which are displayed in Figure 4.7, demonstrate measureable differences in the CO bonding character of the four pre-reaction catalysts.

All DRIFT spectra of Ni-loaded samples revealed absorption in frequency regions consistent with CO adsorbed to Ni-metal (*Blyholder*, 1964; *Hadjiivanov et al.*, 1999; *Agnelli et al.*, 1998; *Pereira and Martin*, 1993; *Resini et al.*, 2009; *Hadjiivanov et al.*, 1998; *Blackmond and Ko*, 1985; *Campuzano and Greenler*, 1979; *Bertolini and Tardy*, 1981). A summary of the observed CO-stretching frequencies is presented in Table 4.3. As each catalyst has a similar active metal surface area, as measured by H_2 Chemisorption, and the same mass fraction dilution in KBr, it is possible to interpret the relative quantity of individual CO-adsorption sites via the observed IR band intensity at a specific wavenumber. IR absorption bands near 2039 cm^{-1} were observed for each sample and are generally assigned to linear carbonyl species bound to a single nickel site (*Blyholder*, 1964; *Hadjiivanov et al.*, 1999; *Agnelli et al.*, 1998;

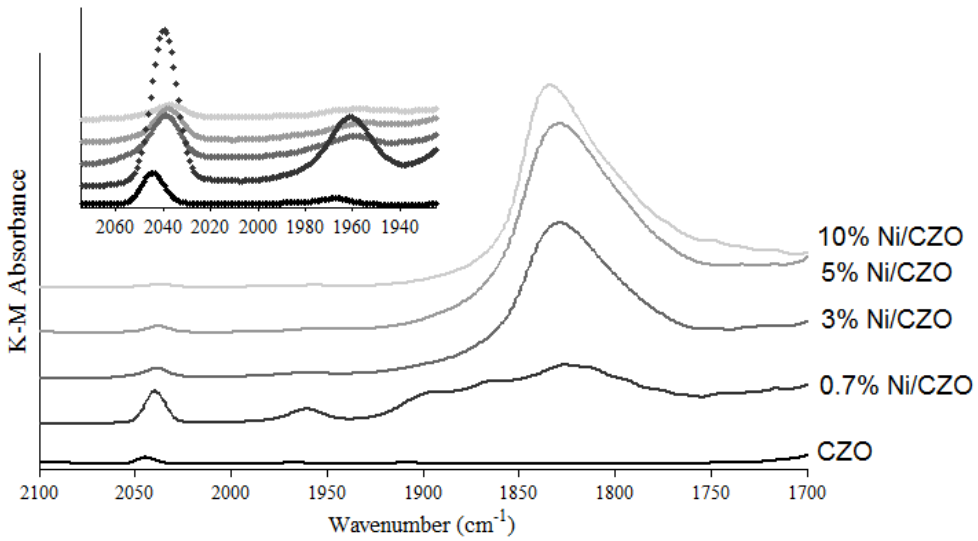

Figure 4.7: DRIFT Spectra from the adsorption of CO on the various pre-reaction Ni/CZO catalysts and the CZO support. Inset is zoomed in on the higher wavenumber region of the scan.

Pereira and Martin, 1993). Some authors have suggested that this absorption band can be used to infer the Ni dispersion (*Resini et al.*, 2009). The observed intensity of the 2039 cm^{-1} IR band decreases with increasing nickel content, which suggests that the presence of defect and low-coordinated Ni atoms decreases for the pre-reaction samples as Ni loading increases.

Pre-Reaction Sample	2100-2000 cm^{-1}	2000-1900 cm^{-1}	1900-1800 cm^{-1}
0.7% Ni/CZO	2039 cm^{-1} (s)	1960 cm^{-1} (w)	1895 cm^{-1} (s), 1863 cm^{-1} (s), 1826 cm^{-1} (s)
3% Ni/CZO	2039 cm^{-1} (w)	1959 cm^{-1} (w)	1829 cm^{-1} (s)
5% Ni/CZO	2038 cm^{-1} (w)	1955 cm^{-1} (w)	1829 cm^{-1} (s)
10% Ni/CZO	2037 cm^{-1} (w)	1957 cm^{-1} (w)	1834 cm^{-1} (s)

Table 4.3: Observed DRIFTS band positions and relative signal intensities for CO-adsorption on Ni (refer to Figure 4.7). Absorption intensities are denoted in parenthesis (s = strong; w = weak).

IR bands for bridged and multi-bonded Ni-CO ($Ni_{x\geq 2}$-CO) were also observed between 2000 cm^{-1} and 1800 cm^{-1} for each catalyst. It is generally accepted that the features between 2000-1930 cm^{-1} are associated with bridged species, Ni_2-CO, while

features between 1900-1800 cm^{-1} are associated with multi-bonded species, $Ni_{3,4}$-CO (*Blyholder*, 1964; *Hadjiivanov et al.*, 1999; *Agnelli et al.*, 1998; *Pereira and Martin*, 1993; *Hadjiivanov et al.*, 1998; *Blackmond and Ko*, 1985). The bridged-CO feature is very intense for 0.7 wt% Ni/CZO and much weaker for increased Ni loadings. The multi-bonded region (1900-1800 cm^{-1}) reveals that 0.7 wt% Ni/CZO contains multiple Ni_x-CO bonding features, while higher Ni loadings show one large Ni_x-CO feature. Such broad, low-frequency bands have been attributed to contributions of IR bands associated with triply- and quaternary-bonded Ni-CO on Ni [100] or [111] planes (*Blackmond and Ko*, 1985; *Campuzano and Greenler*, 1979; *Bertolini and Tardy*, 1981). It is evident that the catalysts that experienced hydrothermal aging primarily exhibited such low-frequency CO absorptions, indicating a larger prevalence of Ni [100] and [111] surfaces as compared to the catalyst with the lowest Ni content.

4.3.3 ATR of Isooctane

Characterization of the pre-reaction catalysts described in Table 4.1 has provided strong evidence that these samples represent a range of mean particle sizes resulting in measurable differences in chemical behavior, all while possessing equivalent active surface area. These catalysts were then tested for their ATR performance to determine the influence of particle size upon actual catalytic behavior. The experiments were performed under both sulfur-free and thiophene-doped conditions in order to specifically describe the influence of particle size on the poisoning of Ni by sulfur.

Isooctane ATR was carried out at a H_2O/C equal to 3, and O/C equal to 0.75. As the desired product of this reaction is synthesis gas (H_2 and CO), the idealized stoichiometry of Reaction 4.5 may be used as a guide for describing this reaction. Based upon this stoichiometry, the maximum yield of synthesis gas (Y_{SG}) is 1.12. Previous analysis has shown that the equilibrium predicted Y_{SG} is 1.11 for these inlet conditions (*Mayne et al.*, 2010). However, these past results have also demonstrated

that actual Y_{SG} is limited by poor isooctane conversion (X < 90%). Specifically, for a non-hydrothermally aged 10% Ni/CZO catalyst, Y_{SG} was 0.87.

$$C_8H_{18} + 2H_2O + 3O_2 \overset{22H_2O}{\rightarrow} 11H_2 + 8CO \tag{4.5}$$

The reaction shown in 4.5 familiarizes the reader with the reactants and desired products of this reaction but masks the complex reaction mechanism which other researchers have endeavored to describe (*Horn et al.*, 2006, 2007; *Gould et al.*, 2007; *Shekhawat et al.*, 2006; *Qi et al.*, 2005; *Yoon et al.*, 2008). For the purposes of this discussion the mechanism may be summarized as one consisting of roughly three different regions. Immediately upstream of the catalyst, thermal energy drives the cracking of a portion of the isooctane feed into mainly olefin products such as isobutylene and propylene. Highly exothermic partial and total oxidation reactions convert another portion of the isooctane feed near the front edge of the catalyst. This is followed by the balance of the catalyst bed wherein steam reforming and water gas shift pathways drive the remaining isooctane and cracking products towards an equilibrium dictated mixture of mostly H_2O, H_2, CO, and CO_2 with a smaller amount of CH_4.

The Y_{SG} versus time-on-stream is plotted for all of the catalytic tests of this study in Figure 4.8. In all cases the activity was fairly stable throughout the duration of the experiment. Results were found to be reproducible when samples were taken from the same synthesis batch and also when the catalyst was prepared again. The standard errors from these separate sources (catalyst preparation and random variation in reactor performance) were not statistically different; therefore they were combined for all of the reported data. The dashed lines in Figure 4.8 denote the time-averaged Y_{SG}, which may be taken as the steady-state value due to the minimal deviation over time-on-stream. These steady-state values are also plotted as a function of the d_p of

each catalyst in Figure 4.9a.

These results demonstrate the effect of particle size on both sulfur-free and thiophene doped isooctane ATR. Under sulfur-free reforming conditions decreasing particle size has a negative impact on Y_{SG}. This is contradictory to the expected trend. As prior studies have demonstrated that higher-dispersed Ni catalysts (smaller d_p) are more active to reforming reactions (*Jones et al.*, 2008), it would be logical to predict that smaller particles would result in higher Y_{SG}. However, the Y_{SG} increases from 0.56 for the <5 nm Ni particles of the 0.7% Ni/CZO catalyst to 0.83 for the 50-60 nm 10% Ni/CZO.

Further evidence suggests that while reforming reactions have been demonstrated to be more active on smaller particles they are actually less active in an ATR environment. Figure 4.10 shows the breakdown of carbon exiting the reactor. As in the previously reported data, the 10 wt% Ni/CZO exhibits nearly 90% isooctane conversion with essentially no olefin products such as isobutylene or propylene. The presence of those products would be associated with poor steam-reforming activity as they are primarily the product of the cracking mechanisms and are converted in endothermic steam reforming pathways to CO and H_2 (*Qi et al.*, 2005; *Yoon et al.*, 2008).

Compared to the 10 wt% Ni/CZO sample, the 5% and 3% samples have lower conversion, but a similar breakdown of carbon species. This observation suggests that olefins were still completely converted to reforming products but the unconverted isooctane was more difficult to reform as the Ni particle size decreased. One possible explanation for this phenomenon is that smaller Ni particles result in smaller ensembles of sites preventing the adsorption of isooctane. Similar ensemble size effects have been used to previously describe the interaction of sulfur with catalyst surfaces (*Rodriguez*, 2006). Compared to the other three samples, the 0.7% Ni/CZO sample had lower isooctane conversion, but now about 5% of the carbon is exiting the reactor as

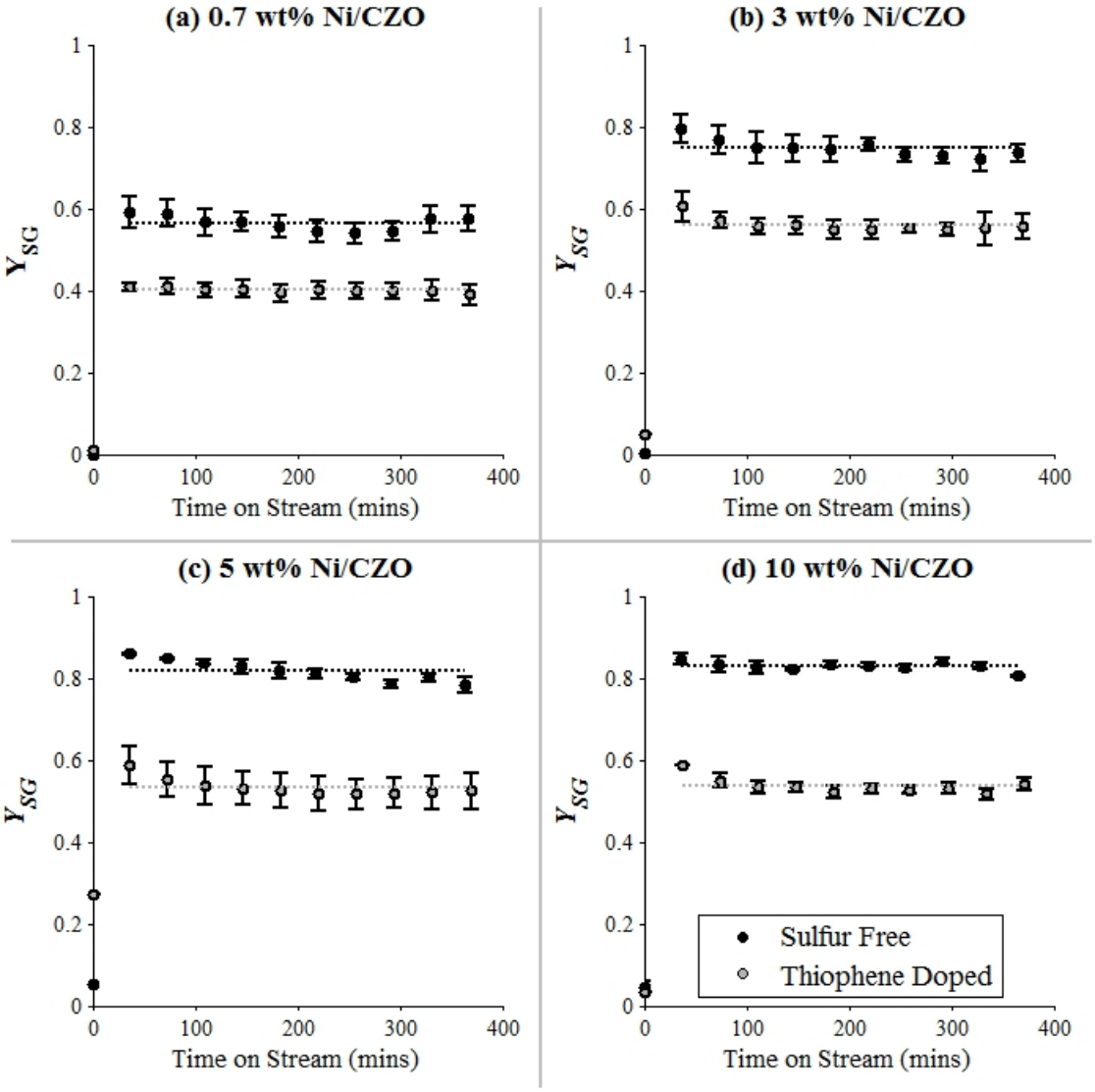

Figure 4.8: Results of isooctane ATR experiments. Time-on-stream YSG for the four different Ni/CZO catalysts studied run under sulfur free and thiophene doped conditions. The results from the non-aged 0.7% Ni/CZO are shown in (a), the results for the 3% Ni/CZO, 5% Ni/CZO, and 10% Ni/CZO, aged as described in Table 4.1, are displayed in (b), (c), and (d), respectively. The reported values at each time point are averaged across the three experiments run at each condition. The dashed lines represent the steady-state time-averaged Y_{SG}. (Reactor Conditions: $H_2O/C = 3$, $O/C = 0.75$, GHSV = 200 k hr^{-1}, Tinlet = 500°C, [S]in = 0 or 7.9 ppmv.)

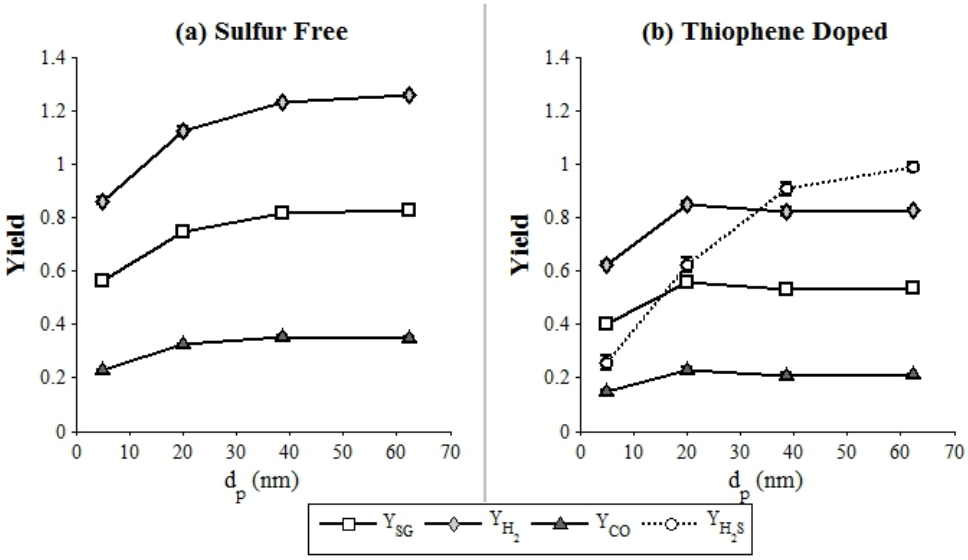

Figure 4.9: Steady-state yields of major species from the sulfur free (a) and thiophene doped (b) isooctane ATR displayed as a function of pre-reaction Ni particle size, as measured or extrapolated (see Figure 4.3).

olefins, mostly isobutylene.

The temperatures measured through the reactor bed demonstrate the thermal consequences of the diminished reforming activity. Figure 4.11a shows the sulfur-free temperature profiles, while Figure 4.12a shows the maximum catalyst bed temperature and the temperature at the bottom face of the catalyst bed as a function of the Ni particle size. As the reforming performance is diminished for smaller particle sizes the temperature of the catalyst bed progressively increases.

The influence of particle size on sulfur tolerance of the ATR reaction is found by examining the performance of the catalyst under conditions of thiophene exposure. As in sulfur-free conditions the time-on-stream data shows stable performance over the course of all the thiophene doped experiments (Figure 4.8). However, the influence of particle size upon Y_{SG} is not as dramatic when thiophene is present. As shown in Figure 4.9b, there is little to no difference in steady-state yields as a function of particle size except in the case of the 0.7% Ni catalyst which performed more poorly than the other catalysts.

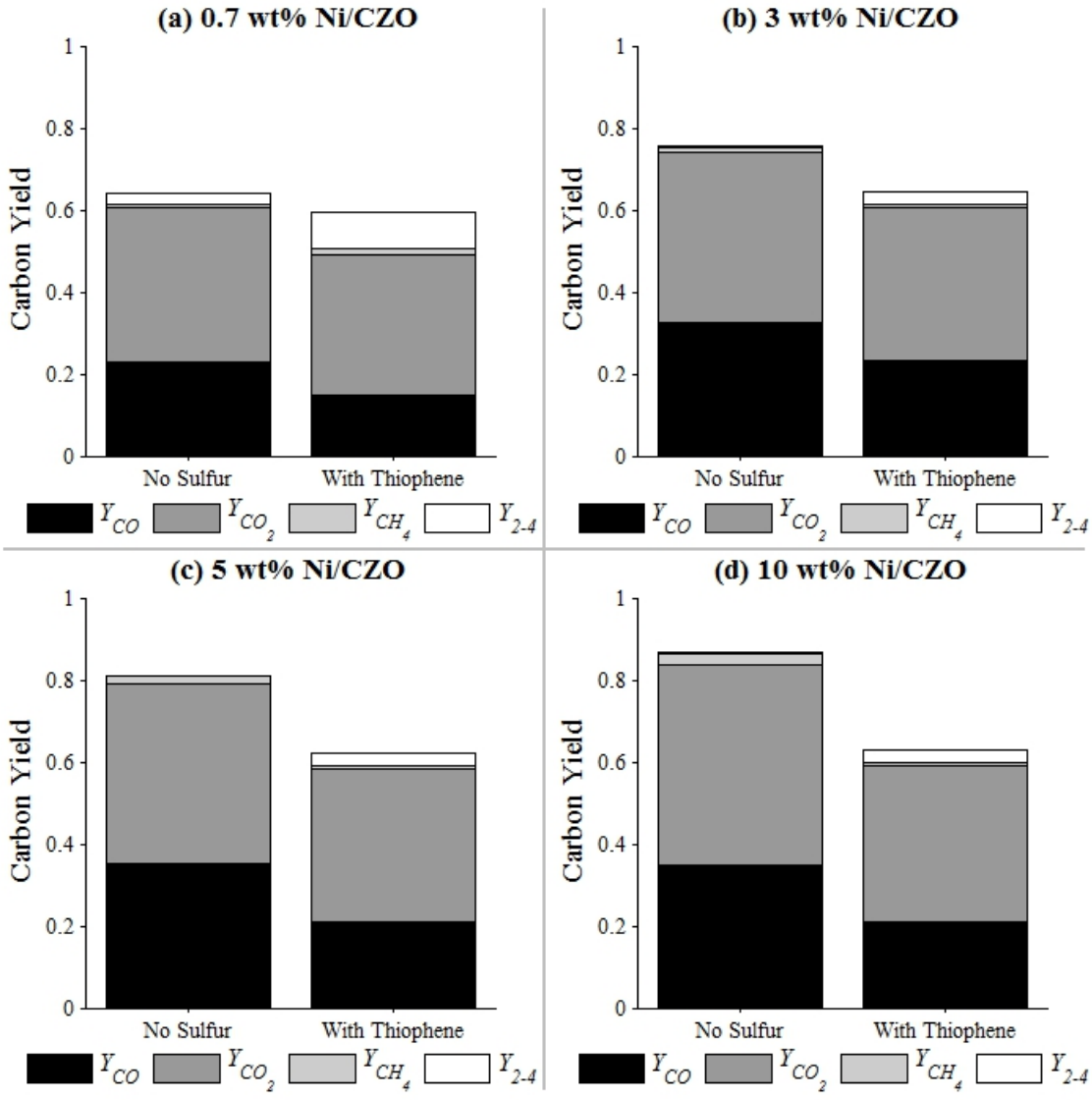

Figure 4.10: Steady-state carbon balance from the sulfur free and thiophene doped isooctane ATR experiments for the four catalysts tested.

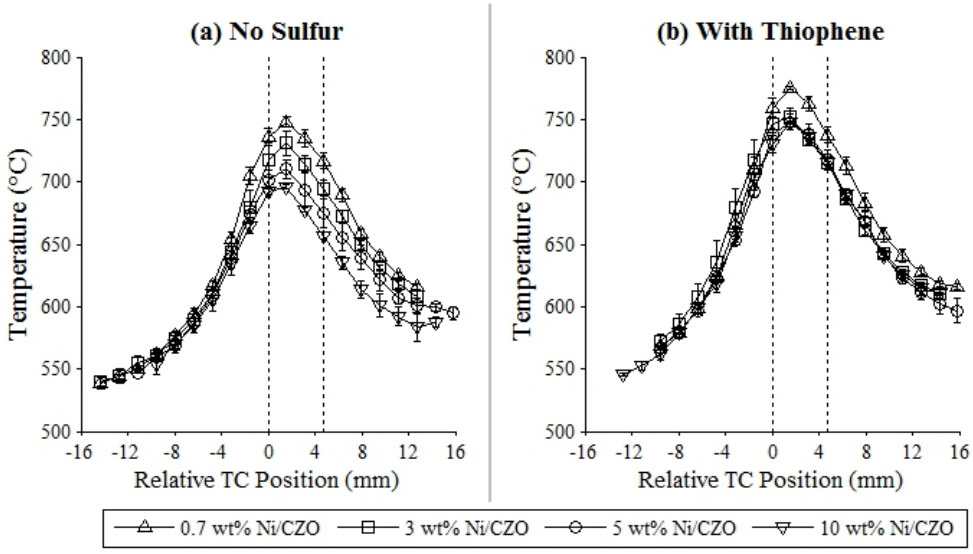

Figure 4.11: Temperature profiles measured through the vertical (flow) axis of the reactor bed during sulfur free (a) and thiophene doped (b) isooctane ATR. Profiles were measured near the end of each experiment and averaged across the three repeats of each experimental condition.

When comparing the carbon fractions for thiophene doped isooctane ATR shown in Figure 4.10, it is clear that there is not a significant difference between the performances of the three samples possessing the largest nickel particle sizes. Furthermore, the isooctane conversion and breakdown of carbon species is nearly identical in those three cases to the same metrics in the sulfur-free 0.7% Ni/CZO experiments. Figure 4.11b and Figure 4.12b similarly show that the temperature profiles for the samples with a d_p higher than 20nm are essentially identical. This trend does not extend to the 0.7% Ni sample. In that case, the catalyst bed temperature is higher, the isooctane conversion is lower, and the relative contribution of isobutylene and propylene are substantially increased.

The yield of H_2S is displayed in Figure 4.9b. It has been previously demonstrated that under many reforming conditions the conversion of thiophene to H_2S correlates with stable time-on-stream yields and conversion (*Mayne et al.*, 2010). It was proposed that this was due to low hydrogen availability, which would be needed to clean

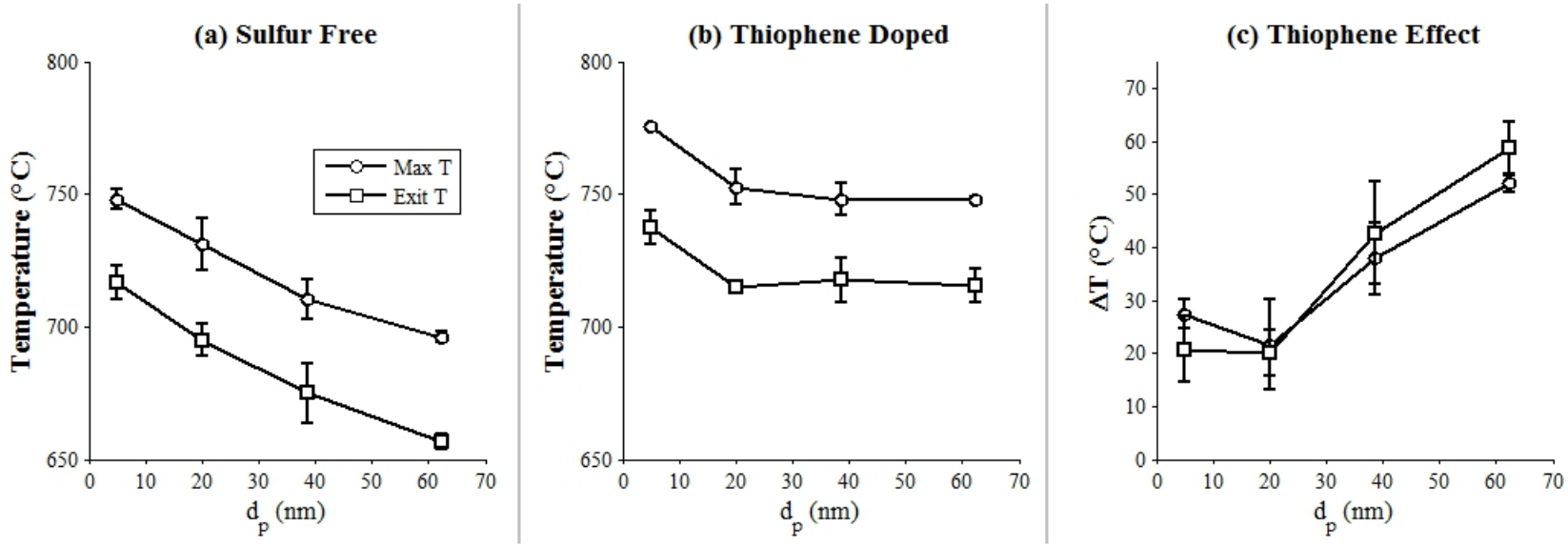

Figure 4.12: Maximum catalyst bed temperature and exit bed temperature as a function of pre-reaction Ni particle size for sulfur free ATR (a), thiophene doped ATR (b), and the influence of thiophene on the catalyst bed temperatures (c).

any sulfur bound to the surface. Based upon that theory, as surface sulfur concentration increases the reforming activity should decline as would the rates of thiophene hydrodesulfurization.

However, the results presented here demonstrate that this trend does not hold for smaller particles of Ni. For example, as the average particle size decreases from 50-60 nm to 20 nm, the yield of H_2S drops by a factor of two. In addition, there is no decline in activity over time-on-stream and there is not a measureable decrease in reforming yields. For the smallest particles, the yields of synthesis gas and H_2S are significantly lower, but again the activity remains constant over the course of the experiment.

These results suggest that sulfur molecules have an ever decreasing interaction with Ni as the particle size is decreased. However, the sulfur-free activity demonstrates this is not due to elevated reforming activity, which is significantly diminished in the case of smaller Ni d_p. Figure 4.13 and Figure 4.12c further demonstrate how the undesirable effects of thiophene exposure are diminished as the Ni particle size is decreased. In Figure 4.13, pertinent yields and conversion under sulfur free ATR are subtracted from those of thiophene doped isooctane ATR. Similarly, Figure 4.12c depicts the difference in catalyst bed temperature due to the presence of thiophene. These metrics are useful in demonstrating the influence of thiophene on these values.

Thiophene exposure increases the presence of olefins while decreasing X and Y_{SG}. These effects are more pronounced as the particle size is increased. However, this is simply due to the fact that the bigger Ni particles were more active under sulfur free conditions. In this sense, thiophene eliminated the disparity in performance caused by different particle sizes.

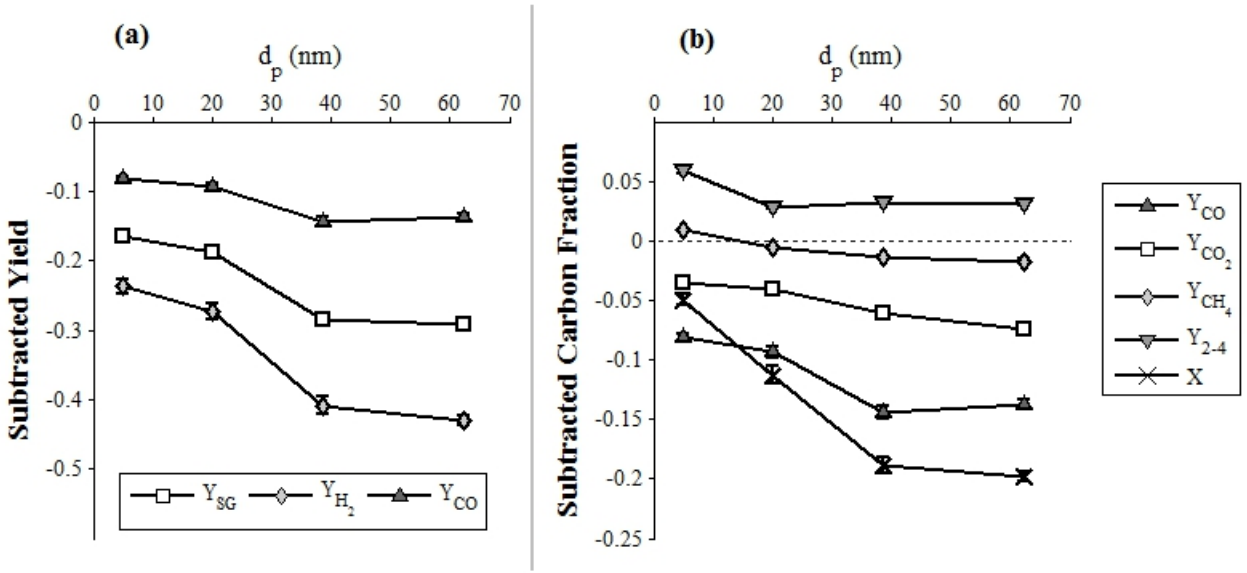

Figure 4.13: Influence of thiophene presence on pertinent yields and carbon fractions displayed as a function of pre-reaction Ni particle size. Results were obtained by subtracting steady-state sulfur-free results from corresponding thiophene doped values.

4.3.4 Characterization of Post-Reaction Catalysts

The core of the experimental design of this study was that the initial catalytic materials were prepared such that they had identical active surface area with a broad range of average particle sizes. However, the description of particle size trends above should be tempered with the fact that under reaction conditions it is expected that these variables would change, beyond the control of the experiment design. In order to provide full disclosure of this effect, the S_A of the post-reaction catalysts were measured using H_2 chemisorption. The results of this analysis, shown in Table 4.4, suggested that the active Ni S_A decreased significantly over the course of the ATR runs. This effect was more pronounced for smaller values of pre-reaction d_p, and also for thiophene doped isooctane ATR. The S_A was low enough for some of the experimental conditions that the measured values of H_2 uptake was at the limit of detection, resulting in the large standard errors reported in Table 4.4.

Pre-Reaction Sample	S_A (m^2/g)	XRD Ni [111] d_p (nm)	XRD Ni [200] d_p (nm)
0.7% Ni no C_4H_4S	0.047 ± 0.021	N/A	N/A
0.7% Ni w/ C_4H_4S	0.011 ± 0.010	N/A	N/A
3% Ni no C_4H_4S	0.049 ± 0.007	85.7 ± 8.4	77.5 ± 13.3
3% Ni w/ C_4H_4S	0.027 ± 0.027	85.0 ± 5.7	74.2 ± 3.1
5% Ni no C_4H_4S	0.100 ± 0.003	83.1 ± 6.7	72.9 ± 4.1
5% Ni w/ C_4H_4S	0.034 ± 0.017	88.8 ± 7.4	83.7 ± 14.6
10% Ni no C_4H_4S	0.148 ± 0.030	104.9 ± 12.3	87.4 ± 7.8
10% Ni w/ C_4H_4S	0.020 ± 0.007	114.6 ± 10.1	90.7 ± 6.5

Table 4.4: Post-reaction S_A, as measured by H_2 Chemisorption, and Ni particle size, as measured by XRD, of the Ni/CZO catalysts following ATR.

Table 4.4 also reports the XRD calculated Ni d_p for the post-reaction samples. Corroborating the chemisorption results, the XRD data shows that the Ni particle sizes of the catalysts increased significantly over the course of the ATR experiments. This increase was most dramatic for the 3% Ni catalyst and least dramatic for the 10% Ni sample. However, unlike the chemisorption results, the XRD data suggests

that thiophene exposure had no statistical effect upon post-reaction d_p. This apparent discrepancy may be explained by the formation of surface sulfides in the presence of thiophene.

The results of Table 4.4 may be taken to imply that the S_A decreased significantly for catalysts which underwent less extensive hydrothermal reduction, and therefore the micro-structure of small Ni particles were simply not as stable as the structure of the large Ni particles. However, it seems that the rate of sintering during reaction was most strongly dependent upon the catalyst bed temperature. For example, the S_A of the 3%, 5% and 10% Ni catalysts following thiophene exposed ATR were reasonably similar despite their large difference in initial particle size. As the temperature profiles illustrated the catalyst temperatures during these experiments were very similar.

As the TPR and TPO analysis of the pre-reaction catalysts demonstrated, the oxidation of smaller particles was achieved at lower temperatures than the oxidation of larger particles. As no deviation in the reduction feature locations were observed, it would follow that under ATR conditions the in-situ oxidation state of Ni would be closely related to particle size. By analyzing TPR profiles of post-reaction samples, it is clear that this is the case. Figure 4.14 shows that the average oxidation state of Ni is very high for the catalyst which initially had the smallest Ni particle size. Conversely, the average oxidation state of the largest particles was below +1. While it appears that the presence of thiophene may have, on average, lowered the oxidation state of Ni for the intermediate sized particles, the large error associated with this analysis makes this distinction difficult to infer with statistical confidence.

XPS was used to further characterize the surface of the post-reaction catalyst. The Ni 2p region is shown in Figure 4.15 for post-reaction samples at each experimental condition. The total intensity of the Ni 2p region compared to other peaks, such as the Ce 3d line, was found to increase as a function of Ni loading with a correlation coefficient of over 0.95. The peaks in the Ni spectra seen at 872, 861, and 855 eV

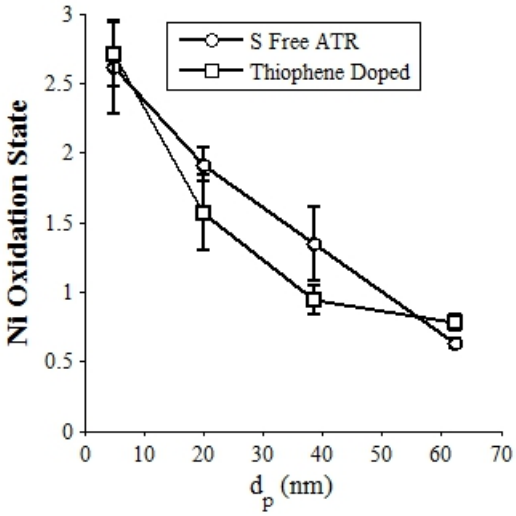

Figure 4.14: Post-reaction average Ni oxidation state as determined by TPR given as a function of pre-reaction Ni particle size.

can be attributed to Ni $2p_{1/2}$ satellite and $2p_{3/2}$ lines, respectively (*McIntyre and Cook*, 1975; *Srinivas et al.*, 2003). Previous researchers have demonstrated that the position of the Ni $2p_{3/2}$ line can be related to the oxidation state of the surface Ni species, with a BE of around 855 eV attributed to $Ni^{2+/3+}$ species and a BE of around 852 eV attributed to metallic Ni (*Shaju et al.*, 2003). Figure 4.15 clearly shows two distinct $2p_{3/2}$ features suggesting the presence of both Ni^0 and $Ni^{2+/3+}$ present in all samples except the 3% Ni/CZO catalyst following the thiophene doped isooctane ATR experiment.

Measuring the difference between the main $2p_{3/2}$ and the satellite line positions has been related to changes in the oxidation state of Ni and the electronegativity of Ni-bound ligands (*Allen et al.*, 1989; *Grosvenor et al.*, 2006). The values of this difference, $\Delta(LS)_3$, measured for the spectra in Figure 4.15 are listed in Table 4.5. The value of satellite displacement was found to generally increase as a function of the particle size of the initial catalyst material. This increase corroborates the findings of the TPR analyses, suggesting that the oxidation state of the Ni increased for smaller Ni particles during the ATR experiments. For the purposes of comparison,

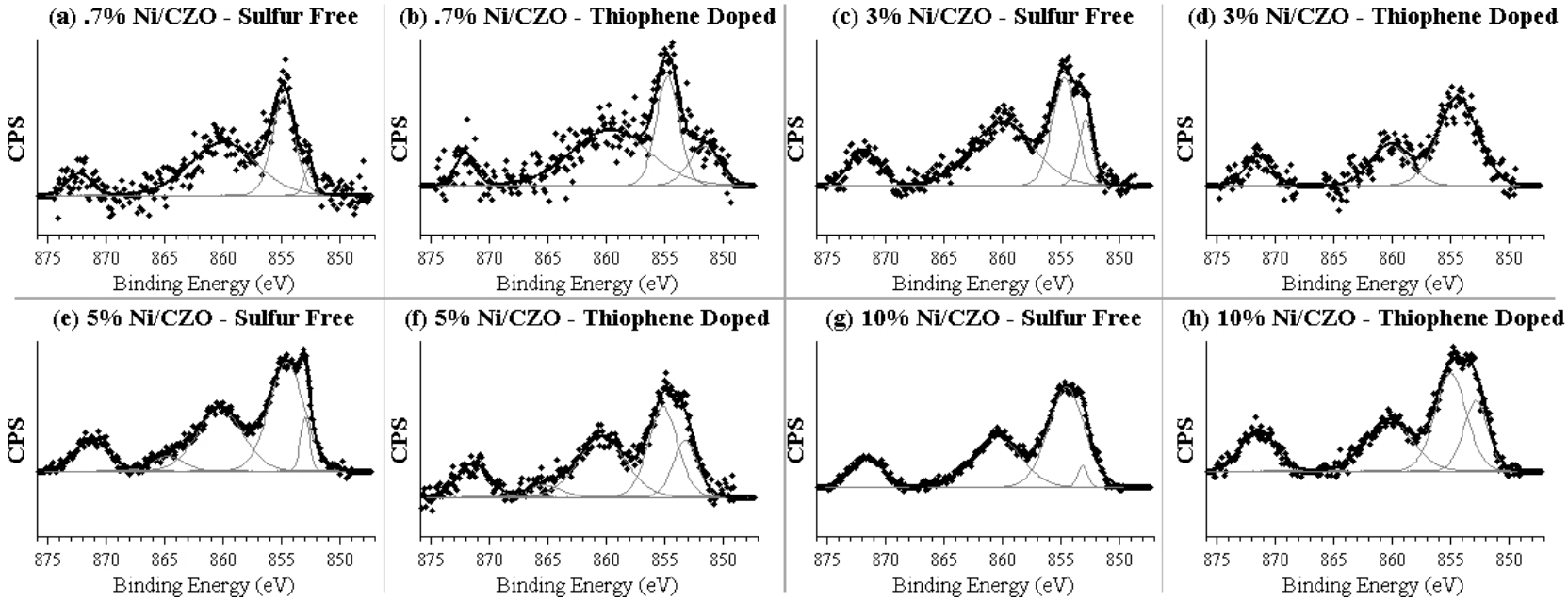

Figure 4.15: Representative post-reaction Ni 2p Core X-Ray Photelectron Spectra. The backgrounds of these spectra have been subtracted and the peaks have been deconvoluted.

the expected satellite displacements for metallic Ni and NiO are 6 eV and 3.5 eV, respectively (*Grosvenor et al.*, 2006).

Post-Reaction Sample	$\Delta(LS)_3$ (eV)
0.7% Ni no C_4H_4S	5.149
0.7% Ni w/ C_4H_4S	4.925
3% Ni no C_4H_4S	5.306
3% Ni w/ C_4H_4S	5.794
5% Ni no C_4H_4S	5.705
5% Ni w/ C_4H_4S	5.258
10% Ni no C_4H_4S	5.976
10% Ni w/ C_4H_4S	5.263

Table 4.5: Satellite displacement measurements from the XPS Ni $2p_{3/2}$ line in the spectra shown in Figure 4.15.

The satellite displacement was lower for three of the samples which had been exposed to thiophene, while it was higher for the 3% Ni/CZO catalyst. A shift in the satellite position to lower binding energies may suggest the binding of a more electropositive ligand than oxygen, such as sulfur. However, no peaks were seen in the S 2p region of the spectrum (165 eV) to corroborate the presence of surface bound sulfur species. Unfortunately, the poor signal-to-noise ratio of this region makes it difficult to make a definitive determination as to the presence or absence of sulfur using this method.

The apparent correlation between pre-reaction Ni particle size and the post-reaction measured Ni oxidation state offers a possible explanation for the poor reforming activity of small Ni particles. TPO of the pre-reaction catalysts demonstrated that smaller Ni particles were completely oxidized at significantly lower temperatures. This suggests that the active site for reforming reactions, Ni^0, is less stable for these smaller particles under the ATR reaction environment. It is feasible that the formation of surface or bulk nickel oxide can have a detrimental effect on the reforming activity of hydrocarbons, such as isooctane and isobutylene, as does the interaction of sulfur with active sites.

4.4 Conclusions

This study investigated the influence of Ni particle size upon isooctane ATR. Ni particle size was effectively controlled by altering the loading of the metal over a $Ce_{0.75}Zr_{0.25}O_2$ support material. The catalyst design corrected for the additional influence of Ni loading upon active metallic S_A. This was achieved by selectively aging the catalyst material under hydrothermal reducing conditions such that the pre-reaction catalysts all exhibited identical S_A, as measured by H_2 chemisorption. This approach allowed for the specific effects of particle size to be determined. Characterization of the pre-reaction materials convincingly demonstrated the disparity in particle size distributions between the separate samples and that such differences resulted in measurable changes in the surface reactivity of the Ni sites.

The catalytic materials were then tested under sulfur free and thiophene doped reaction conditions in order to determine the effect of particle size on these separate conditions. It was found that under sulfur free conditions, Ni particle size has a significant influence on the activity of the catalyst towards production of synthesis gas. Surprisingly, it was the highly dispersed small Ni particles (<5 nm) which exhibited unfavorable reaction characteristics. High catalyst temperature and increased olefin output suggested that the catalyst exhibited poor steam reforming activity. This effect of particle size was somewhat negated with the presence of thiophene in the feed stream. There was more pronounced deactivation of the larger Ni particles due to thiophene addition.

Two possible theories were presented which explain the role of particle size based upon an analysis of the products of the reforming reaction and post-reaction characterization of the catalytic material. The first theory suggests that smaller ensemble sizes of Ni found on the smallest Ni particles limited the reforming activity, especially of a hydrocarbon the size of isooctane. The second theory was based upon the differences in the apparent reducibility of the different catalysts. As the small particles

were more easily oxidized it is possible that this would also limit the reforming of hydrocarbons.

CHAPTER V

Modified Ni-based Catalysts for Sulfur-exposed Autothermal Reforming of Isooctane

This chapter describes some initial efforts to identify bimetallic catalysts which might offer increased durability compared to monometallic nickel catalysts when exposed to sulfur during the ATR of isooctane. Twelve different Ni-based catalysts were tested, including Fe, Au, Ag, Pt, and W modified Ni and monometallic Ni catalysts. These experiments identified two promising materials for more sulfur tolerant ATR catalysts (0.1% W modified 5% Ni/CZO and 0.2% Pt modified 10% Ni/CZO). These two samples demonstrated an elevated yield of H_2 and CO as well as an extended period of time before excessive deactivation was observed. The site-blocking interaction that Au has upon Ni catalysts offers additional insights into the nature of site-specific poisoning by sulfur compounds during ATR of isooctane.

5.1 Introduction to Bimetallic Reforming Catalysis

Efforts to develop fuel processors which convert liquid fuels into hydrogen rich feed streams are hampered by the propensity of the catalysts to deactivation from

carbon deposition and sulfur compounds present in the feed. Various efforts are present in the literature to attack these issues, with the most common approaches involving the identification and testing of novel catalyst formulations. One example is the development of bimetallic catalyst formulations. These materials consist of a primary supported metal which is either promoted by, or alloyed with, another metal.

There are essentially three possible ways that the addition of another metal can alter the reactivity of a catalyst (*Demirci*, 2007). First, the altered catalytic surface may exhibit new possible adsorption geometries. Second, the formation of an alloy can result in a surface with significantly altered reactivity compared to either monometallic surface. And third, the surface energies of the system may favor the segregation of one metal or another at the surface.

Significant theoretical progress has been made to predict the behavior of new bimetallic catalysts (*Ruban et al.*, 1997, 1999; *Greeley et al.*, 2002). Of particular interest is the effect that surface-alloying has upon the position of the ϵ_d in the electronic configuration of the metal. The d-band center has been used by some as a short-hand for describing the reactivity of a transition-metal surface (*Hammer and Norskov*, 1995). This is because when comparing the substrate-adsorbate interaction across a range of transition metal substrates for a fixed geometry, the most important single parameter is the relation of the d-band center relative to the Fermi level of the material. For example, a higher ϵ_d yields a stronger adsorbate-substrate interaction.

The influence of surface alloying on ϵ_d for Ni can be seen in Table 5.1 for a few ad-metals (*Ruban et al.*, 1997). For purposes of reference ϵ_d for Ni is 1.29 eV below the Fermi-level. The addition of either an impurity layer or complete monolayer can either elevate (as in Pt, Au, and Ag) or lower (as in Fe) ϵ_d. If this were the dominant effect upon surface reactivity it may be expected that, for example, an iron modified nickel catalyst may be less reactive than a monometallic nickel catalyst.

However, there are two important caveats to consider when interpreting the ϵ_d

Solute Metal	Electron Configuration	$\Delta\epsilon_d$ impurity (eV)	$\Delta\epsilon_d$ overlayer (eV)	Segregation Behavior
Fe	$[Ar]d^6s^2$	-0.20	-0.04	Moderate anti-segregation
Au	$[Xe]f^{14}d^{10}s^1$	+0.63	+0.71	Strong segregation
Ag	$[Kr]d^{10}s^1$	+0.67	+0.68	Very-strong segregation
Pt	$[Xe]f^{14}d^9s^1$	+0.40	+0.54	Moderate segregation
W	$[Xe]f^{14}d^4s^2$	u/k	u/k	Strong anti-segregation

Table 5.1: Theoretical interaction of various transition metals with Ni. $\Delta\epsilon_d$ refers to the change in ϵ_d of Ni due to the presence of the ad-metal as an impurity or an overlayer. Segregation refers to agglomeration of the admetal at the surface of Ni, while anti-segregation refers to Ni agglomeration at the surface. Modified from *Ruban et al.* (1997, 1999).

trends shown in Table 5.1. First, the values for $\Delta\epsilon_d$ are calculated based upon a fixed geometry which may not accurately represent the behavior of a particular bimetallic system. Additionally, the effect of alloying on ϵ_d may not be the dominant factor in describing the behavior of an alloy. Surface segregation of either the admetal or solvent metal, or other ensemble type effects may play a much more critical role. Theoreticians have also made efforts to describe the segregation behavior based upon the surface energies of model systems (*Ruban et al.*, 1999). These behaviors are also summarized in Table 5.1. By way of example these calculations would suggest that silver atoms would tend to segregate at the Ni surface, while tungsten atoms would segregate in the bulk of the metal.

These revolutionary efforts offer hope that the properties of bimetallic catalysts may be predicted prior to their development. This is extremely advantageous because the development of bimetallic catalysts offers the potential benefit of finely-tuned reactivity, but at the relatively high cost of increased material complexity. The maturation of theoretical models would allow the experimentalist to carve through the multitude of bimetallic permutations and design an optimal material for a given application while avoiding the necessity for such approaches as high-throughput catalyst testing.

Unfortunately, the application of these theories to ATR catalysis may be problematic due to the already complex nature of the system and an incomplete atomic-level perspective of the underlying chemistry and catalyst structure. Prior researchers have demonstrated that reforming catalysts possesses a complex reaction network which includes thermal homogeneous cracking followed by the catalytic routes for mass-transfer limited exothermic oxidation and endothermic reforming (*Horn et al.*, 2006, 2007; *Gould et al.*, 2007; *Shekhawat et al.*, 2006; *Qi et al.*, 2005; *Yoon et al.*, 2008). The work presented in Chapter IV and Chapter V suggests that sustained activity of Ni/CZO catalysts under thiophene exposed reaction conditions is related to the ability to clean chemisorbed sulfur and maintain a reduced Ni surface. It is also possible that ensemble effects play an important role in determining the extent of sulfur tolerance.

This contribution discusses efforts to describe the sulfur tolerance of several Ni based bimetallic catalysts. The different admetals selected were iron, platinum, gold, silver, and tungsten. These metals were chosen because they represented a range of electronic structures and segregation phenomena when combined with Ni. Also, there is some evidence based upon a review of the literature that these materials may be useful in sulfur exposed reforming chemistry. Some preliminary results (not shown) also considered Cu and Sn, but these catalysts performed poorly compared to monometallic Ni/CZO catalysts at even low sulfur exposures, possibly due to the low active surface area of these bimetallics.

Ensemble effects and surface segregation are two topics of considerable interest here, therefore two separate metal loading scenarios were considered, a low and a high Ni loading (5 versus 10 wt%). In all cases the mass ratio of admetal to Ni was 1:50. Unfortunately, this approach led to a variation in the molar ratio. However, the most important issue in this study was to qualitatively describe the behavior of a Ni/CZO catalyst modified with a sub-monolayer loading of a second metal. The

actual concentrations of the metals was therefore not of particular interest.

There has been significant work on the combination of various noble metals with Ni to suppress the formation of carbon deposits. Specifically, both theoretical and experimental work has shown that the addition of gold to Ni-based catalysts decreases carbon formation (*Besenbacher et al.*, 1998; *Molenbroek et al.*, 2001; *Chin et al.*, 2006). There are several proposed reasons for this effect including that gold selectively blocks Ni sites most prone to carbon deposition. Overall gold decreases the activity of other nickel sites by altering the electronic structure of the surface. This less active catalyst is more advantageous for certain reforming scenarios because of the significant decreases in carbon deposition. However, there has not been investigation into the behavior of Au-Ni reforming systems during sulfur exposure. Such catalysts have been applied in HDS systems, and have been shown to decrease the rate of irreversible sulfide formation (*Suo et al.*, 2009).

The addition of Pt to Ni catalysts has also been employed by a number of researchers (*Parizotto et al.*, 2009; *Li et al.*, 2006, 2007; *Pillay and Johannes*, 2008; *Mikami et al.*, 2003). It has been found that Pt addition lowers the ignition temperature of CH_4 POX over Ni (*Choudhary et al.*, 1995; *Enger et al.*, 2009). Others have reported that Pt-Ni systems seem to lack the hot-spot formation that plagues POX and ATR catalyst beds, and this may be explained by a potential ability of Pt to stabilize the reduced state of the Ni surface. This attribute makes the Pt-Ni system of particular interest in terms of sulfur tolerance, and there is some evidence that surface alloying may decrease the extent of sulfur adsorption (*Pillay and Johannes*, 2008). In terms of particle size effects, *Yoshida et al.* (2009) has reported that both Au and Pt tend to increase the dispersion of Ni.

Considerably less extensive work has been done investigating the other systems discussed in this chapter. *Wang et al.* (2009) has reported that a Ni-W catalyst appears to have higher stability under sulfur exposure compared to monometallic Ni.

Several groups have investigated an iron-nickel bimetallic system and have attributed increased performance to increased active surface area due to a complex interaction with an alumina-spinel support (*Huang et al.*, 2010; *Moon and Ryu*, 2003). It is believed that the Ag-Ni system may behave similarly to the related Au-Ni system, with some theoretical and experimental work suggesting lower carbon deposition on the surface (*Parizotto et al.*, 2009; *Zhu et al.*, 2010).

The work presented in this chapter compares the activity of the various bimetallic catalysts head-to-head. A high sulfur concentration is used to determine the length of time required before the activity diminishes due to sulfur saturation of the catalyst bed. Catalyst temperature profiles and carbon balance provide clues of the internal chemistry for each catalyst formulation.

5.2 Experimental

5.2.1 Catalyst Preparation

The CZO support used in this study was prepared by the coprecipitation of $Ce(NO_3)_3{\cdot}6H_2O$ and $ZrOCl_2{\cdot}8H_2O$ using 4M NH_4OH as a precipitating agent. The precipitate was recovered by filtration and calcined in air at 800°C for 1 hour. Nickel catalysts were prepared by the incipient-wetness impregnation of $Ni(NO_3)_2{\cdot}6H_2O$ salt onto the CZO support. Two Ni loadings were considered in this study— 5 and 10 wt%. Following impregnation, the catalysts were calcined in air at 800°C for 45 minutes.

Modification of 5 wt% and 10 wt% Ni/CZO was achieved by first reducing the monometallic catalyst at 600°C for 30 minutes in 5% H_2 (balance N_2). The second metal (Fe, Au, Ag, Pt, or W) was impregnated using the appropriate salt precursor ($Fe(NO_3)_3{\cdot}9H_2O$, $AuCl_3{\cdot}xH_2O$, $AgNO_3$, $PtCl_4$, or WO_3). The admetal concentration was 0.1 wt% for the 5 wt% catalyst and 0.2 wt% for the 10 wt% Ni/CZO. The

bimetallic catalysts were calcined a final time in air for 4 hours at 500°C. For purposes of comparison, the corresponding monometallic Ni/CZO catalysts were also reduced and subsequently calcined for four hours.

5.2.2 ATR Experiments

The prepared catalysts were tested for their activity to the autothermal reforming of isooctane. The H_2O/C ratio in these experiments was 1.0, the O/C ratio was 0.75, and the GHSV was 200,000 hr^{-1}. The overall stoichiometry for this reaction is shown in Reaction 5.1. The flowrates fed to the reactor were 45.2 mmole/min Air, 25.5 mmole/min H_2O, and 3.19 mmole/min isooctane. In all experiments of this study the isooctane was doped with thiophene at a concentration of 230 ppmw. This is equivalent to a sulfur concentration of 87.71 ppmw in the fuel or 13.43 ppmv in the overall feed. This relatively high concentration of sulfur was used in order to analyze the breakthrough capacity of each catalyst.

$$C_8H_{18} + 2H_2O + 3O_2 \overset{6H_2O}{\rightarrow} 11H_2 + 8CO \tag{5.1}$$

In all of the experiments, 500 mg of catalyst was loaded into a quartz-wool supported fixed bed reactor, which consisted of a 1/2" quartz tube inside a furnace. Along the center-line of the reactor was a 1/8" closed-end quartz-tube which sheathed a thermocouple. This set-up allowed for the in situ measurement of catalyst temperature. In order to avoid adsorptive losses of VSCs, the reactor lines were silane-treated (obtained from Restek). Additional reactor details have been described previously (see Chapters II and III).

Prior to reaction, the catalysts are reduced at 600°C for 30 minutes in a flow mixture of 5% H_2 and 95% N_2. The catalyst was then cooled to 300°C, at which

temperature the reaction was initiated by switching on the reactant feed mixture (isooctane plus air plus steam). The reactor inlet temperature was then ramped to 500°C. This light-off followed by ramp protocol was used because it has previously been demonstrated that high temperatures can occur during start-up which are not advantageous for long-term performance (*Gould et al.*, 2007).

The reactor effluent was fed to a single-stage condenser which collected water vapor before the stream entered an on-line GC for quantitative analysis. A Varian CP-3800 GC was used to identify the gaseous products of the reaction (H_2, N_2, CO, CH_4, CO_2, ethylene, ethane, propylene, propane, H_2S, CH_3S, and thiophene). Molar flowrates were calculated from the composition data by using N_2 as an interal standard in the data analysis.

5.2.3 Benchmarking Catalyst Performance

Each experiment was carried out until steady-state performance was established, which was signaled by no change in species concentrations or catalyst temperature. Steady-state was reached for all experiments by between 19 and 25 hours of time-on-stream. In order to describe the performance of ATR under thiophene exposure for each catalyst several metrics will be discussed. First, the combined yield of synthesis gas (H_2 and CO) was calculated at each time on stream using Equation 5.2. This single metric describes the performance of the catalyst towards the desired reforming products. Due to the high thiophene concentration present in the feed, the Y_{SG} decreased over the course of time-on-stream for all experiments.

$$Y_{SG} = \frac{(F_{H_2} + F_{CO})_{,out}}{17 * F_{C_8H_{18},in}} \tag{5.2}$$

The initial activity was described by extrapolating the trend in Y_{SG} between the

second and third time points back to the starting-time of the experiment. This initial Y_{SG} was usually similar to the maximum Y_{SG}; in such cases this implied that the initial activity was nearly constant before the onset of deactivation. Also, the final three Y_{SG} points were averaged to describe the final activity of the catalyst after steady-state had been reached. For purposes of comparison, Figure 3.3a shows the Y_{SG} as a function of time-on-stream at the same inlet composition but for sulfur free ATR and for a lower concentration of thiophene than was used in this study. Compared the stoichiometric limit on Y_{SG} of 1.12, and the equilibrium predicted Y_{SG} of 1.08, the initial sulfur-free Y_{SG} was 0.995, and the initial Y_{SG} for an inlet sulfur concentration of 4.5 ppmv was 0.729.

The time at which catalyst deactivation was most reflected in Y_{SG} was used to describe how quickly the catalyst deactivated. This point was calculated based upon the derivative Y_{SG}. The time at which the change in Y_{SG} was most negative is described as the point of maximum deactivation, t_{md}. When the inlet sulfur concentration was 0 or 4.5, the Y_{SG} was stable for at-least 24 hours of time-on-stream, so it is assumed that $t_{md} > 24$ hours.

Temperature profiles were collected at steady-state conditions for each of the experiments of this study. The maximum catalyst bed temperature was used to compare the various catalysts tested. For the 10 wt% Ni/CZO catalyst tested in Chapter III, the maximum bed temperature was 698.1°C under sulfur-free isooctane ATR and 795.3°C when thiophene was present. The increased temperature was attributed to a significant drop in steam reforming activity, which also was responsible for the decrease in Y_{SG}.

The final performance consideration is the speciation of carbon– in other words, the yields of the various carbon products and the total conversion of isooctane (Equations 5.3-5.10). The initial and final isooctane conversion values were calculated for each experiment using the same method as was described above for Y_{SG}. According

to prior investigations, the S-free conversion of isooctane at these inlet conditions was found to be 96.8% and at the lower sulfur concentration of 4.5 ppmv, it was 90.8% (see Chapter III).

$$Y_{H_2} = \frac{F_{H_2,out}}{9 * F_{C_8H_{18},in}} \tag{5.3}$$

$$Y_{CO} = \frac{F_{CO,out}}{8 * F_{C_8H_{18},in}} \tag{5.4}$$

$$Y_{CO_2} = \frac{F_{CO_2,out}}{8 * F_{C_8H_{18},in}} \tag{5.5}$$

$$Y_{CH_4} = \frac{F_{CH_4,out}}{8 * F_{C_8H_{18},in}} \tag{5.6}$$

$$Y_{2-4} = \frac{\left(2 * F_{C_2H_4} + 2 * F_{C_2H_6} + 3 * F_{C_3H_6} + 3 * F_{C_3H_8} + 4 * F_{C_4H_8}\right)_{,out}}{8 * F_{C_8H_{18},in}} \tag{5.7}$$

$$Y_{H_2S} = \frac{F_{H_2S,out}}{F_{C_4H_4S,in}} \tag{5.8}$$

$$Y_{C_4H_4S} = 1 - X_{C_4H_4S} \approx \frac{F_{C_4H_4S,out}}{max\left(F_{C_4H_4S,out}\right)} \tag{5.9}$$

$$Y_{CH_3S} = \frac{F_{CH_3S,out}}{F_{C_4H_4S,in}} \tag{5.10}$$

In contrast to the conditions chosen in Chapter IV, the conditions explored in this study also have to contend with the issue of carbon deposition. For the purposes of describing the extent of carbon deposition in each experiment, the maximum amount of pressure drop is reported; this value is strongly correlated to the deposition of carbon. Pressure-drop data are useful in providing a more complete picture of the reactor environment.

The analysis of each monometallic or bimetallic catalyst was repeated in this study. The data described and discussed below are representative of the experiments performed.

5.3 Results and Discussion

5.3.1 Monometallic and Modified 5 wt% Ni/CZO

The initial activity of the monometallic 5% Ni/CZO catalyst was significantly impeded by the high concentration of thiophene which is evident by comparison to the equilibrium predicted Y_{SG} and sulfur-free isooctane conversion. The initial and final conversion along with the initial, final, and maximum Y_{SG} are displayed for all of the 5% Ni catalysts in Table 5.2. The time-on-stream data for these experiments are displayed in Figure 5.1.

Catalyst	X^0	X^f	Y^0_{SG}	Y^f_{SG}	Y^{max}_{SG}
5% Ni/CZO	0.775	0.942	0.554	0.304	0.555
Fe-Ni/CZO	0.751	0.787	0.521	0.251	0.526
Au-Ni/CZO	0.721	0.583	0.484	0.243	0.475
Ag-Ni/CZO	0.751	0.868	0.543	0.280	0.551
Pt-Ni/CZO	0.636	0.792	0.305	0.184	0.411
W-Ni/CZO	0.734	0.877	0.573	0.277	0.574

Table 5.2: Isooctane conversion and Y_{SG} from the isooctane ATR over 5% Ni/CZO based bimetallics. (Reactor conditions: $H_2O/C = 1$, $O/C = 0.75$, GHSV = 200 k h^{-1}, $T_{inlet} = 500°C$, $S_{in} = 13.43$ ppmv.)

The Y_{SG} is fairly constant for the first three hours of the reaction before the catalyst begins to experience an elevated rate of deactivation. According to the t_{md}, listed in Table 5.3, the maximum rate of deactivation was seen at around nine hours-on-stream. The high catalyst bed temperature suggests that the reforming activity was significantly diminished. The calculated yields of carbon species, shown in Figure 5.2, corroborate this interpretation as high isooctane conversion was seen with significant contribution from intermediate hydrocarbon species, such as isobutylene and propylene, and CO_2.

These combined observations suggest the importance of multiple types of sites and their corresponding interactions with sulfur. The fact that initial catalyst activity decreases with increasing sulfur concentration suggests one type of interaction. This

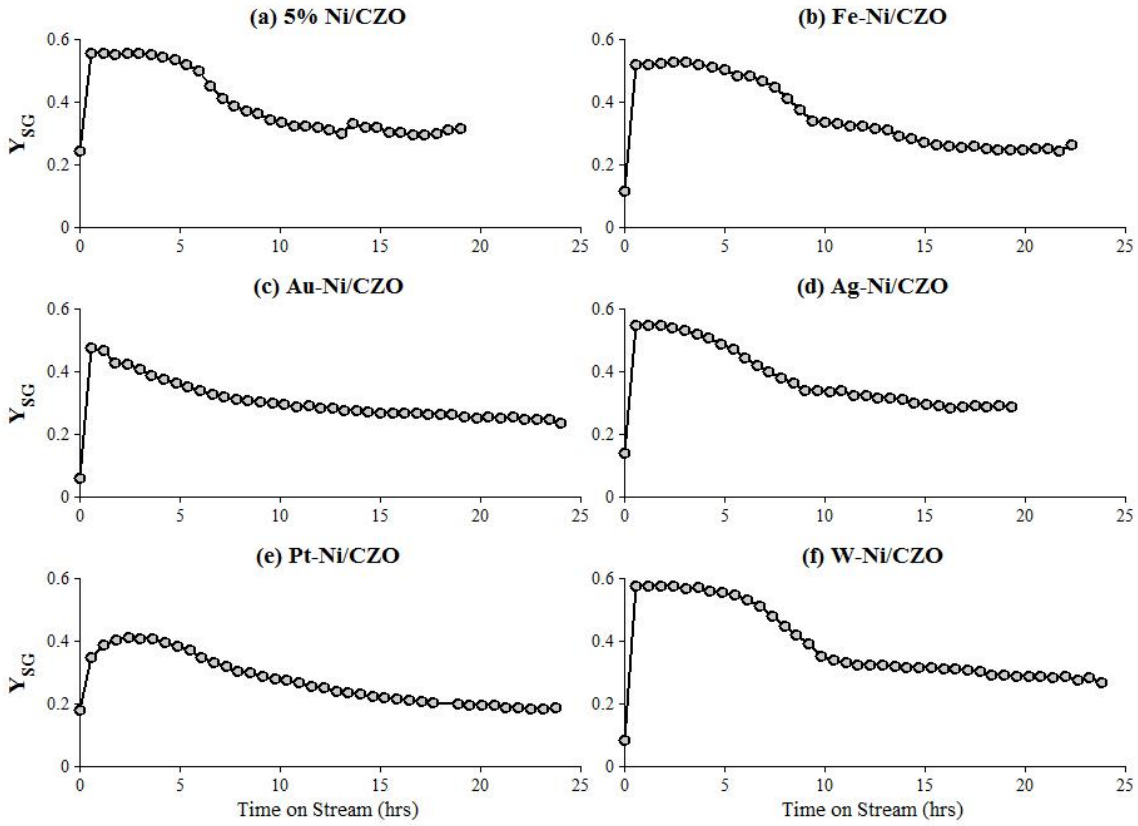

Figure 5.1: Time-on-stream Y_{SG} for monometallic 5% Ni/CZO (a), 0.1% Fe-5% Ni/CZO (b), 0.1% Au-5% Ni/CZO (c), 0.1% Ag-5% Ni/CZO (d), 0.1% Pt-5% Ni/CZO (e), and 0.1% W-5% Ni/CZO (f). (Reactor conditions: $H_2O/C = 1$, $O/C = 0.75$, GHSV = 200 k h^{-1}, $T_{inlet} = 500°C$, $S_{in} = 13.43$ ppmv.)

Catalyst	t_{md} (hours)	T^{max} (°C)	ΔP^{max} (psig)
5% Ni/CZO	7.78	839.96	10.09
Fe-Ni/CZO	8.07	798.89	10.89
Au-Ni/CZO	1.20	769.78	3.12
Ag-Ni/CZO	6.04	825.34	10.35
Pt-Ni/CZO	6.14	813.21	14.26
W-Ni/CZO	9.23	804.05	11.64

Table 5.3: Additional parameters describing the performance of the bimetallic catalysts based upon the 5% Ni/CZO precursor during ATR: the rate of maximum loss of Y_{SG}; the maximum catalyst bed temperature; and the maximum pressure drop across the catalyst bed. (Reactor conditions: $H_2O/C = 1$, $O/C = 0.75$, GHSV = 200 k h^{-1}, $T_{inlet} = 500°C$, $S_{in} = 13.43$ ppmv.)

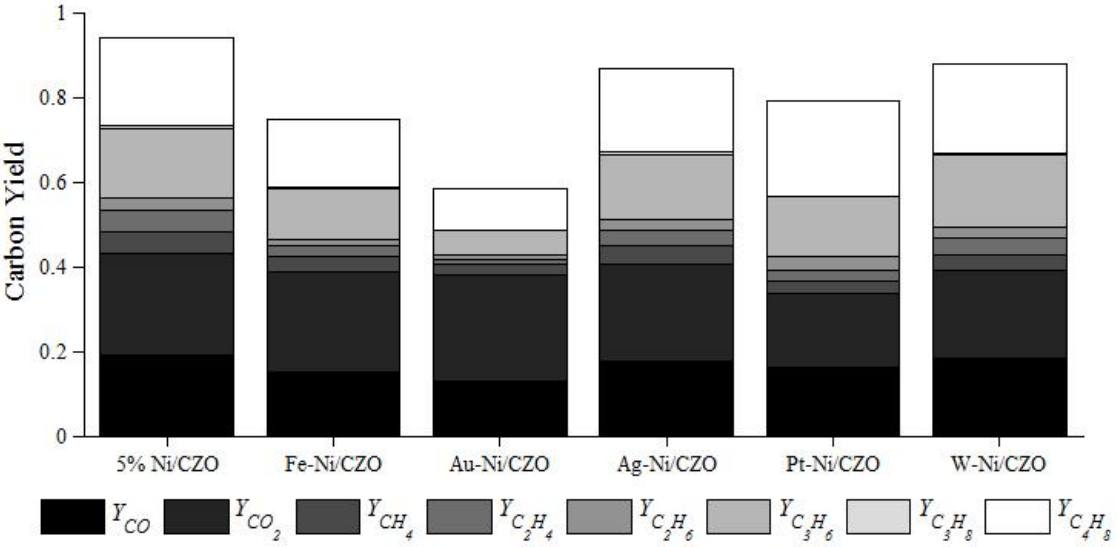

Figure 5.2: Steady-state carbon fractions for monometallic 5% Ni/CZO catalyst and associated bimetallics. (Reactor conditions: $H_2O/C = 1$, $O/C = 0.75$, GHSV = 200 k h^{-1}, $T_{inlet} = 500°C$, $S_{in} = 13.43$ ppmv.)

relationship suggests the presence of sulfur immediately impedes the ability of certain sites to reform hydrocarbons such as isobutylene, propylene, and non-homogeneously-cracked isooctane.

The delayed deactivation behavior after three-hours of constant activity suggests that the presence of other types of sites which are vulnerable to continual contact with sulfur compounds. There are two possible explanations for this phenomenon. One possibility is that increased build-up of sulfur on the surface begins to enact long-range deactivation on the Ni catalyst once a certain level of sulfur is reached. Alternatively, it is possible that low-activity sacrificial sites are being slowly saturated with adsorbed sulfur until saturation is reached at which point more reforming-active sites become prone to deactivation.

The continued presence of activity following the period of increased deactivation can likely be attributed to the activity of the support material. According to the results of Chapter II, the blank support has reforming activity which tends to decrease

slightly with time-on-stream. If this trend is extrapolated to the duration of the experiments considered in these studies, it is assumed that non-poisoned support might be expected to contribute a Y_{SG} of approximately 0.2. This analysis suggests that the steady-state activity of 5% Ni/CZO may be indicative of either the combination of essentially no Ni activity and sulfur-free support activity or some combination of diminished metal and support activities.

The Y_{SG} trend for the Fe-Ni/CZO catalyst was similar to that of the monometallic catalyst in terms of initial activity and the observed decrease in activity seen after around three hours-on-stream. The maximum decline in activity was seen at around nine hours. The only significant difference in the behavior of the Fe-Ni catalyst was a decreased conversion of isooctane, which correlated with a lower maximum catalyst bed temperature. The lower catalyst temperature suggests that the Fe-Ni catalyst was less prone to SR deactivation. However this is not supported by an analysis of the ratio of carbon species seen in the reactor effluent. There is, as in the monometallic case, a proportionally high production of CO_2, propylene, and isobutylene, suggesting a diminished SR activity. It is plausible that the lower catalyst temperature may be attributed to a deactivation of catalytic partial oxidation mechanisms.

The addition of gold to nickel catalysts has been used by several researchers and their industrial partners to drastically diminish the rate of carbon deposition, especially in methane SR reactors (*Besenbacher et al.*, 1998; *Molenbroek et al.*, 2001; *Chin et al.*, 2006). The low pressure drop seen in this study when studying Au-Ni catalysts seems to suggest that these materials may also be effective at reducing carbon deposition during the ATR of larger hydrocarbons. However, in every other aspect it is clear that the Au-Ni catalyst would be an undesirable catalyst under exposure to sulfur. In contrast to the monometallic 5% Ni catalyst, there is no stable initial activity. The Y_{SG} decreases dramatically almost as soon as the reaction is initiated. There is a lower catalyst bed temperature and lower overall conversion of isooctane.

The relatively high production of CO_2 suggests that sulfur has essentially no impact upon the mechanistic routes to CO_2 production, in other words total oxidation.

The efforts of both theoreticians and experimentalists have suggested that when added to a Ni surface, Au atoms tend to selectively block highly-active undercoordenated Ni sites. This site-blocking effect suggests that these same sites are those responsible for the short-lived stability of the Y_{SG}. However, this would seem to controvert the results of Chapter IV. By investigating the effects of particle size, it was discovered that the activity of these undercoordenated sites were not significantly diminished due to the presence of sulfur. On the other hand, the initial Y_{SG} of the monometallic Ni is significantly dependent upon sulfur concentration. The initial Y_{SG} at high sulfur concentration was lower than the Y_{SG} during ATR at low sulfur exposures, which was in turn lower than sulfur-free Y_{SG}. Therefore, since the activity of high-index plane surfaces does not possess a strong dependence on sulfur concentration, it necessarily follows that it must be other types of sites which are responsible for both a strong sulfur dependence and the eventual decline of initial Y_{SG}. The suppression of these sites by gold may also be explained by the work of theoreticians which suggested that the presence of gold impurities had a long-range impact on Ni activity. It is possible that in addition to blocking step Ni sites; the presence of Au may tend to further increase the effective coordination number of terrace Ni sites, rendering them less active.

Various researchers have proposed a similar behavior between the Ag-Ni and Au-Ni catalysts. In this study it is unclear that this is the case. It appears that the Ag-Ni catalysts do not exhibit a maintained initial activity, similar to the Au-Ni catalyst. However, the maximum rate of deactivation does not occur until approximately six hours-on-stream. It is possible that the effect of Ag addition is muted due to the experimental protocol which used a constant mass ratio of Ni and admetal. However, there are additional differences between the Au-Ni and Ag-Ni catalysts. For example,

the catalyst bed temperature is significantly hotter for the Ag-Ni catalyst, and the isooctane conversion was correspondingly high.

The time-on-stream data for the Pt-Ni catalyst (Figure 5.1e) demonstrated a slight increase in the Y_{SG} over the first three hours-on-stream. This suggests that the structure of the catalyst is not in a stable form prior to reaction. The low initial and final Y_{SG} may be remedied by a different pre-reaction treatment protocol. The maximum catalyst bed temperature was over 810°C, and the isooctane conversion was nearly 80%, with slightly lower contributions from CO_2 and CH_4 in the final carbon balance.

The W-Ni/CZO catalyst had the highest initial and final Y_{SG} of the catalysts based upon the 5 wt% Ni/CZO precursor. This makes this catalyst an interesting possibility for more sulfur-tolerant reformers. However, due to the lack of characterization work describing the interaction between tungsten and nickel it is difficult to speculate on the reasons for the marginal improvement in performance. The catalyst bed temperature was around 800°C, and the carbon fractions were very similar to the monometallic 5% Ni experiment.

5.3.2 Monometallic and Modified 10 wt% Ni/CZO

The results for the monometallic and bimetallic catalysts based upon the 10% Ni/CZO catalyst are displayed in Figures 5.3 and 5.4 and Tables 5.4 and 5.5. The monometallic 10% Ni/CZO catalyst had similar initial activity compared to the 5% Ni/CZO sample. However, it appears that the added Ni content led to a significant increase in the amount of carbon deposited on the catalyst as demonstrated by the increased pressure drop across the catalyst bed. It is clear that carbon deactivation was not advantageous for reactor performance as the maximum rate of deactivation was reached at around three hours. Additionally, the 10% Ni catalyst had a lower maximum bed temperature of around 790°C. This was associated with a lower isooctane

conversion.

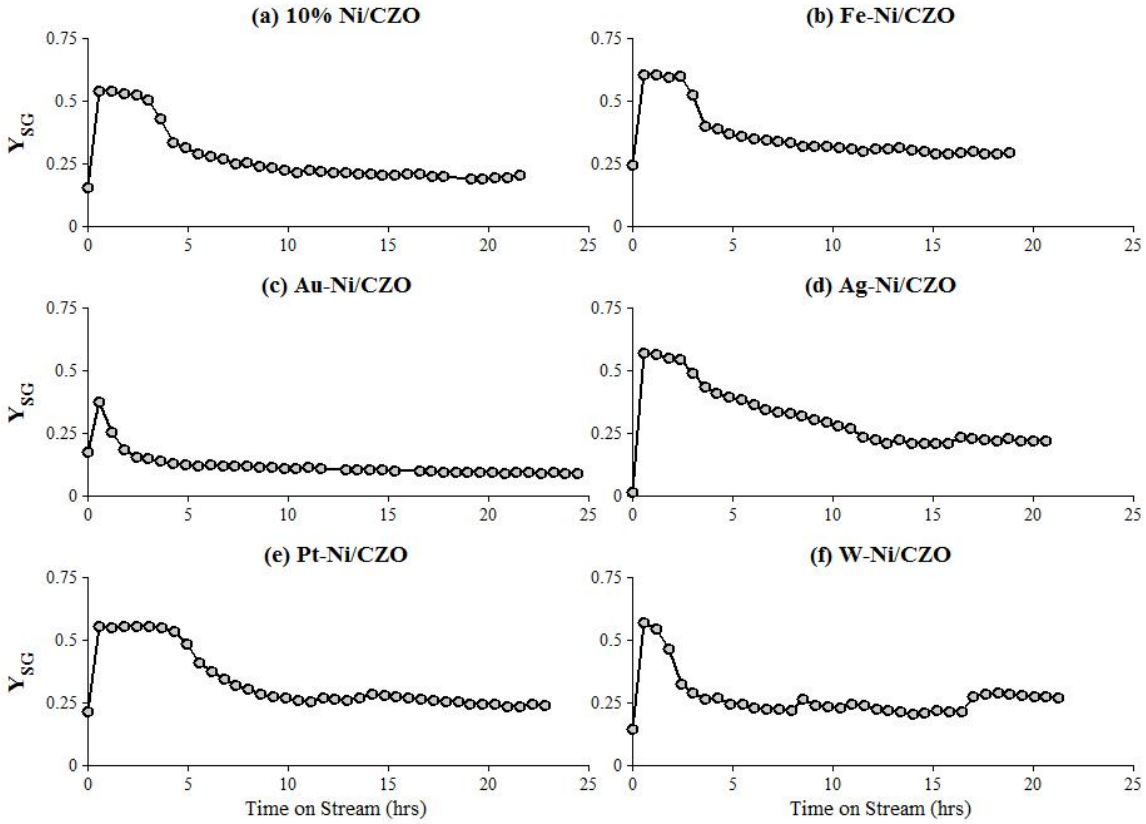

Figure 5.3: Time-on-stream Y_{SG} for monometallic 10% Ni/CZO (a), 0.1% Fe-10% Ni/CZO (b), 0.1% Au-10% Ni/CZO (c), 0.1% Ag-10% Ni/CZO (d), 0.1% Pt-10% Ni/CZO (e), and 0.1% W-10% Ni/CZO (f). (Reactor conditions: $H_2O/C = 1$, $O/C = 0.75$, GHSV = 200 k h^{-1}, $T_{inlet} = 500°C$, $S_{in} = 13.43$ ppmv.)

The 0.2%Fe-10%Ni catalyst had higher initial and final Y_{SG} and conversion than the 0.1%Fe-5% Ni catalyst. However, the maximum deactivation rate was reached significantly sooner— three versus eight hours. The pressure drop across the reactor was essentially unchanged between the two experiments, so it appears that any ensemble effects experienced by the two catalysts lead to a more stable activity for the lower loading catalyst.

The Au-Ni catalyst behaved very poorly. There was very low initial and final Y_{SG}. Compared to the 0.1%Au-5%Ni material, the 0.2%-10% catalyst had a higher catalyst

Catalyst	X^0	X^f	Y^0_{SG}	Y^f_{SG}	Y^{max}_{SG}
10% Ni/CZO	0.709	0.784	0.538	0.194	0.539
Fe-Ni/CZO	0.773	0.938	0.600	0.290	0.603
Au-Ni/CZO	0.617	0.696	0.486	0.089	0.370
Ag-Ni/CZO	0.812	0.913	0.568	0.221	0.566
Pt-Ni/CZO	0.705	0.532	0.587	0.160	0.576
W-Ni/CZO	0.652	0.858	0.594	0.273	0.569

Table 5.4: Isooctane conversion and Y_{SG} from the isooctane ATR over 10% Ni/CZO based bimetallics. (Reactor conditions: $H_2O/C = 1$, $O/C = 0.75$, GHSV = 200 k h^{-1}, $T_{inlet} = 500°C$, $S_{in} = 13.43$ ppmv.)

bed temperature and isooctane conversion. The benefits seen in terms of carbon deposition, did not extend to the higher loaded material, as there was similar pressure drop seen between the 0.2% Au-10% Ni and the monometallic 10% Ni catalyst.

Catalyst	t_{md} (hours)	T^{max} (°C)	ΔP^{max} (psig)
10% Ni/CZO	3.36	798.37	15.54
Fe-Ni/CZO	3.04	845.32	10.51
Au-Ni/CZO	1.22	787.66	13.12
Ag-Ni/CZO	3.03	836.90	15.08
Pt-Ni/CZO	5.87	754.21	16.22
W-Ni/CZO	1.83	831.07	15.88

Table 5.5: Additional parameters describing the performance of the bimetallic catalysts based upon the 10% Ni/CZO precursor during ATR: the rate of maximum loss of Y_{SG}; the maximum catalyst bed temperature; and the maximum pressure drop across the catalyst bed. (Reactor conditions: $H_2O/C = 1$, $O/C = 0.75$, GHSV = 200 k h^{-1}, $T_{inlet} = 500°C$, $S_{in} = 13.43$ ppmv.)

The 0.2% Ag-10% Ni catalyst behaved very similarly to the 0.1% Ag-5% Ni catalyst. There was similar catalyst bed temperatures and carbon speciation.

The Pt-Ni catalyst behaved well at the higher loading. The initial Y_{SG} was higher than the monometallic 10% Ni catalyst, and the maximum rate of deactivation was seen at the latest time-on-stream among the high metal loading catalysts. The catalyst bed temperature was 100°lower than the 0.1% Pt-5% Ni catalyst. Although the isooctane conversion was only around 50%, there was very minimal amount of

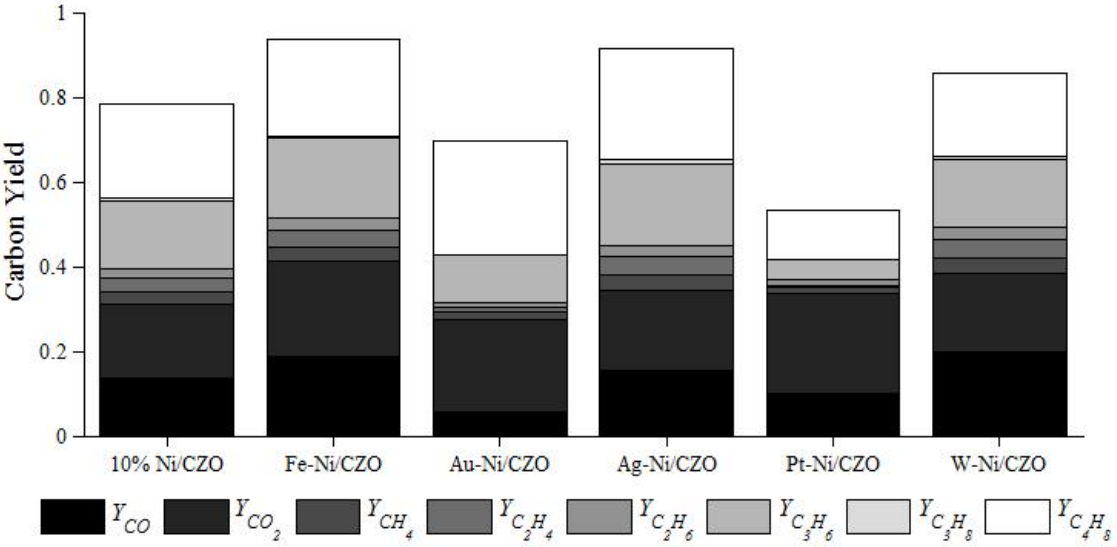

Figure 5.4: Steady-state carbon fractions for monometallic 10% Ni/CZO catalyst and associated bimetallics. (Reactor conditions: $H_2O/C = 1$, $O/C = 0.75$, GHSV = 200 k h^{-1}, $T_{inlet} = 500°C$, $S_{in} = 13.43$ ppmv.)

isobutylene in the reactor effluent. Based upon these observations it is clear that this catalyst offers promise for sulfur tolerant ATR catalysis. Additional work should be done to compare the activity of the catalyst to that of monometallic Pt catalysts. Any benefit of modifying the Ni surface by platinum should be greater than the activity of the platinum alone.

The W-Ni catalyst had good initial activity, with a Y^0_{SG} greater than monometallic Ni. However, this catalyst showed poor stability and the catalyst deactivated within the first three hours of operation. The deactivation pattern was similar to the Au-Ni catalysts, suggesting a similar mechanism described above, whereby W lowers the activity of Ni sites. It appears that this is a loading dependent effect, as the 0.1% W-5% Ni catalyst exhibited sustained initial Y_{SG} for at least 4 hours-on-stream. Additional characterization of the Ni-W electronic and ensemble interaction may provide an interesting explanation of this behavior.

5.4 Conclusion

This preliminary screening study analyzed the performance of several bimetallic Ni-based catalyst formulations. They were tested for their activity to the ATR of isooctane ($H_2O/C = 1$; $O/C = 0.75$; GHSV = 200,000 hr^{-1}). The isooctane was doped with a relatively high dose of thiophene in order to stress-test the tolerance of these catalysts. Under these conditions all of the tested catalysts showed considerable deactivation, with maximum deactivation rates observed within ten hours on-stream. The trends in catalyst activity suggested that there were several different routes for sulfur deactivation in the catalysts, suggesting the interplay of different types of Ni sites. Deviations in this behavior from the monometallic Ni catalysts suggested the presence of separate deactivation mechanisms for the Au-Ni formulations, the 0.1% Pt-5% Ni, and the 0.2% W-10% Ni catalysts. Additional investigations into these materials would likely provide invaluable insight into the deactivation mechanisms in an ATR reactor.

The results of this study demonstrated that for the catalysts based upon the 5% Ni/CZO precursor the durability of the catalysts to high sulfur exposure increased in rank of Au-Ni < (Ag-Ni, Pt-Ni) < (Ni, Fe-Ni) < W-Ni. When the 10% Ni/CZO catalysts were tested, there was generally higher carbon deposition, which further complicated the durability testing. Based upon those analyses the rank in durability for the higher loaded materials was Au-Ni < W-Ni < (Ni, Fe-Ni, Ag-Ni) < Pt-Ni. Based upon their favorable performance it is suggested that the bimetallic catalysts 0.1% W-5% Ni/CZO and 0.2% Pt-10% Ni/CZO offer significant promise for the development of more sulfur tolerant reformers. In both cases, they offered higher initial and final Y_{SG} as compared to their monometallic counterparts in addition to their longer viability at the initial Y_{SG} value.

CHAPTER VI

Summary of Conclusions and Recommendations for Future Studies

The principal goal of the research described in this dissertation was to understand the process of sulfur poisoning within Autothermal Reforming reactors. Through the employ of a well crafted experimental approach, considerable progress was made to understand fundamental processes within a complex reaction system. The catalyst materials studied were nickel based catalysts supported on a mixed oxide of cerium-zirconium (Ni/CZO). The endeavors of prior researchers identified this material as a suitable target for ATR chemistry, and outlined suitable synthesis procedures and reaction environments which would limit the deposition of carbon on the catalyst surface. Still, the inclination of Ni/CZO to deactivate readily under sulfur exposure was a major problem facing these materials. The work presented in this thesis provides ample knowledge to predict the deployment of Ni/CZO-based catalysts in sulfur-tolerant fuel reformers.

6.1 Major Achievements

This dissertation summarized experiments which studied the reforming of isooctane doped with thiophene. This mixture was used as a surrogate for commercial gasoline. This was a necessary approach in order to develop new knowledge into the intricate ATR system by reducing its complexity. While this approximation overestimates the effect of sulfur poisoning, it accurately describes the chemical composition of the reactor effluent. This fact implies that surrogate fuels are good at describing the chemistry of the reformer, and that there is more to be learned on how sulfur impacts the reforming of C_5-C_7 and aromatic hydrocarbons.

Initial experiments were performed to analyze reforming behavior without Ni present. These experiments describe the importance of homogeneous chemistry and support activity. While CZO is active towards reforming chemistry; the addition of Ni to the material provides long-term stability and increased production of desired reforming products. When sulfur is not present in the feed, the exit composition from the reactor is closely consistent with thermodynamic equilibrium predictions.

Sulfur negatively impacts the SR activity of Ni more strongly than the other chemical mechanisms in the system. This can be deduced from the elevated temperature profile seen when sulfur is present and the fact that the effluent composition is skewed towards intermediate homogeneous cracking products such as isobutylene and propylene. This diminished activity was observed as soon as the catalyst lit-off; there was no delayed-induction period. This phenomenon is described by a quickly established equilibrium of sulfur coverage which impaired the ability of Ni to catalyze reforming reactions. The deviation in initial activity from sulfur-free feeds was found to be strongly dependent on the inlet sulfur concentration.

Various post-reaction characterization techniques were unable to identify sulfur species on the catalyst following low-level exposures of thiophene. This suggests that the decline in initial catalytic activity is not due to irreversible sulfide formation. In

contrast, higher exposures of sulfur eventually led to severely diminished reforming activity after an initial period of stable performance. This latter behavior does suggest the formation of sulfides which drastically impede the activity of Ni.

At elevated Ni loadings it was observed that the conversion of thiophene to H_2S had a stronger correlation to maintained activity than inlet sulfur concentration. When no thiophene was found in the effluent, there was stable activity. Conversely, when conditions were such that Ni did not facilitate HDS chemistry it would also suffer continued declines in reforming activity. The determining factor which determined which of these phenomena predominated was the inlet conditions. When the thermodynamics of a particular feed scenario (see Figure 3.11b) predicted a strong driving-force for H_2 production, it appears that an altered adsorption equilibrium of sulfur prevented the formation of irreversible sulfides.

This interesting relationship between HDS and reforming activity was not seen at lower Ni loadings. It did not appear that thiophene interacted strongly with Ni catalysts with smaller particle sizes. However, these catalysts were significantly less active at reforming of isooctane, even under sulfur-free conditions. This result is surprising considering that higher dispersion materials are often the driving focus behind new catalyst synthesis techniques. Such materials have been described by previous researchers as being highly active to the SR of light hydrocarbons and less prone to deactivation from carbon deposition.

Two possible explanations were discussed in this thesis for particle size effects on the ATR of isooctane. The first (Figure 6.1) was that the ensemble sizes of the more highly dispersed Ni catalysts were ineffectual at the reforming of heavier hydrocarbons. The second (Figure 6.2) was that in the complex redox environment of an ATR, smaller particles are more prone to oxidation, rendering them less active for the desired reforming reactions. Regardless, of the explanation, this new knowledge suggests that radical new thinking is required in the development of better ATR

catalysts.

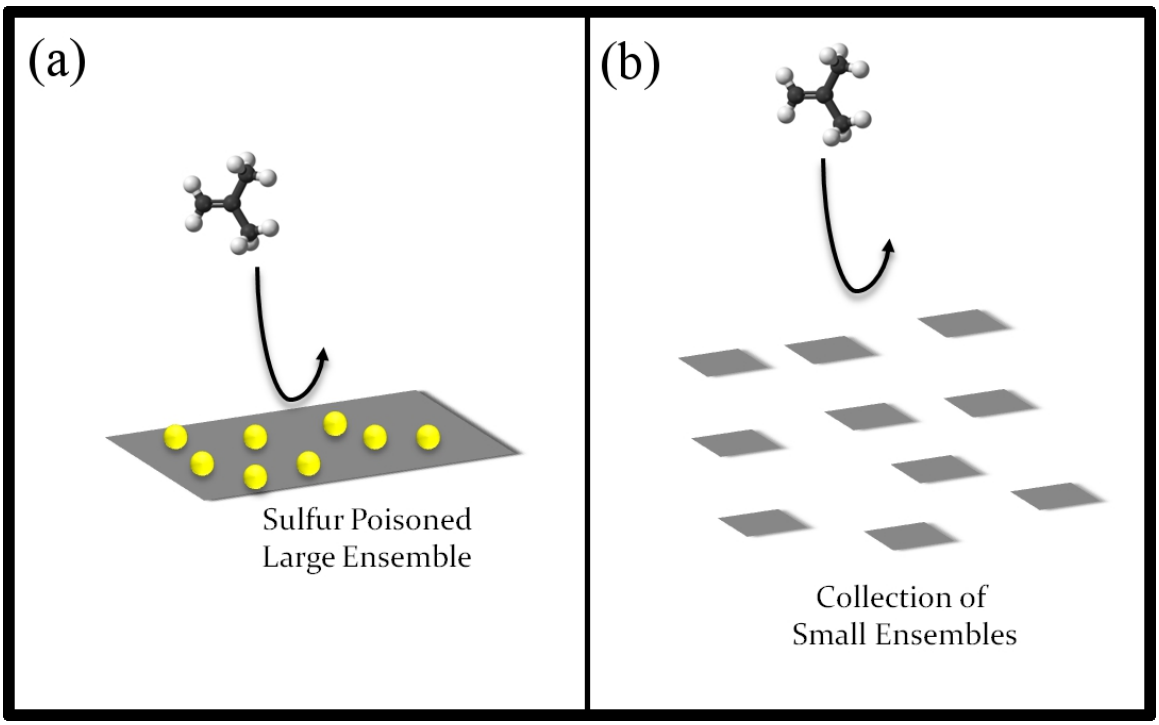

Figure 6.1: Cartoon depiction of the theory that the influence of particle size on ATR reactivity is dependent on ensemble size restrictions. For big Ni particles, ample ensemble size is present to adsorb hydrocarbon molecules but the ensemble is disrupted by the presence of chemisorbed sulfur species (a). Comparatively, the small Ni particles present insufficient ensemble sizes even under sulfur free conditions (b).

Finally, the ATR activities of a series of carefully selected bimetallic catalyst formulations were tested. These experiments identified materials which offer promise for further study. The addition of gold to the Ni system decreased the tolerance of the catalyst to thiophene exposure. The fact that gold is known to selectively bind to highly active SR sites and impart long-range chemical changes on the Ni surface provides interesting fundamental insight into the ATR reaction.

This work specifically identified two possible candidates which may unlock the promise of sulfur-tolerant reformer activity. These were the 0.1 wt% W modified 5 wt% Ni/CZO and the 0.2 wt% Pt modified 10 wt% Ni/CZO. The insight that

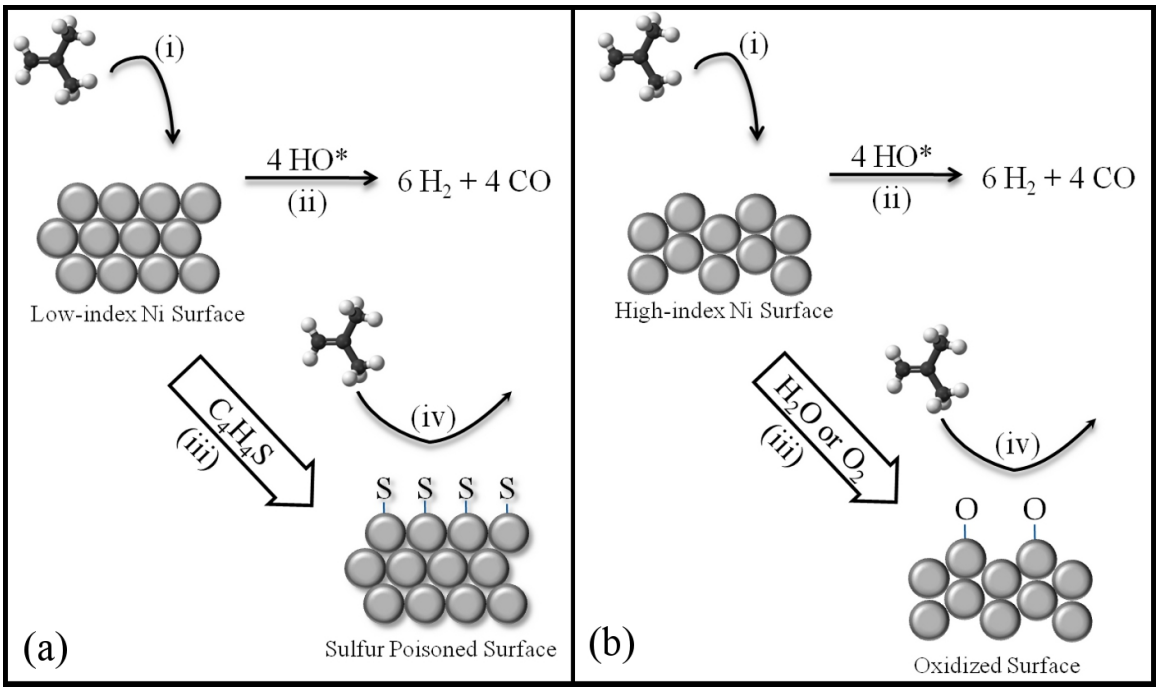

Figure 6.2: A key process in the reforming chemistry involves hydrocarbon adsorption (i) followed by reaction with adsorbed hydroxyl species to form synthesis gas (ii). The poisoning of low-index (a) and high-index (b) surfaces may occur by exposure to either sulfur or oxygen source, respectively (iii). This altered surface has a lowered affinity to the adsorbate.

different metals are more promising for higher versus lower weight loading of Ni again hints at the complex role that ensemble size plays in determining activity.

6.2 Future Work

The work discussed in these pages provides many answers about how the Ni-catalyzed ATR reactor behaves. Yet, it also raises many avenues for future exploration. Below are several proposed starting-points for future research into these areas.

In this work, system variables were purposefully manipulated to ask specific questions of the reactor system. Therefore, due to the complex parameter space of an ATR reactor and limitations on various resources, there were certain variables that remained unchanged in all of the experiments discussed in this dissertation. For example, the support material was always CZO. The consideration of other support materials would be interesting, in that it would further define the role of active vs. non-active and reducible vs. non-reducible supports. Additionally, considering higher or lower space velocities may provide insight into how the contact time and diffusion of thiophene alter poisoning behavior.

There are experiments which may be undertaken which expand upon the efforts presented in this thesis. For example, DRIFTS studies were effectively used to describe the bonding character of pre-reaction catalysts. This tool could be readily applied to post-reaction samples to understand how in-situ sintering mechanisms differ from the controlled aging discussed in Chapter IV.

A more comprehensive understanding of the influence of different types of Ni sites may arise from further investigations of gold alloyed materials, or pre-sulfided catalysts. There are many opportunities for creative characterization studies on such materials.

Finally, future experiments might consider the ATR performance of other surrogates for gasoline. Clearly, there is a need to understand the effect that sulfur has

upon the reforming of lighter versus heavier hydrocarbons. It would also be interesting to consider potential particle size effects in the presence of a smaller sulfur source, such as H_2S.

APPENDICES

APPENDIX A

GC Calibration and Error Analysis

A.1 Hydrocarbon Detector

The Analytical system is described in detail in Chapter II This section describes the calibrations performed in order to interpret the results from the chromatograms from each experiment. Separate calibrations were performed for the three GC detectors. The first detector was used to quantify ethylene, ethane, propylene, propane, and isobutylene. The areas of each peak were used to calculate a corresponding concentration with aid of response factors. The response factor was determined for each of the compounds by running a certified standard mixture of the gases diluted to varying degrees with N_2. Five different compositions were considered in developing the curve standard, and three GC sample injections were averaged at each concentration. Figure A.1 shows the calibration curves for the first detector.

Table A.1 lists the Response Factors and corresponding correlation coefficient for the hydrocarbon detector.

A.2 Stationary Gas Detector

Table A.2 lists the Response Factors and corresponding correlation coefficient for the stationary gas detector.

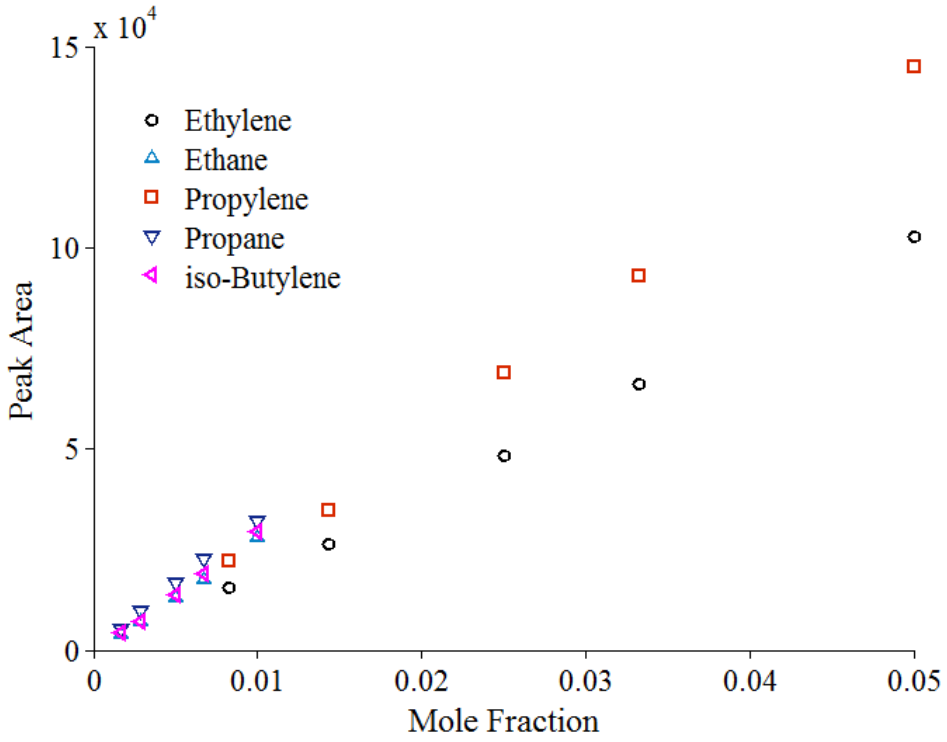

Figure A.1: Calibrations for ethylene, ethane, propylene, propane, and isobutylene.

	Response Factor	R^2
C_2H_4	2.00e6	0.9993
C_2H_6	2.68e6	0.999
C_3H_6	2.81e6	0.9982
C_3H_8	3.32e6	0.998
C_4H_8	3.38e6	0.999

Table A.1: Response Factors and Correlation Coefficients for Hydrocarbon Detector.

	Response Factor	R^2
H_2	73397	0.996
N_2	4230.3	0.9827
CO	5131.9	0.9996
CO_2	13822	0.9957
CH_4	34660	0.9993

Table A.2: Response Factors and Correlation Coefficients for Stationary Gas Detector.

A.3 Sulfur Detector

The curves in Figures A.2 and A.3 were used to calibrate the concentrations of sulfur containing molecules for flowrates less than 3000 sccm.

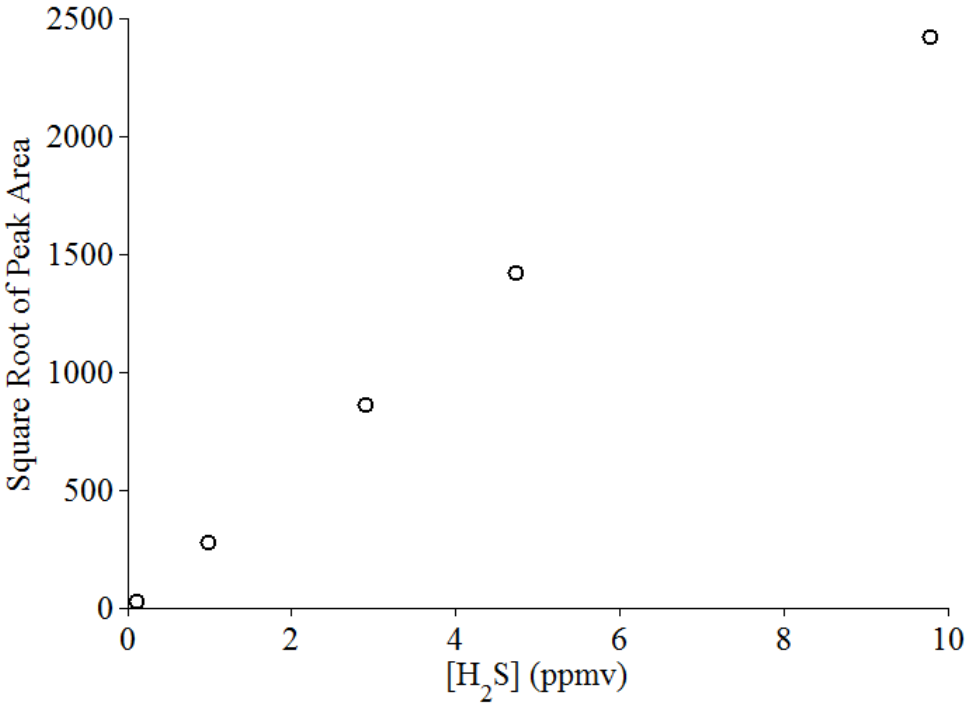

Figure A.2: Calibration curve for H_2S at low to moderate flow.

A.4 Discusion of Experimental Error

The validity of the data presented in this dissertation has been verified by the repetition of the described experimental protocols. Where error bars are given they represent the standard error of the mean of the observed measurements. The standard error formula is given in Equation A.1.

$$SE_{\bar{x}} = \frac{s}{\sqrt{n}} = \frac{\sqrt{\sum_{k=1}^{n} (x_k - \bar{x})^2}}{n} \tag{A.1}$$

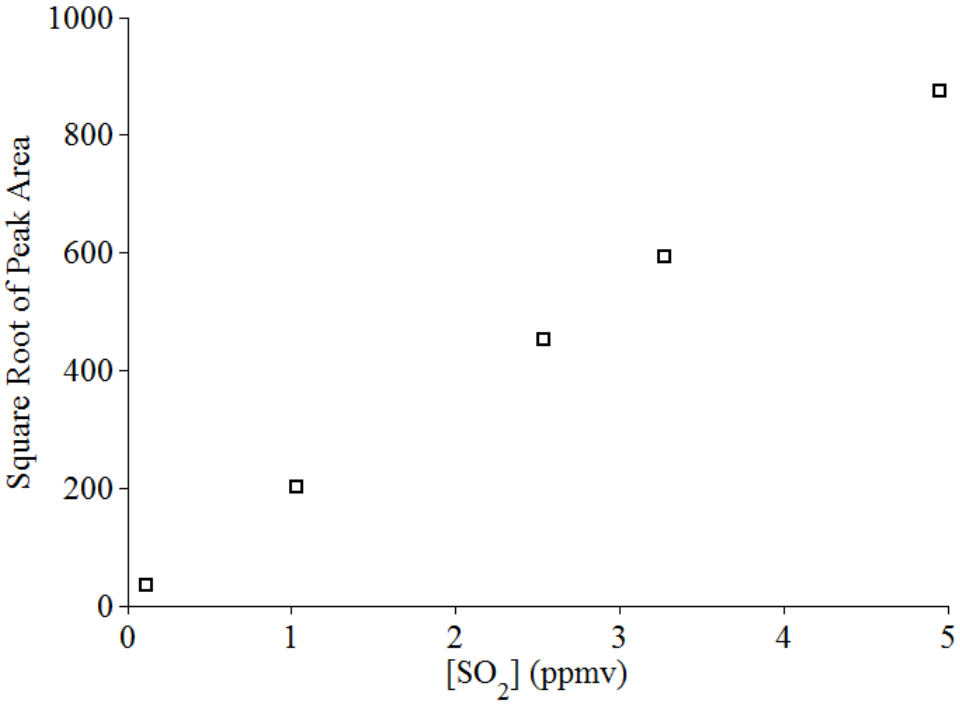

Figure A.3: Calibration curve for SO_2 at low to moderate flow.

Where s is the standard deviation of the sample mean, $\bar{x}$, n is the number of samples taken, x_k refers to the k'th value of the meausurement of x.

The mean and error measurements are calculated from at least three repeat experiments. Error bars never correspond merely to repeated measurement of the same experimental value. This type of error (Measurement Error) is included, along with Experimental Error and Sampling Error, in the total error estimate when the standard error is calculated for multiple experiments. Where error bars are omitted, the presented data is from a single experiment. This data was chosen as representative of the qualitative trends that were observed from the repeated experiments.

BIBLIOGRAPHY

BIBLIOGRAPHY

Abild-Pedersen, F., O. Lytken, J. Engbaek, G. Nielsen, I. Chorkendorff, and J. Norskov (2005), Methane activation on Ni(111): Effects of poisons and step defects, *Surface Science*, *590*(2–3), 127–137.

Agnelli, M., H. Swaan, C. Marquez-Alvarez, G. Martin, and C. Mirodatos (1998), CO hydrogenation on a nickel catalyst: II. A mechanistic study by transient kinetics and infrared spectroscopy, *Journal of Catalysis*, *175*(1), 117–128.

Agostini, G., R. Pellegrini, G. Leofanti, L. Bertinetti, S. Bertarione, E. Groppo, A. Zecchina, and C. Lamberti (2009), Determination of the particle size, available surface area, and nature of exposed sites for silica-alumina-supported Pd nanoparticles: A multitechnical approach, *Journal of Physical Chemistry C*, *113*(24), 10,485–10,492.

Ahmed, K., L. Kershenbaum, and D. Chadwick (1990), Adsorption of thiophene on nickel/alumina catalysts, *Industrial and Engineering Chemistry Research*, *29*(2), 150–156.

Allen, G., S. Harris, J. Jutson, and J. Dyke (1989), A study of a number of mixed transition metal oxide spinels using X-ray Photoelectron Spectroscopy, *Applied Surface Science*, *37*(1), 111–134.

Alstrup, I., J. Rostrup-Nielsen, and S. Roen (1981), High temperature hydrogen sulfide chemisorption on nickel catalysts, *Applied Catalysis*, *1*(5), 303–314.

Ashrafi, M., C. Pfeifer, T. Proll, and H. Hofbauer (2008), Experimental study of model biogas catalytic steam reforming: 2. Impact of sulfur on the deactivation and regeneration of Ni-based catalysts, *Energy and Fuels*, *22*(6), 4190–4195.

Balducci, G., J. Kapar, F. Paolo, G. Mauro, and I. Saiful (1998), Surface and reduction energetics of the CeO_2-ZrO_2 catalysts, *The Journal of Physical Chemistry. B*, *102*(3), 557–561.

Barison, S., et al. (2007), Novel $Au/La_{1-x}Sr_xMnO_3$ and $Au/La_{1-x}Sr_xCrO_3$ composites: Catalytic activity for propane partial oxidation and reforming, *Solid State Ionics*, *177*(39–40), 3473–3484.

Barone, G. (2003), Method of passivating a gas vessel or component of a gas transfer system ..., United States Patent No. 6511760.

Beebe, T. J., D. Goodman, B. Kay, and J. J. Yates (1987), Kinetics of the activated dissociative adsorption of methane on the low index planes of nickel single crystal surfaces, *The Journal of Chemical Physics*, *87*(4), 2305–2315.

Bell, M., A. McDermott, S. Zeger, J. Samet, and F. Dominici (2004), Ozone and short-term mortality in 95 US urban communities, 1987-2000, *Journal of the American Medical Association*, *292*(19), 2372–2378.

Bengaard, H., J. Norskov, J. Sehested, B. Clausen, L. Nielsen, A. Molenbroek, and J. Rostrup-Nielsen (2002), Steam reforming and graphite formation on Ni catalysts, *Journal of Catalysis*, *209*(2), 365–384.

Bertolini, J., and B. Tardy (1981), Vibrational EELS studies of CO chemisorption on clean and carbided (111), (100) and (110) nickel surfaces, *Surface Science*, *102*(1), 131–150.

Besenbacher, F., I. Chorkendorff, B. S. Clausen, B. Hammer, A. M. Molenbroek, J. K. Norskov, and I. Stensgaard (1998), Design of a surface alloy catalyst for steam reforming, *Science*, *279*(5358), 1913–1915.

Blackmond, D., and E. Ko (1985), Structural sensitivity of CO adsorption and H_2/CO coadsorption on Ni/SiO_2 catalysts, *Journal of Catalysis*, *96*(1), 210–221.

Blyholder, G. (1964), Molecular orbital view of chemisorbed carbon monoxide, *Journal of Physical Chemistry*, *68*(10), 2772–2778.

Borowiecki, T. (1982), Nickel catalysts for steam reforming of hydrocarbons; size of crystallites and resistance to coking, *Applied Catalysis*, *4*, 223–231.

Brodrick, C.-J., T. Lipman, M. Farshchi, N. Lutsey, H. Dwyer, D. Sperling, S. Gouse III, D. Harris, and F. King Jr. (2002), Evaluation of fuel cell auxiliary power units for heavy-duty diesel trucks, *Transporation Research Part D Transport and Environment*, *7*(4), 303–315.

Burri, J., R. Crockett, R. Hany, and D. Rentsch (2004), Gasoline composition determined by 1H NMR spectroscopy, *Fuel*, *83*(2), 187–193.

Campuzano, J., and R. Greenler (1979), The adsorption sites of CO on Ni(111) as determined by infrared reflection-absorption spectroscopy, *Surface Science*, *83*(1), 301–312.

Cheekatamarla, P., and A. Lane (2005), Catalytic autothermal reforming of diesel fuel for hydrogen generation in fuel cells: I. Activity tests and sulfur poisoning, *Journal of Power Sources*, *152*(1–2), 256–263.

Cheekatamarla, P., and A. Lane (2006), Efficient sulfur-tolerant bimetallic catalysts for hydrogen generation from diesel fuel, *Journal of Power Sources*, *153*(1), 157–164.

Cheekatamarla, P., and W. Thomson (2006), Hydrogen generation from 2,2,4-trimethyl pentane reforming over molybdenum carbide at low steam-to-carbon ratios, *Journal of Power Sources*, *156*(2), 520–524.

Chen, H., D. Zhang, and G. Lu (1990), Superparamagnetism of Ni_xFe_{1-x} thin films, *Journal of Magnetism and Magnetic Materials*, *84*(1–2), 208–212.

Chen, X., A. Tadd, and J. Schwank (2007), Carbon deposited on Ni/Ce-Zr-O isooctane autothermal reforming catalysts, *Journal of Catalysis*, *251*(2), 374–387.

Chevron (2006), Aviation fuels technical overview.

Chin, Y.-H., H.-S. King, D.L. andRoh, Y. Wang, and S. M. Heald (2006), Structure and reactivity investigations on supported bimetallic auni catalysts used for hydrocarbon steam reforming, *Journal of Catalysis*, *244*, 153–162.

Chorkendorff, I., and J. Niemantsverdriet (2003), *Concepts of Modern Catalysis and Kinetics*, 180 pp., John Wiley & Sons, Weinheim.

Choudhary, V., K. Mondal, and T. Choudhary (2007), Oxy-methane reforming over high temperature stable NiCoMgCeOx and NiCoMgOx supported on zirconia-haffnia catalysts: Accelerated sulfur deactivation and regeneration, *Catalysis Communications*, *8*(3), 561–564.

Choudhary, V. R., B. Prabhakar, and A. M. Rajput (1995), Beneficial effects of noble metal addition to Ni/Al_2O_3 catalyst for oxidative methane-to-syngas conversion, *Journal of Catalysis*, *157*, 752—754.

Dantas, S., J. Escritori, R. Soares, and C. Hori (2010), Effect of different promoters on $Ni/CeZrO_2$ catalyst for autothermal reforming and partial oxidation of methane, *Chemical Engineering Journal*, *156*(2), 380–387.

Demirci, U. B. (2007), Theoretical means for searching bimetallic alloys as anode electrocatalysts for direct liquid-feed fuel cells, *Journal of Power Sources*, *173*(1), 11–18.

Dinka, P., and A. Mukasyan (2007), Perovskite catalysts for the auto-reforming of sulfur containing fuels, *Journal of Power Sources*, *167*(2), 472–481.

Docter, A., and A. Lamm (1999), Gasoline fuel cell systems, *Journal of Power Sources*, *84*(2), 194–200.

DOE (2005a), Annual energy review 2004, Energy Information Administration.

DOE (2005b), Annual energy review 2008, Energy Information Administration.

DOE (2007), U.S. sulfur content (weighted average) of crude oil input to refineries (percent), tonto.eia.doe.gov/dnav/pet/hist/mcrs1us2m.htm.

Enger, B., R. Lodeng, and A. Holmen (2009), Evaluation of reactor and catalyst performance in methane partial oxidation over modified nickel catalysts, *Applied Catalysis A: General*, *364*(1-2), 15–26.

EPA (2000), Tier 2/gasoline sulfur final rule, united States Environmental Protection Agency, http://www.epa.gov/tier.

EPA (2007), National Clean Diesel Campaign, http://www.epa.gov/cleandiesel/.

Escritori, J., S. Dantas, R. Soares, and C. E. Hori (2009), Methane autothermal reforming on nickel-ceria-zirconia based catalysts, *Catalysis Communications*, *10*(7), 1090–1094.

Fisher, G. (2009), Personal communication, 2009.

Flytzani-Stephanop., M., and G. Voecks (1983), Autothermal reforming of aliphatic and aromatic hydrocarbon liquids, *International Journal of Hydrogen Energy*, *8*(7), 539–548.

Gaines, L., A. Vyas, and J. Anderson (2006), Estimation of fuel use by idling commercial trucks, *Transportation Research Record*, *1983*(1983), 91–98.

Goud, S., W. Whittenberger, S. Chattopadhyay, and M. Abraham (2007), Steam reforming of n-hexadecane using a Pd/ZrO_2 catalyst: Kinetics of catalyst deactivation, *International Journal of Hydrogen Energy*, *32*(14), 2868–2874.

Gould, B., X. Chen, and J. Schwank (2007), Dodecane reforming over nickel-based monolith catalysts, *Journal of Catalysis*, *250*(2), 209–221.

Gould, B., X. Chen, and J. Schwank (2008), n-Dodecane reforming over nickel-based monolith catalysts: Deactivation and carbon deposition, *Applied Catalysis A: General*, *334*(1–2), 277–290.

Gramshaw, J., and A. Hussain (1978), Gas-liquid chromatography of thiols using flame-photometric detection and a deactivated transfer line, *Journal of Chromatography A*, *157*(C), 267–275.

Greeley, J., J. K. Norskov, and M. Mavrikakis (2002), Electronic structure and catalysis on metal surfaces, *Annual Review of Physical Chemistry*, *53*(1), 319–348.

Grosvenor, A., M. Biesinger, R. Smart, and N. McIntyre (2006), New interpretations of XPS spectra of nickel metal and oxides, *Surface Science*, *600*(9), 1771–1779.

Hadjiivanov, K., M. Mihaylov, N. Abadjieva, and D. Klissurski (1998), Characterization of Ni/TiO_2 catalysts prepared by successive adsorption-reduction of Ni^{2+} ions, *Journal of the Chemical Society — Faraday Transactions*, *94*(24), 3711–3716.

Hadjiivanov, K., M. Mihaylov, D. Klissurski, P. Stefanov, N. Abadjieva, E. Vassileva, and L. Mintchev (1999), Characterization of Ni/SiO_2 catalysts prepared by successive deposition and reduction of Ni^{2+} ions, *Journal of Catalysis*, *185*(2), 314–323.

Hammer, B., and J. Norskov (1995), Electronic factors determining the reactivity of metal surfaces, *Surface Science*, *343*(3), 211–220.

Hansen, J., D. Johnson, A. Lacis, S. Lebedeff, P. Lee, D. Rind, and G. Russell (1981), Climate impact of increasing atmospheric carbon dioxide, *Science*, *213*(4511), 957–966.

Haynes, C. (2001), Clarifying reversible efficiency misconceptions of high temperature fuel cells in relation to reversible heat engines, *Journal of Power Sources*, *92*(1–2), 199–203.

Henry, C. (2007), *Size Effects on Structure and Morphology of Free or Supported Nanoparticles*, chap. 1, pp. 3–34, John Wiley & Sons.

Hepola, J., and P. Simell (1997), Sulphur poisoning of nickel-based hot gas cleaning catalysts in synthetic gasification gas: II. Chemisorption of hydrogen sulphide, *Applied Catalysis B: Environmental*, *14*(3–4), 305 – 321.

Hernandez-Maldonado, A., and R. Yang (2004), Desulfurization of transportation fuels by adsorption, *Catalysis Reviews - Science and Engineering*, *46*(2), 111–150.

Holladay, J., J. Hu, D. King, and Y. Wang (2009), An overview of hydrogen production technologies, *Catalysis Today*, *139*(4), 244–260.

Horn, R., K. Williams, N. Degenstein, and L. Schmidt (2006), Syngas by catalytic partial oxidation of methane on rhodium: Mechanistic conclusions from spatially resolved measurements and numerical simulations, *Journal of Catalysis*, *242*(1), 92–102.

Horn, R., K. Williams, N. Degenstein, A. Bitsch-Larsen, D. Dalle Nogare, S. Tupy, and L. Schmidt (2007), Methane catalytic partial oxidation on autothermal Rh and Pt foam catalysts: Oxidation and reforming zones, transport effects, and approach to thermodynamic equilibrium, *Journal of Catalysis*, *249*(2), 380–393.

Huang, L., J. Xie, R. Chen, D. Chu, and A. T. Hsu (2010), Nanorod alumina-supported Ni-Zr-Fe/Al_2O_3 catalysts for hydrogen production in auto-thermal reforming of ethanol, *Materials Research Bulletin*, *45*(1), 92–96.

Jain, S., H.-Y. Chen, and J. Schwank (2006), Techno-economic analysis of fuel cell auxiliary power units as alternative to idling, *Journal of Power Sources*, *160*(1), 474–484.

Jones, G., et al. (2008), First principles calculations and experimental insight into methane steam reforming over transition metal catalysts, *Journal of Catalysis*, *259*(1), 147–160.

Kambolis, A., H. Matralis, A. Trovarelli, and C. Papadopoulou (2010), Ni/CeO_2-ZrO_2 catalysts for the dry reforming of methane, *Applied Catalysis A: General*, *377*(1–2), 16–26.

Koga, H., S. Fukahori, T. Kitaoka, A. Tomoda, R. Suzuki, and H. Wariishi (2006), Autothermal reforming of methanol using paper-like Cu/ZnO catalyst composites prepared by a papermaking technique, *Applied Catalysis A: General*, *309*(2), 263–269.

Krumpelt, M., T. Krause, J. Carter, J. Kopasz, and S. Ahmed (2002), Fuel processing for fuel cell systems in transportation and portable power applications, *Catalysis Today*, *77*(1–2), 3–16.

Kumar, P., Y. Sun, and R. Idem (2007), Nickel-based ceria, zirconia, and ceria zirconia catalytic systems for low-temperature carbon dioxide reforming of methane, *Energy and Fuels*, *21*(6), 3113–3123.

Kummerle, E., and G. Heger (1999), The structures of C-$Ce_2O_{3+\delta}$, Ce_7O_{12}, and $Ce_{11}O_{20}$, *Journal of Solid State Chemistry*, *147*(2), 485–500.

Lakhapatri, S., and M. Abraham (2009), Deactivation due to sulfur poisoning and carbon deposition on Rh-Ni/Al_2O_3 catalyst during steam reforming of sulfur-doped n-hexadecane, *Applied Catalysis A: General*, *364*(1–2), 113–121.

Lamp, P., J. Tachtler, O. Finkenwirth, S. Mukerjee, and S. Shaffer (2003), Development of an auxiliary power unit with solid oxide fuel cells for automotive applications, *Fuel Cells*, *3*(3), 146–152.

Laosiripojana, N., and S. Assabumrungrat (2005), Methane steam reforming over Ni/Ce-ZrO_2 catalyst: Influences of Ce-ZrO_2 support on reactivity, resistance toward carbon formation, and intrinsic reaction kinetics, *Applied Catalysis A: General*, *290*(1–2), 200–211.

Larsen, J., and I. Chorkendorff (1999), From fundamental studies of reactivity on single crystals to the design of catalysts, *Surface Science Reports*, *35*(5-8), 163–222.

Li, B., S. Kado, Y. Mukainakano, M. Nurunnabi, T. Miyao, S. Naito, K. K., and K. Tomishige (2006), Temperature profile of catalyst bed during oxidative steam reforming of methane over Pt-Ni bimetallic catalysts, *Applied Catalysis A: General*, *304*, 62–71.

Li, B., S. Kado, Y. Mukainakano, T. Miyazawa, T. Miyao, S. Naito, K. Okumura, K. Kunimori, and K. Tomishige (2007), Surface modification of Ni catalysts with trace Pt for oxidative steam reforming of methane, *Journal of Catalysis*, *245*(1), 144–155.

Lutsey, N., C.-J. Brodrick, and T. Lipman (2007), Analysis of potential fuel consumption and emissions reductions from fuel cell auxiliary power units (APUs) in long-haul trucks, *Energy*, *32*(12), 2428–2438.

Lutz, A., R. Bradshaw, L. Broomberg, and A. Rabinovich (2004), Thermodynamic analysis of hydrogen production by partial oxidation reforming, *International Journal of Hydrogen Energy*, *29*(8), 809–816.

Mayne, J., A. Tadd, K. Dahlberg, and J. Schwank (2010), Influence of thiophene on the isooctane reforming activity of ni-based catalysts, *Journal of Catalysis*, *271*(1), 140–152.

McIntyre, N., and M. Cook (1975), X-Ray photoelectron studies on some oxides and hydroxides of cobalt, nickel, and copper, *Analytical Chemistry*, *47*(13), 2208–2213.

Micromeritics (2005), *ASAP 2020 Chemi Operator's Manual*, Micromeritics Instrument Corporation.

Mikami, I., R. Kitayama, and T. Okuhara (2003), Utrarapid hydrogenation of high concentrations of nitrate ions catalyzed by Pt-modified nickel catalysts, *Catalysis Letters*, *91*(1–2), 69–71.

Molenbroek, A., J. K. Norskov, and B. S. Clausen (2001), Structure and reactivity of Ni-Au nanoparticle catalysts, *The Journal of Physical Chemistry B*, *105*(23), 5450–5458.

Montini, T., A. Speghini, L. De Rogatis, B. Lorenzut, M. Bettinelli, M. Graziani, and P. Fornasiero (2009), Identification of the structural phases of $Ce_xZr_{1-x}O_2$ by Eu(III) luminescence studies, *Journal of the American Chemical Society*, *131*(36), 13,155–13,160.

Montoya, J., E. Romero-Pascual, C. Gimon, P. Del-Angel, and A. Monzon (2000), Methane reforming with CO_2 over Ni/ZrO_2-CeO_2 catalysts prepared by sol-gel, *Catalysis Today*, *63*(1), 71–85.

Moon, D., and J. W. Ryu (2003), Partial oxidation reforming catalyst for fuel cell-powered vehicles applications, *Catalysis Letters*, *89*, 207–212.

Murata, K., M. Saito, M. Inaba, and I. Takahara (2007), Hydrogen production by autothermal reforming of sulfur-containing hydrocarbons over re-modified $Ni/Sr/ZrO_2$ catalysts, *Applied Catalysis B: Environmental*, *70*(1–4), 509–514.

Nagaoka, K., K. Takanabe, and K.-I. Aika (2004), Modification of Co/TiO_2 for dry reforming of methane at 2 MPa by Pt, Ru or Ni, *Applied Catalysis A: General*, *268*(1–2), 151–158.

Navarro, R., M. Alvarez-Galvan, F. Rosa, and J. Fierro (2006), Hydrogen production by oxidative reforming of hexadecane over Ni and Pt catalysts supported on Ce/La-doped Al_2O_3, *Applied Catalysis A: General*, *297*(1), 60–72.

Nilsson, M., P. Jozsa, and L. Pettersson (2007), Evaluation of Pd-based catalysts and the influence of operating conditions for autothermal reforming of dimethyl ether, *Applied Catalysis B: Environmental*, *76*(1–2), 42–50.

Norskov, J., B. Clausen, and H. Topsoe (1992), Understanding the trends in the hydrodesulfurization activity of the transition metal sulfides, *Catalysis Letters*, *13*(1–2), 1–8.

NPRA (2010), Gasoline sulfur, http://www.npradc.org/issues/fuels/gasoline.cfm.

Owens, W., N. Rodriguez, and R. Baker (1994), Effect of sulfur on the interaction of nickel with ethylene, *Catalysis Today*, *21*(1), 3–22.

Pacheco, M., J. Sira, and J. Kopasz (2003), Reaction kinetics and reactor modeling for fuel processing of liquid hydrocarbons to produce hydrogen: Isooctane reforming, *Applied catalysis. A, General*, *250*(1), 161–175.

Panuccio, G., K. Williams, and L. Schmidt (2006), Contributions of heterogeneous and homogeneous chemistry in the catalytic partial oxidation of octane isomers and mixtures on rhodium coated foams, *Chemical Engineering Science*, *61*(13), 4207–4219.

Parizotto, N., D. D. Zanchet, K. Rocha, C. Marques, and J. Bueno (2009), The effects of Pt promotion on the oxi-reduction properties of alumina supported nickel catalysts for oxidative steam-reforming of methane: Temperature-resolved XAFS analysis, *Applied Catalysis A: General*, *366*(1), 122–129.

Patil, A., T. Dubois, N. Sifer, E. Bostic, K. Gardner, M. Quah, and C. Bolton (2004), Portable fuel cell systems for America's army: Technology transition to the field, *J. Power Sources*, *136*(1), 220–225.

Pengpanich, S., V. Meeyoo, T. Rirksomboon, and K. Bunyakiat (2002), Catalytic oxidation of methane over CeO_2-ZrO_2 mixed oxide solid solution catalysts prepared via urea hydrolysis, *Applied catalysis. A, General*, *234*(1-2), 221–233.

Pengpanich, S., V. Meeyoo, and T. Rirksomboon (2004), Methane partial oxidation over Ni/CeO_2-ZrO_2 mixed oxide solid solution catalysts, *Catalysis Today*, *93–95*, 95–105.

Pereira, E., and G.-A. Martin (1993), Alcohol synthesis from syngas over nickel catalysts: Effect of copper and lithium addition, *Applied Catalysis A: General*, *103*(2), 291–309.

Pillay, D., and M. Johannes (2008), Comparison of sulfur interaction with hydrogen on Pt(111), Ni(111) and Pt_3Ni(111) surfaces: The effect of intermetallic bonding, *Surface Science*, *602*(16), 2752–2757.

Pino, L., A. Vita, Cipiti, M. F., Lagana, and V. Recupero (2006), Performance of Pt/CeO_2 catalyst for propane oxidative steam reforming, *Applied Catalysis A: General*, *306*, 68–77.

Qi, A., S. Wang, G. Fu, and D. Wu (2005), Autothermal reforming of n-octane on Ru-based catalysts, *Applied Catalysis A: General*, *293*(1–2), 71–82.

Qi, A., S. Wang, C. Ni, and D. Wu (2007), Autothermal reforming of gasoline on Rh-based monolithic catalysts, *International Journal of Hydrogen Energy*, *32*(8), 981–991.

Rafaja, D. (2000), Deconvolution versus convolution, *Materials Structure*, *7*(2), 43–50.

Rakass, S., H. Oudghiri-Hassani, N. Abatzoglou, and P. Rowntree (2006), A study of the surface properties and steam reforming catalytic activity of nickel powders impregnated by n-alkanethiols, *Journal of Power Sources*, *162*(1), 579–588.

Resini, C., T. Venkov, K. Hadjiivanov, S. Presto, P. Riani, R. Marazza, G. Ramis, and G. Busca (2009), An FTIR study of the dispersed Ni species on Ni-YSZ catalysts, *Applied Catalysis A: General*, *353*(1), 137–143.

Rodriguez, J. (2006), The chemical properties of bimetallic surfaces: Importance of ensemble and electronic effects in the adsorption of sulfur and SO_2, *Progress in Surface Science*, *81*(4), 141–189.

Rodriguez, J., and J. Hrbek (1999), Interaction of sulfur with well-defined metal and oxide surfaces: Unraveling the mysteries behind catalyst poisoning and desulfurization, *Accounts of Chemical Research*, *32*(9), 719–728.

Rodriguez, J., J. Dvorak, A. Capitano, A. Gabelnick, and J. Gland (1999), Adsorption of thiophene on surfaces of clean and Ni-promoted molybdenum sulfide, *Surface Science*, *429*(1), L462–L468.

Rooksby, H. (1943), Structure of nickel oxide, *Nature*, *152*(3854), 304.

Rostrup-Nielsen, J. (1968), Chemisorption of hydrogen sulfide on a supported nickel catalyst, *Journal of Catalysis*, *11*(3), 220–227.

Rostrup-Nielsen, J. (1971), Some principles relating to the regeneration of sulfur-poisoned nickel catalyst, *Journal of Catalysis*, *21*(2), 171–178.

Rostrup-Nielsen, J. (1975), *Steam Reforming Catalysts*, Danish Technical Press, Copenhagen.

Rostrup-Nielsen, J. (1984), Catalytic steam reforming, in *Catalysis: Science and Technology*, vol. 5, chap. 1, Springer-Verlag.

Rostrup-Nielsen, J. (2002), Hydrogen and synthesis gas by steam and CO_2 reforming, *Advances in Catalysis*, *47*, 65.

Ruban, A., B. Hammer, P. Stoltze, H. Skriver, and J. Norskov (1997), Surface electronic structure and reactivity of transition and noble metals, *Journal of Molecular Catalysis A: Chemical*, *115*(3), 421–429.

Ruban, A. V., H. L. Skriver, and J. K. Norskov (1999), Surface segregation energies in transition-metal alloys, *Physical Review B*, *59*(24), 15,990–16,000.

Schwank, J., and A. Tadd (2010), Catalytic reforming of liquid hydrocarbons for on-board solid oxide fuel cell auxiliary power units, in *Catalysis*, vol. 22, edited by J. Spivey and K. Dooley, pp. 56–93, RSC Publishing.

Sehested, J. (2003), Sintering of nickel steam-reforming catalysts, *Journal of Catalysis*, *217*(2), 417–426.

Sehested, J. (2006), Four challenges for nickel steam-reforming catalysts, *Catalysis Today*, *111*(1–2), 103–110.

Sehested, J., J. Gelten, I. Remediakis, H. Bengaard, and J. Norskov (2004), Sintering of nickel steam-reforming catalysts: effects of temperature and steam and hydrogen pressures, *Journal of Catalysis*, *223*(2), 432–443.

Shaju, K., G. Subba Rao, and B. Chowdari (2003), X-ray photoelectron spectroscopy and electrochemical behaviour of 4 V cathode, $Li(Ni_1/2Mn_1/2)O_2$, *Electrochimica Acta*, *48*(11), 1505–1514.

Shekhawat, D., T. Gardner, D. Berry, M. Salazar, D. Haynes, and J. Spivey (2006), Catalytic partial oxidation of n-tetradecane in the presence of sulfur or polynuclear aromatics: Effects of support and metal, *Applied Catalysis A: General*, *311*(1–2), 8–16.

Smith, D. (2006), Method for chemical vapor deposition of silicon on to substrates for use in ..., United States Patent, No. 7070833.

Somorjai, G. (1994), *Introduction to Surface Chemistry and Catalysis*, John Wiley & Sons.

Srinivas, D., C. Satyanarayana, H. Potdar, and P. Ratnasamy (2003), Structural studies on NiO-CeO_2-ZrO_2 catalysts for steam reforming of ethanol, *Applied Catalysis A: General*, *246*(2), 323–334.

Strohm, J., J. Zheng, and C. Song (2006), Low-temperature steam reforming of jet fuel in the absence and presence of sulfur over Rh and Rh-Ni catalysts for fuel cells, *Journal of Catalysis*, *238*(2), 309–320.

Suo, Z., A. Lv, H. Lv, M. Jin, and T. He (2009), Influence of au promoter on hydrodesulfurization activity of thiophene over sulfided Au-Ni/SiO_2 bimetallic catalysts, *Catalysis Communications*, *10*(8), 1174–1177.

Tadd, A., B. Gould, and J. Schwank (2005), Packed bed versus microreactor performance in autothermal reforming of isooctane, *Catalysis Today*, *110*(1–2), 68–75.

Tadd, A. R. (2006), Hydrogen production from gasoline using nickel-based catalysts, Ph.D. thesis, University of Michigan.

van Hardeveld, R., and F. Hartog (1969), The statistics of surface atoms and surface sites on metal crystals, *Surface Science*, *15*(2), 189–230.

Vitos, L., A. Ruban, H. Skriver, and J. Kollar (1998), The surface energy of metals, *Surface Science*, *411*(1–2), 186–202.

Wang, L., K. Murata, and M. Inaba (2004a), Control of the product ratio of CO_2/(CO + CO_2) and inhibition of catalyst deactivation for steam reforming of gasoline to produce hydrogen, *Applied Catalysis B: Environmental*, *48*(4), 243–248.

Wang, L., K. Murata, and M. Inaba (2009), Highly efficient conversion of gasoline into hydrogen on Al_2O_3-supported Ni-based catalysts: Catalyst stability enhancement by modification with W, *Applied Catalysis A: General*, *358*(2), 264–268.

Wang, W., S. Stagg-Williams, F. Noronha, L. Mattos, and F. Passos (2004b), Partial oxidation and combined reforming of methane on ce-promoted catalysts, *Catalysis Today*, *98*(4), 553–563.

Wang, X., and R. Gorte (2001), Steam reforming of n-butane on Pd/ceria, *Catalysis Letters*, *73*(1), 15–19.

Wardencki, W. (1998), Problems with the determination of environmental sulphur compounds by gas chromatography, *Journal of Chromatography A*, *793*(1), 1–19.

Wei, J., and E. Iglesia (2004), Isotopic and kinetic assessment of the mechanism of reactions of CH_4 with CO_2 or H_2O to form synthesis gas and carbon on nickel catalysts, *Journal of Catalysis*, *224*(2), 370–383.

Xu, S., and X. Wang (2005), Highly active and coking resistant Ni/CeO_2-ZrO_2 catalyst for partial oxidation of methane, *Fuel*, *84*, 563–567.

Yin, C., and D. Xia (2004), A study of the distribution of sulfur compounds in gasoline produced in China. Part 3. Identification of individual sulfides and thiophenes, *Fuel*, *83*(4–5), 433–441.

Yoon, S., I. Kang, and J. Bae (2008), Effects of ethylene on carbon formation in diesel autothermal reforming, *International Journal of Hydrogen Energy*, *33*(18), 4780–4788.

Yoshida, K., N. Begum, S.-I. Ito, and K. Tomishige (2009), Oxidative steam reforming of methane over Ni/α-Al_2O_3 modified with trace noble metals, *Applied Catalysis A: General*, *358*(2), 186–192.

Youn, M., J. Seo, K. Cho, S. Park, D. R. Park, J. C. Jung, and I. K. Song (2008), Hydrogen production by auto-thermal reforming of ethanol over nickel catalysts supported on Ce-modified mesoporous zirconia: Effect of Ce/Zr molar ratio, *International Journal of Hydrogen Energy*, *33*(19), 5052–5059.

Zhu, T., and M. Flytzani-Stephanopoulos (2001), Catalytic partial oxidation of methane to synthesis gas over Ni-CeO_2, *Applied catalysis. A, General*, *208*(1–2), 403–417.

Zhu, Y.-A., D. Chen, X.-G. Zhou, P.-O. Astrand, and W.-K. Yuan (2010), First-principles calculations of C diffusion through the surface and subsurface of Ag/Ni(100) and reconstructed Ag/Ni(100), *Surface Science*, *604* (2), 186–19.